Near Infrared Photocurrent Spectroscopy on Carbon Nanotube Devices

TECHNISCHE UNIVERSITÄT DARMSTADT

At the department of Materials and Earth Sciences
of the Technischen Universität Darmstadt
Submitted in fulfilment of the requirements
for the degree of Doctor-Engineer
(Dr.-Ing.)

Doctoral Thesis
by Pranauv Balaji Selvasundaram
M.Tech. in Nanotechnology
From Delhi NCR, India

Referee: Prof. Dr. Ralph. M. Krupke
Co- Referee: Prof. Dr. Robert. Stark

Date of Submission: 04/08/2020
Date of Oral Exam: 28/10/2020

Darmstadt 2020

Table of Contents

List of Figures

List of tables

List of Abbreviations

1D	One Dimensional
AC	Alternating Current
AFM	Atomic Force Microscope
ALD	Atomic Layer Deposition
AUC	Analytical Ultracentrifuge
CNT	Carbon Nanotubes
CoMoCAT	Cobalt Molybdenum Catalyst process
CVD	Chemical Vapour Deposition
DC	Direct Current
DEP	Dielectrophoresis
DOS	Density of States
EBL	Electron Beam Lithography
EDL	Electrical Double Layer
FET	Field Effect Transistor
HiPCO	High Pressure Carbon Mono-oxide
IC	Integrated Chip
LED	Light Emitting Diode
MD	Molecular Dynamics
m-SWCNT	Metallic Single Walled Carbon Nanotube
MWCNT	Multi-Walled Carbon Nanotube
nIR	Near Infrared
PTE	Photo Thermoelectric Effect
PV	Photovoltaic
SEC	Size Exclusion Chromatography
SEM	Scanning Electron Microscopy

SOI	Silicon on Insulator
SOS	Silicon on Sapphire
STM	Scanning Tunneling Microscopy
s-SWCNT	Semiconducting Single Walled Carbon Nanotube
SWCNT	Single Walled Carbon Nanotube
UV	Ultra Violet
vHS	Von Hove Singularities
ZF	Zone Folding

Abstract

Single-walled carbon nanotubes (SWCNTs) constitute an allotrope of carbon with a two dimensional lattice structure rolled up to a seamless cylinder. Owing to their one dimensional structure, they possess unique optical properties including the ability to absorb light from visible to infrared regime. Additionally, they behave as metals or semiconductors depending upon their structure or the direction in which they are rolled up with respect to the graphene lattice. With solution processing techniques, it is now possible to fabricate devices consisting of carbon nanotubes with tailored properties for a variety of applications including optical detectors, optical emitters and other organic electronics.

This thesis work is focused on achieving for photocurrent generation in carbon nanotube transistor devices working under ambient conditions. The transistors with split gate geometry were fabricated with solution - processed carbon nanotubes as the transport channel and characterized using photocurrent spectroscopy. The nanotubes were integrated to form transistor devices dielectrophoretically, by depositing semiconducting previously sorted CNTs using polymer assisted size exclusion chromatography (SEC) in toluene. Also, a new method to measure the length distributions of the nanotubes using Analytical Untracentrifugation (AUC) was explored for the first time for non-aqueous suspensions. It was realized that the sedimentation behavior of monochiral suspensions studied in toluene deviated strongly from prior works carried out for aqueous suspensions, but a new and a rather simpler model allows to explain the observation.

On characterizing the transistor devices with photocurrent spectroscopy, it is realized that for the device geometry used, the photocurrent spectrum correlates well with the absorption spectrum of the deposited nanotubes. Also, the results display signatures from the substrates in the off-resonant regions of the spectrum. It was realized that only insulating substrates could provide a clean photoresponse specific to the nanotubes alone and that CNTs are sensitive to light absorption by the underlying substrate.

Furthermore, electric - field assisted measurements were carried out by applying a gate voltage on the split gates and measuring the short - circuit (source to drain) photocurrent signal. Based on the trends observed in the results, it is possible to identify the mechanism behind the generated photocurrent signal for a particular measurement scheme. Also, the results indicate that the Schottky barrier at the nanotube and the metal electrode interface dominates the pn-junction formed by the split gates. Nevertheless, the (n, m) specific relative photocurrent contribution could be tailored with the electrostatic field from the split gates.

Lastly, transistors were fabricated with silicon contact with solution processed few chiral and monochiral carbon nanotubes as the transport channel. Photocurrent spectroscopy was carried out on these transistors as well. Results show photocurrent signals originating from the substrate as well as from the smaller diameter tubes however, in opposite polarity, but not from the larger diameter tubes due to unfavorable energy level positions primarily for the few chiral suspensions. However, devices fabricated with a monochiral suspension, revealed that the photocurrent signatures resemble the signatures of the few chiral suspensions, indicating that the signatures are rather an effect from the substrate and not from the nanotube channel itself.

Declaration

I declare that this thesis, which I submit to the Technische Universität Darmstadt for examination in consideration of the degree award of Doctor of Engineering, is my own personal effort. Any of the content, which is the result from a related collaborative research program and presented in this document has been duly acknowledged. I certify that I have not yet submitted this thesis for a degree or diploma in any university. Furthermore, a reasonable care has been taken to ensure that the work is original, and to the best of my knowledge, it does not contain any material previously published or written by another person except where such work has been cited and acknowledged within the text.

Date

Signature

Acknowledgement

The research work presented in this thesis has been conducted at the Institute of Nanotechnology at Karlsruhe Institute of Technology, Germany and at the Department of Materials and Geosciences at the Technische Universität Darmstadt, Germany under the supervision of Prof. Dr. Ralph Krupke. I am grateful for his support scientifically and morally during the course of this thesis work, which helped in shaping this thesis work to its present form. My sincere thanks to him for his continuous support and encouragement over the entire period.

I am thankful to Prof. Dr. Robert Stark for co-refereeing this thesis, and to Prof. Dr. Jörg Schneider and Prof. Dr.-Ing. Horst Hahn for examining the dissertation.

I am grateful to Dr. Frank Hennrich for supporting me scientifically and morally along the Analytical Ultracentrifugation experiments with the length analysis of the carbon nanotube suspensions and providing me with the carbon nanotube materials used in this thesis.

My special thanks to Ms. Simone Dehm for supporting me in fabrication of devices of devices employed in this work.

I am also indebted to all my colleagues, in particular to Dr. Romain Danneau, Dr. Benjamin Scott Flavel, Dr. Wenshan Li, Dr. Rainer Kraft, Dr. Felix Pyatkov, Dr. Preeti Pandey, Dr. Han Li, Asiful Alam, Adnan Riaz, Sandeep Kumar, Anirudh Peyyety, Min-Ken Li and Marco Gaulke for their help and moral support.

Finally, yet importantly, I would like to express my gratitude to my family and friends for their continuous support across the entire duration of this thesis.

Curriculum Vitae

Personal information

Name	Pranauv Balaji Selvasundaram
Date of birth	21.11.1992

Education

03/2016 -08/2020	Doctorate	TU Darmstadt, Germany "Near Infrared Photocurrent Spectroscopy on Carbon Nanotube Devices" Supervisor: Prof. Dr. Ralph Krupke
05/2010 – 05/2015	M.Tech +B.Tech (Dual Degree)	Nanotechnology, Amity Institute of Nanotechnology, Amity University, India
	Master Thesis	Quantum Transport and Superconductivity in monolayer Graphene hBN pn-junctions

Professional Expirience

03/2016 – 08/2020	Researcher at the Institute of Nanotechnology, Karlsruhe Institute of Technology and at the Department of Materials and Geosciences, Technische Universität Darmstadt
01/2015 – 12/2015	Research assistant at the Institute of Nanotechnology, Karlsruhe Institute of Technology

Publications

Articles

[1] H. li, G. Gordeev, O. Garrity, N. A. Peyyety, P. B. Selvasundaram, S. Dehm, R. Krupke, S. Cambré, W. Wenseleers, S. Reich, M. Zheng, J. A. Fagan and B. S. Flavel. Seperation of Specific Single – Enantiomer Single – Wall Carbon Nanotubes in the Large Diameter Regime. *ACS Nano* **14**, 948-963 (2020).

[2] P. B. Selvasundaram, R. Kraft, W. Li, R. Fischer, M. M. Kappes, F. Hennrich and R. Krupke. Measuring in Situ Length Distributions of Polymer – Wrapped Monochiral Single – Walled Carbon Nanotubes Dispersed in Toluene with Analytical Ultracentrifugation. *Langmuir* **35**, 3790-3796 (2019).

[3] A. Riaz, A. Alam, P. B. Selvasundaram, S. Dehm, F. Hennrich, M. M. Kappes and R. Krupke. Near – Infrared Photoresponse of Waveguide – Integrated Carbon Nanotube - Silicon Junctions. *Adv. Electron. Mater.* **5**, 1-6 (2019).

[4] R. Kraft, J. Mohrmann, R. Du, P. B. Selvasundaram, M. Irfan, U. N. Kanilmaz, F. Wu, D. Beckmann, H. v. Löhneysen, R. Krupke, A. Akhmerov, I. Gyorni and R. Danneau. Tailoring supercurrent confinement in graphene bilayer weak links. *Nat. Commun* **9**, 1722 (2018).

[5] D. McManus, A. Dal Santo, P.B. Selvasundaram, R. Krupke, A. LiBassi and C. Casiraghi. Photocurrent study of all –printed photodetectors on paper made of different transition metal dichalcogenide nanosheets. *Flex.Print. Electron.***3**, 034005 (2018).

Conference Contributions

[1] P. B. Selvasundaram, R. Kraft, W. Li, R. Fischer, M. M. Kappes, F. Hennrich and R. Krupke. In-situ measurement of the length distribution of polymer-wrapped (7, 5) SWCNTs in solution by analytical untracentrifugation, Graphene & Co – Annual Meeting 2017, October 2017 Assouis, France, Contributed Talk.

[2] P. B. Selvasundaram, A. Riaz, S. Dehm, F. Hennrich, M. M. Kappes and R. Krupke. Photocurrent respose of carbon nanotube – semiconductor junctions, Graphene & Co – Annual Meeting 2018, October 2018 Sète, France, Poster.

[3] P. B. Selvasundaram, R. Kraft, W. Li, R. Fischer, M. M. Kappes, F. Hennrich and R. Krupke. Measuring in Situ Length Distribution of polymer Wrapped Monochiral Single-Walled Carbon Nanotubes Dispersed in Toluenen with Ananlytical Ultracentrifugation, NT-19: International Conference on the Science and Application of Nanotubes and Low- Dimensional Materilas, July 2019 Würzburg, Germany, Poster.

[4] P. B. Selvasundaram, S. Dehm, F. Hennrich, M. M. Kappes, Y. Chen and R. Krupke. NIR – photoresponse of carbon nanotube split gate junctions, Graphene & Co – Annual Meeting 2019, October 2019 Bad Herrenalb, Germany, Poster.

1 Introduction

1.1 Scope of Thesis

The entire progress in the state of the art electronics can be credited to the success of one material, and that is Silicon (Si). [1] It was made possible by improving the Si- transistor over decades by increasing the integration density of the integrated chips (ICs). The IC development has always followed the famous Moore's Law over the years, which states that the integration of number of transistors doubles every 18 months on a processor chip by reducing the transistor dimensions and increasing the operating frequency. [2] However, Moore's Law is now challenged as the Si transistors have met their physical limit by considering all the factors like scaling down the dimension, increasing the charge carrier density and mobility, using high k dielectrics along with new geometries.[1] On the contrary, due to the increasing demand of the integration density, transistors face problems like short channel effects such as tunnelling between source and drain, and high leakage currents. Due to such shortcomings, it is of great importance and interest for the industry and scientists to find a capable material with superior electrical properties to replace silicon.

Over the years and since, many materials with such superior electrical properties are subjected to tests and experiments to pinpoint the fix. One such promising material is the quasi one-dimensional (1D) carbon nanotubes (CNTs) because of their novel electrical and optical properties.[3–6] CNTs are an allotrope of carbon and their structure can be correlated to a rolled up graphene sheet. Similar to graphene, CNTs also possess sp^2 hybridized orbitals and these orbitals form the sigma bonds between the adjacent carbon atoms and the remaining p orbital forms a delocalised π electron cloud which depending on boundary condition determines the metallic or quasi metallic behaviour of the tube.[7,8] Geometrically, an individual CNT wall can be defined by the orientation of the wrapped up graphene lattice with respect to the tube axis, known as the chirality[9]. Based on the number of walls, CNTs can be classified as single-walled carbon nanotubes (SWCNTs) and multi-walled carbon nanotubes (MWCNTs).[10] Typically, the diameters of SWCNTs and MWCNTs range from 0.8nm to 2nm and 5nm to 20nm, respectively. Whereas, the length of the tubes can vary from less than 100nm up till several centimetres.

Due to their unique 1D geometry, CNTs show many attractive mechanical, thermal, electrical and optical properties. They have very high Young's modulus (~1TPa), tensile strength (over 50GPa) and breaking elongation (up to 16 %) which potentially makes them interesting as a strong reinforcement agent in composite materials, right from Atomic Force Microscope (AFM) tips up till air crafts and space elevators.[11–13] Also with its thermal stability and conductivity, CNTs are ideal candidates to replace metals in thermal conductive applications such as heat sinks and heat exchangers in electronics. Typically, CNTs are stable until 2800 °C in vacuum and 750 °C in air with a thermal conductivity > 6000 W/mK at 300 K.[14,15]

The nanotubes exhibit attractive electrical properties with their diameter and chirality dependent band gap ranging from zero to 2 eV placing them in metallic or semiconducting behaviour. Other than the low electron scattering within the 1D system and surface to volume ratio, electrical conductivity of up to 10^6 - 10^7 S/m, charge mobility of 10^5 $cm^2/(Vs)$ and current capacity as high as 1 GA/cm^2 are observed for SWCNTs which makes them more than suitable for modern electronics and sensors.[16–20] Over the years, it has also been verified that CNT based transistors can perform with sub threshold swing lower than 60mV/dec and are also compatible with CMOS field effect transistor (FET) architecture.[21]

The optical properties of SWCNTs emerge from their electronic transitions within the van Hove singularities (vHs) – the one dimensional density of states (DOS), which consists of chirality resolved peaks making them spectroscopically distinguishable.[22] Due to their nm- scale diameter, the Coulomb interaction between the optically excited electron and hole pair is strong within a nanotube.[23] These strong interactions result in sharp band to band or excitonic transitions and also a strong photon - phonon coupling within the CNTs. This results in many optical features, like electron phonon side band or Raman scattering etc.[24] Hence, CNTs have proven to be exceptional in various optical applications, such as light emitting diodes (LEDs), solar cells, optoelectronic transducers, photonics and plasmonics.[25–28]

In order to probe these properties, material procurement and device integration are two essential factors. To address the material procurement, pure semiconducting SWCNTs (s-SWCNTs) separated from the metallic SWCNTs (m-SWCNTs) are needed. It is not efficient to separate during the synthesis methods such as chemical vapour deposition (CVD), arc discharge, laser ablation, plasma torch etc.[20,29–33], even with selective m-SWCNT etching.[33,34] This occurs due to the possibility of multiple preferential species growth in a synthesis process. Hence, further separation processes are required to sort the SWCNTs with respect to their chirality after synthesis.

In practice, the post synthesis separation of CNTs can be categorized into solid substrate based and solution based methods.[35] Using external heat or high currents to burn off or remove m-SWCNTs is known as substrate based purification, commonly used in techniques like microwave purification[36] and electrical breakdown[37]. The tube density prepared by these techniques is quite low due to the limitation from the substrate area, making them detrimental to the device performance. On the other hand, the solution based techniques include selective chemistry[38–40], ultracentrifugation[41,42], chromatography[43,44] and electrophoretic separation[45]. Based on these purification techniques, separation of specific SWCNTs has well improved compared to their synthesis techniques. However, it still includes certain drawbacks like functionalisation of the material and low yield of the targeted SWCNTs. In particular, SEC performed with organic solvents and poly-fluorene based polymer wrapping has shown to be one of the high yielding specific sorting abilities towards generating dispersed SWCNTs with >>99% semiconducting content in a single sonication or ultracentrifugation step.[46–48] Using such a method would yield ultra - high purity s – SWCNT for large scale applications.

When it comes to the CNT integration, the major challenge is to assemble individual tubes rather bundles with precision on to the chip, along with reproducibility and packing density optimization. Methods like shear force guided SWCNT alignment, so far lack control over orientation of alignment and positioning of the SWCNT arrays.[49,50] Also, Langmuir- Schaefer method is a technique that has been widely used for fabricating single molecule thick film with control over the packing density but has no control over forming double layered CNT arrays, which can be detrimental to the electrical behaviour due to the inter-tube screening effect.[40,51] On the contrary, dielectrophoresis (DEP) has proven to be more versatile to sort and deposit simultaneously.[52,53] Unlike the regular electrophoresis process, DEP does not need its particles to be charged. It is effectively driven by the dielectric properties (permittivity and conductivity) of both particle and solvent along with the size and geometry of the particle. The technique makes use of induced dipole moments on applying inhomogeneous field, giving precise control over deposition and could be scaled by optimization of electric field and electrode geometry.[52,54]

CNT integration was first demonstrated in Karlsruhe[52] using (AC) DEP to assemble them on to devices separating the individual tubes from the bundles.[55] The technique has a potential to fabricate individual devices, displaying potential for industrial fabrication.[56] However, SWCNT DEP at first was mainly concentrated on the metallic species rather than semiconducting ones due to their dielectric properties as the

former one is much larger, making them preferential for DEP. In order to achieve quality s-SWCNT deposition, a low dielectric media should be preferable in order to reduce the screening effects from the media and increase the polarizability of the nanotube.[57] The frequency window for achieving the conditions for DEP for s-SWCNT is limited by the electrolysis of the electrodes and formation of electrical double layers (EDLs) due to the ions in the media at low frequency. Also the DEP parameters should be tuned down or up according to the decrease or increase in the conductivity of the substrate.[58]A method to characterize such DEP deposited CNTs is photocurrent spectroscopy.

Due to the quasi 1D structure of SWCNTs, the exciton interband transitions between the corresponding vHs dominates the optical transitions of nanotubes. Generating an exciton and the probability of converting it to free charges depends on the binding energy, which can be influenced by the external applied electric field.[59] These free charges when collected at the nanotube ends in response to the illumination with light results in a photocurrent. Typically, photocurrent is strongly correlated with the optical absorption of the nanotube and depends on the polarization of the incident light.

The photocurrent generation mechanism in CNTs can be broken down into phonon assisted and electric field assisted. The phonon assisted or thermal based photocurrent generation is independent of exciton generation or relaxation process and can be further classified into bolometric as well as photothermoelectric effect (PTE). The bolometric effect dominates when a DC bias is applied across the nanotube channel and can efficiently dissociate the charge carriers across the entire nanotube channel.[60–62] In absence of a DC bias, the CNT devices generate either a PTE or a photovoltaic (PV) /electric field assisted photocurrent. Both of these mechanisms exist together with their relative dominance on the nanotube type and electronic assembly of the CNT film along with the device geometry.[63–65] PTE works on the Seebeck effect, where the temperature difference is induced by absorption of light by two materials, generating a potential gradient due to the difference in the Seebeck coefficients between the metal electrodes and the nanotubes. Whereas, the PV works on the electric field gradient generated along the nanotube film or at the contacts. Along the nanotube channel, the electric field gradient is generated by an electrostatic gating (split gate) and at the edge of the nanotube- metal contact, electric field gradient is generated due to the formation of Schottky barrier due to the difference in work-function between the nanotube film and the metal contact. But the Schottky barrier based photocurrent generation is more prominent in smaller diameter tubes, due to a larger difference in the fermi levels between the nanotubes and the metal contact. To realise photocurrent through electrostatic doping, a larger contact length is desired between the nanotube and the metal contact. Also, a larger diameter tube or a lower work function for a metal contact should be considered, minimising the work-function difference between the nanotube and metal contact.

Although, Riaz et.al[66] reported a curious behaviour, that when a few CNTs were contacted with a bulk semiconductor creating a nanotube semiconductor junction, it was observed that there was a change in the direction of the photocurrent generated along the spectrum, each attributed to the contribution from the nanotube and the silicon electrode. The photocurrent observed on the nanotube active regions was proposed to be from the PV effect and the rest of the opposite photocurrent signature due to a photogating effect in the bulk semiconductors. However, this was reported to be true for the smaller diameter tubes and not for the slightly larger diameter tubes present in the multi-chiral suspension used in the experiment.[66] On continuing the work for better understanding with even smaller diameter tubes, a similar signature in the photocurrent was observed suggesting that the competing polarities generated from the photo-gating effect is occurring at different layers of the substrate.

1.2 Thesis Framework

In this thesis, the best possible condition for the photocurrent generation was investigated in the near infrared (nIR) region of the light spectrum along with the influence of bulk silicon on the photocurrent when in contact with nanotubes, as silicon is an ideal waveguide material to channel light to nanotubes. In Chapter 2, a detailed theoretical background is presented to comprehend all the experimental measurements and their interpretation in the following chapters. The main focus of this chapter is driven towards the introduction of the structure and geometry of the SWCNTs, along with their structure driven optical and electrical properties.

The experimental methods on production or synthesis along with purification and length sorting are explained in Chapter 3. It includes the different synthesis techniques along with types of SWCNT dispersion and their length sorting by SEC and a new length analysis technique is introduced. The new length analysis technique is compared with the atomic force microscopy (AFM) method as a reference, to gauge the new technique using analytical ultracentrifugation (AUC). The statistical number distributions obtained from each method are compared for a monochiral (7, 5) suspension. Chapter 4 is focused on the photocurrent spectroscopy technique, where the concepts and working principles of the different instrumentations used in the photocurrent spectroscopy are explained in detail along with their calibration.

In Chapter 5, favorable conditions for the photocurrent generation are discussed in detail. In comparison to silicon, the photocurrent spectra from the sapphire substrate on same type of devices shows a clear CNT specific spectrum within the nIR region. In addition, different substrate geometries were investigated and discussed to maximize the photocurrent generation, with the main focus towards split gate geometry to create an electrostatic pn-junction. The devices were fabricated by integrating CNTs from a toluene based multi-chiral dispersion with a high concentration of (9, 8) SWCNTs using DC DEP. The devices were then electrically characterized and their photocurrent spectra were measured for different gate configurations along with their photocurrent-gate voltage map. In conclusion it was found that the Schottky barriers dominate the pn- junction for the given nanotube dispersion used. The photocurrent enhancement from the pn- junction can be realized only if the Schottky barrier height can be reduced or a larger diameter SWCNT can be used.

As the SWCNTs were targeted to potentially be single photon detectors, the light to be detected is coupled on to a silicon waveguide. Hence, the behavior of SWCNT-silicon junction is focused in detail in Chapter 6. Here, different nanotube to silicon junctions are investigated with photocurrent spectroscopy in detail. Also, the photocurrent mechanism is deduced across these junctions by addressing different parts of the photocurrent spectra and substrate effects. The photocurrent studies are mainly conducted on few chiral and monochiral (6, 5) suspensions integrated using DC DEP on silicon on insulator (SOI) and silicon on sapphire (SOS) substrates. The fabricated devices were characterized electrically and their photocurrent spectra were collected. The comparison of the photocurrent spectra collected concludes that the photocurrent observed is from the substrate and not from the SWCNTs bridging the electrical contacts.

2 Theoretical Background

2.1 Single walled Carbon Nanotube

Single-walled carbon nanotubes (SWCNTs) constitute an allotrope of carbon with a two dimensional lattice structure rolled up to a seamless cylinder. Since their discovery in 1991, carbon nanotubes (CNT) have shown a great potential to replace other bulk material attributed to their quasi 1D nanostructure. They exhibit unique optical, electrical and chemical properties making them ideal for various applications including photonics.[8] Carbon has six electrons with orbital occupancy $1s^2 2s^2 2p^2$. The atomic orbitals in carbon can mix with one another leading to sp^x hybridization (where x can be 1, 2 or 3) that can define its geometry as well as its electronic properties. For instance, alkynes (sp) and graphene (sp^2) can act as conductors, whereas diamond (sp^3) is a wide-band gap insulator. As rolled up single layer graphene sheets, SWCNTs also possess similar sp^2 hybridized orbitals. These orbitals form the σ bonds between adjacent carbon atoms in the graphene plane while the remaining unsaturated p orbital forms a delocalized π electron cloud perpendicular to the graphene sheet. Since the electron cloud lies near the Fermi level, it determines the metallic or quasi - metallic behaviour of graphene and that of SWCNT as well.

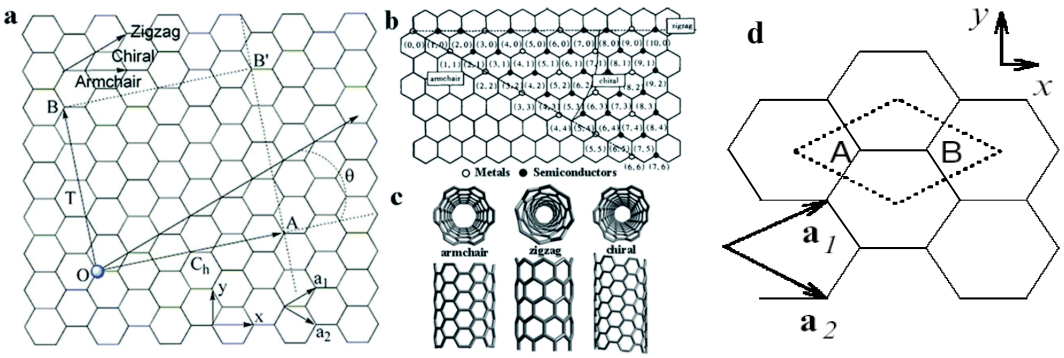

Figure 2.1(a) Schematic plot of the chiral vector ($\mathbf{C}_h$) in a graphene lattice. (b) The relationship between the integers (**n**,**m**) and the metallic or semiconducting nature of nanotubes. (c) The structures of "armchair", "zigzag", and "chiral" nanotubes. Copyright 2011 RSC[67]. (d) Unit cell of graphene, along with the lattice vectors.

The structure of SWCNTs is defined using the graphene lattice vectors. The unit cell is spanned over the unit vectors $\overrightarrow{a_1}$ and $\overrightarrow{a_2}$ in the shape of a rhombus containing two carbon atoms in the centre A and B. Geometrically, the length of both the vectors is obtained using the distance between the neighbouring atoms $a_{cc} \cong 1.42\text{Å}$ where $|\overrightarrow{a_1}| = |\overrightarrow{a_2}| = a_0 = \sqrt{3}a_{cc} = 2.46\text{Å}$ and form an angle of 60°.[68] The chiral vector $\overrightarrow{C_h}$, is perpendicular to the nanotube axis and is mathematically represented as,

$$\overrightarrow{C_h} = n\overrightarrow{a_1} + m\overrightarrow{a_2} \qquad (2.1)$$

where $\overrightarrow{a_1}$ and $\overrightarrow{a_2}$ are the basis vectors of graphene and n and m are integers ($0 \leq |m| \leq |n|$). (n, m) is called the chiral index or chirality of the nanotube and is unique for a particular tube. Based on this, the chiral vector $\overrightarrow{C_h}$ is the one along which the graphene sheet is rolled up to form a SWCNT, which means

that $\overrightarrow{C_h}$ connects two equivalent atomic sites along circumference of the tube (Figure 2.1). From the chiral index, the nanotube diameter and chiral angle $\theta_{(n,m)}$between $\overrightarrow{C_h}$ and $\overrightarrow{a_1}$ can be calculated through[68,69]

$$d_{CNT} = \frac{|\overrightarrow{C_h}|}{\pi} = \frac{\sqrt{3}a_{cc}}{\pi}\sqrt{n^2 + nm + m^2} \tag{2.2}$$

$$\cos\theta_{(n,m)} = \frac{\overrightarrow{a_1} \cdot \overrightarrow{C_h}}{|\overrightarrow{a_1}| \cdot |\overrightarrow{C_h}|} = \frac{n + m/2}{\sqrt{n^2 + nm + m^2}} \tag{2.3}$$

The geometry of CNTs is relevant not only for understanding the physical properties of nanotubes but it also simplifies the calculations as well. The electronic properties of CNTs vary dramatically for carbon nanotubes with adjacent chiral indices. Taking into account the symmetry of rotation of the graphene lattice for the SWCNTs, the magnitude of each chiral angle $\theta_{(n,m)}$ is correlated to the chirality of every single tube (as stated above) and is restricted within $0° \leq \theta_{(n,m)} \leq 30°$. When $m = 0$, indicating $\theta_{(n.m)} = 0°$, the circumference of the tube gives a zig-zag pattern, hence defining them as zig-zag tubes. When $n = m$, meaning $\theta_{(n,m)} = 30°$, the tubes are defined as armchair due to its armchair pattern along the circumference. Other tubes $(n \neq m \neq 0)$are known as the chiral tubes (Figure 2.1(c)).[70] Accompanying the chiral vector $\overrightarrow{C_h}$, a translational vector $\vec{T}$ which denotes the translational period in the tube-axis direction, is needed to span the unit cell of the nanotube (Figure 2.1(a)[71]).

2.2 Band structure of Graphene

In general, the electronic band structure of graphene is calculated using ab - initio calculations or the empirical tight - binding approximations. In the latter approximation, the valence electrons are confined within atoms but interact with those of neighbouring atoms owing to the small interatomic distances. The electronic band structure is there of calculated by superimposing the constituent electronic wave functions. The typical electronic band structure of graphene is represented in Figure 2.2. The tight-binding electronic dispersion model for graphene that considers the third nearest neighbour interaction is in good agreement with the ab-initio calculation in the vicinity of the high symmetry points Γ, K and K´. Consequently, the energy dispersion relation in these regions is simplified to,

$$E(k) = \frac{\epsilon_{2p} \pm \gamma|E_s(k)|}{1 \pm s|E_s(k)|} \tag{2.4}$$

where the phase change in electron wave function $E_s(k)$ is described as follows $E_s(k) = |f(k)| = \sqrt{1 + 4\left(\cos\frac{1}{2}k_y\right)^2 + 4\cos\left(\frac{\sqrt{3}}{2}k_x\right)\cos\left(\frac{1}{2}k_y\right)}$ where s is the value for the overlap, ϵ_{2p} is the electron's onsite energy and γ is the hopping integral for graphene and are determined by theoretical calculations, as an empirical fitting parameters for experimental data.[72] The ± denotes the bonding state of the valence band (+) and the antibonding state of the valence band (-). Also, the π and π* conduction and valence band meet at the K - points of the Brillouin zone (BZ) and are almost linear in the vicinity of the Fermi level.

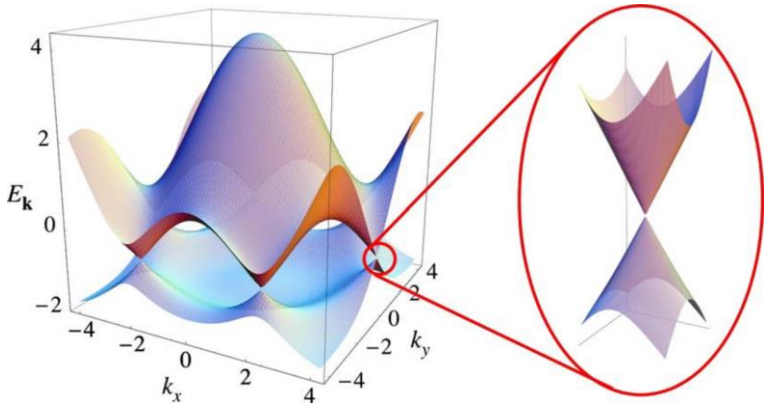

Figure 2.2: Band structure of graphene – Electronic dispersion in the honeycomb lattice.[73]

2.3 Band Structure of Single Walled Carbon Nanotubes (SWCNTs)

With the 2D dispersion relation of graphene, it is possible to deduce the energy dispersion in the SWCNTs by imposing the periodic boundary conditions known as the zone folding (ZF) approximation. The method results in quantization of the continuous band in graphene to discrete sub-bands. The BZ in the reciprocal space for SWCNTs consist of equidistant lines matching the number of graphene hexagons in each cell of the nanotube. The BZ is define by two vectors, $\overrightarrow{k_{||}}$ running along the axis of the SWCNTs and $\overrightarrow{k_{\perp}}$ running perpendicular to the tube axis. Figure 2.3 shows the first BZ and electronic band structure of (4, 4) arm-chair nanotube presented on top of the 2D representation of the first BZ of graphene ($\epsilon_{2p} = 0, s = 0, \gamma = 2.9$) . The plot is the resultant from tight binding calculations of electronic band structure of SWCNTs using the ZF approximation.[74] For an infinitely long SWCNT, the wave vector $\overrightarrow{k_{||}}$ is continuous (Equation 2.5) whereas, the wave vector $\overrightarrow{k_{\perp}}$ is quantized (Equation 2.6) along the $\overrightarrow{C_h}$ direction

$$\overrightarrow{k_{||}} \cdot \overrightarrow{C_h} = 0 \tag{2.5}$$

$$\overrightarrow{k_{\perp}} \cdot \overrightarrow{C_h} = \pi d_{CNT} k_{\perp} = 2\pi\mu \tag{2.6}$$

Here, d_{CNT} is the nanotube diameter and μ is an quantum number related to the number of graphene hexagons in a unit cell of the SWCNT. The number of hexagons $N = 2(n^2 + nm + m^2)/\gcd(2n + m, 2m + n)$ (where gcd- greatest common divisor) and the integer μ is given by $-\frac{N}{2}, \ldots -1, 0, 1, \ldots, \frac{N}{2}$ resulting in N lines of allowed k-states separated by π/d_{CNT}. The factor 2π comes from the phase difference of the electron wavefunction along the circumference of the SWCNT. [For more information, Thomsen et al.[7]].

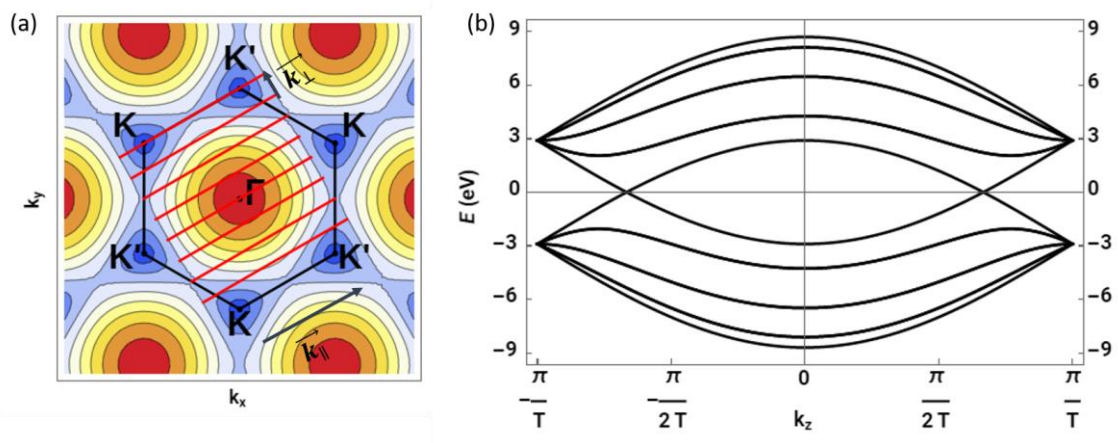

Figure 2.3 : (a) First Brillouin zone and (b) Electronic band structure in for (4, 4) armchair nanotube.[calculated with wolfarm alpha[74]]

Although the ZF approach yields reliable descriptions for electrical properties of SWCNTs, it fails for smaller diameter tubes ($d_{CNT} \lesssim 1nm$) to consider a shift of the k - points due to the curvature effect of the Fermi vector $\overrightarrow{k_F}$ from the BZ corners (K) of graphene. For those cases, the ab initio method is used to calculate the band structure for larger diameter SWCNTs.[75]

The density of states (DOS) at higher energies comprises several singularities called as the van Hove singularities (vHs)$n(E) \sim 1/\sqrt{E}$. In SWCNTs, the DOS is given by

$$n(E) \propto \sum_i \int dk \delta(k - k_i) \left| \frac{\partial E_i^{\pm}}{\partial k} \right|^{-1} \tag{2.7}$$

with $E_i^{\pm}$for the i^{th}Eigen values of the band energy of graphene under the tight binding model, given by $E - E_i^{\pm}(k) = 0$. Due to the high DOS at the vHs, physical properties like optical absorption/ emission[76], resonant Raman scattering[77] etc. will be pronounced at these energies.

2.4 Optical Properties of Single Walled Carbon Nanotubes

The electronic states of SWCNT within an energy interval give rise to many optical properties. As mentioned in the section above, the local symmetry of the SWCNTs along with their curvature effect gives rise to these energy levels.[78] These energy levels can be probed by several optical spectroscopic techniques like UV - Vis absorption spectroscopy, photoluminescence etc. Figure 2.4 shows the typical density of states (DOS) of (4, 0) and (4, 4) respectively (calculated with Wolfarm alpha). The presence of DOS has been verified by scanning tunneling microscopy (STM)[79] and have direct implications on charge transport and optical properties of the SWCNTs.

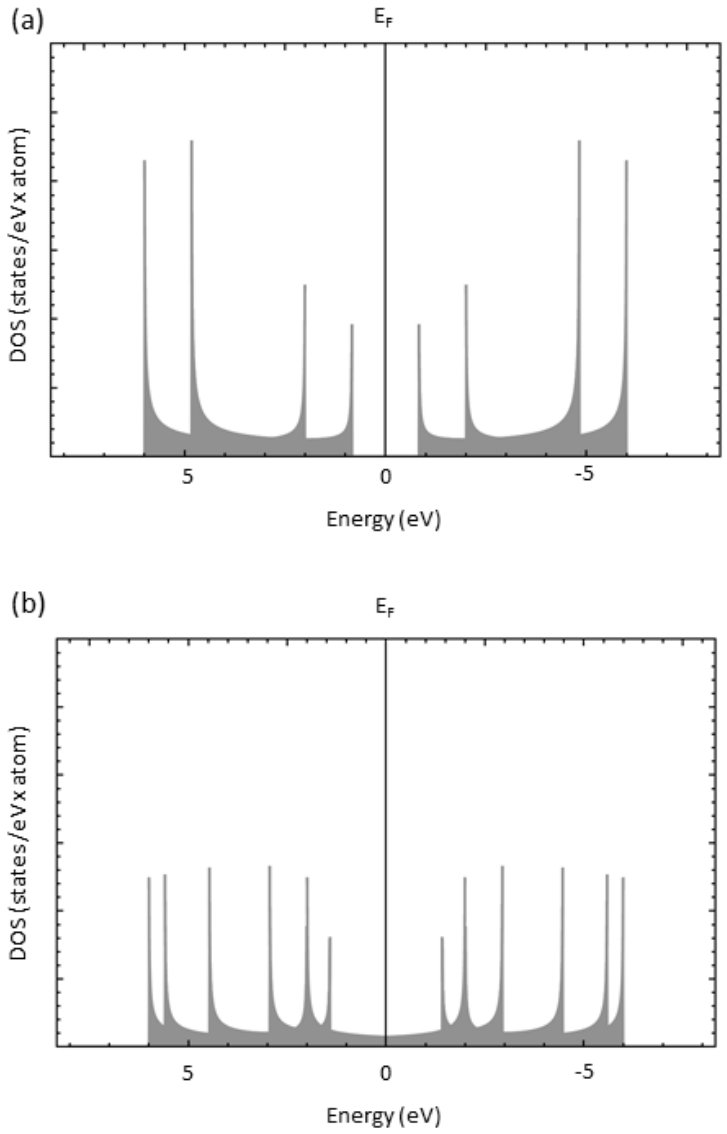

Figure 2.4: The plots show the electronic density of states (DOS) computed from the tight-binding method for (a) semiconducting nanotube (4, 0) and (b) metallic nanotube (4, 4).

2.4.1 Absorption

On illumination with linearly polarized light parallel to the nanotube axis, the optical transition (E_{ii}) between the two energy levels defined by the vHs side-bands with same angular momentum number μ is allowed[80] These optical transitions in semiconducting tubes are commonly denoted as S_{11}, S_{22} etc. and M_{11}, M_{22} etc. in metallic tubes. Figure 2.5 shows the possible optical transitions in SWCNTs. As the energy levels are strongly dependent on the nanotube chiral properties, the optical absorption measurement techniques can be used to probe the energy levels and define the chirality of the SWCNTs. In principle, the photon of energy S_{11} or S_{22} is absorbed to excite the electrons to the corresponding excited state forming an electron hole pair. The S_{11}, S_{22} and other similar higher order transitions are possible when the

incident polarized light is aligned or parallel to the SWCNT axis in which the selection rule $\Delta\mu = 0$ applies. On the other hand, the transitions like S_{12} are allowed only when the incident light is polarized perpendicular to the SWCNT axis where the selection rule is $\Delta\mu = \pm 1$. However, this cross-polarized excitation is suppressed by the antenna effect or the depolarization effect[81,82] due to the geometrical anisotropy of the SWCNTs. Polarization induced in SWCNTs by incident light is opposite to the electric field causing the effect, nevertheless cross-polarized photoluminescence has been reported from several SWCNTs despite its low efficiency.[83]

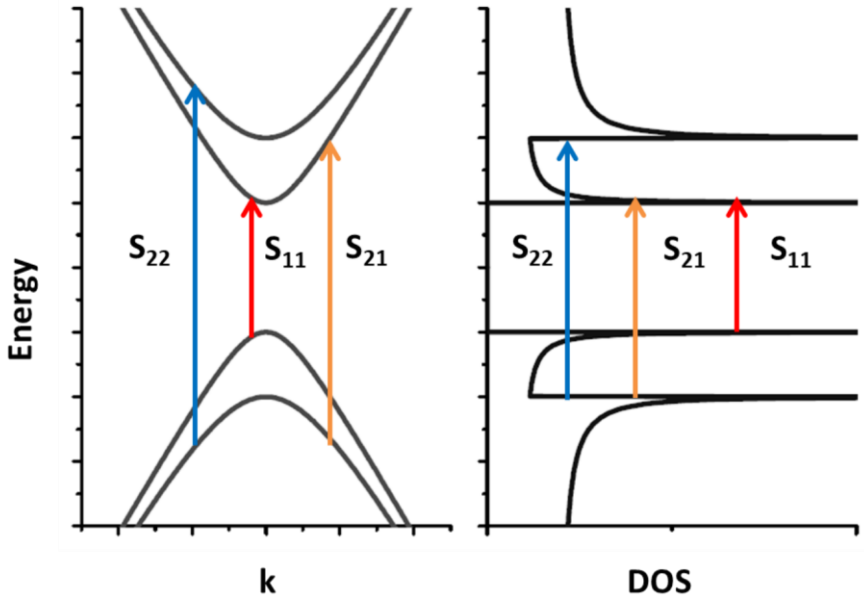

Figure 2.5: The allowed transitions are indicated with arrows. The S_{11} and S_{22} transitions are resultant of excitation with SWCNT axis aligned with the polarized light, whereas the S_{12} transition is a resultant of cross polarized excitation with respect to the nanotube axis.

2.4.2 Photoluminescence

Photoluminescence excitation (PLE) is widely used to characterize semiconducting SWCNTs.[84,85] It is performed by exciting SWCNTs over a wide range of wavelengths and detecting the emission from the SWCNTs. Typically, the relative abundance of (n, m) species in the specimen could be deduced from the relative emission intensity. Figure 2.6 shows the photoluminescence process that takes place after an optical excitation. In general, the electrons excited from the valence band to the conduction band can radiatively recombine emitting a photon with an energy equivalent to S_{11}.[86] Electrons from the higher bands can also relax to the first conduction band non - radiatively through electron-phonon relaxation and then continue to recombine, to the ground state.

However, this technique is not suitable for metallic tubes as the excited free carriers relax to the Fermi state in a phonon assisted process leading to non-radiative recombination. Hence, light emission from metallic-SWCNT (m-SWCNT) or bundles of semiconducting and metallic SWCNTs are strongly quenched and not observed under PLE characterization.[87]

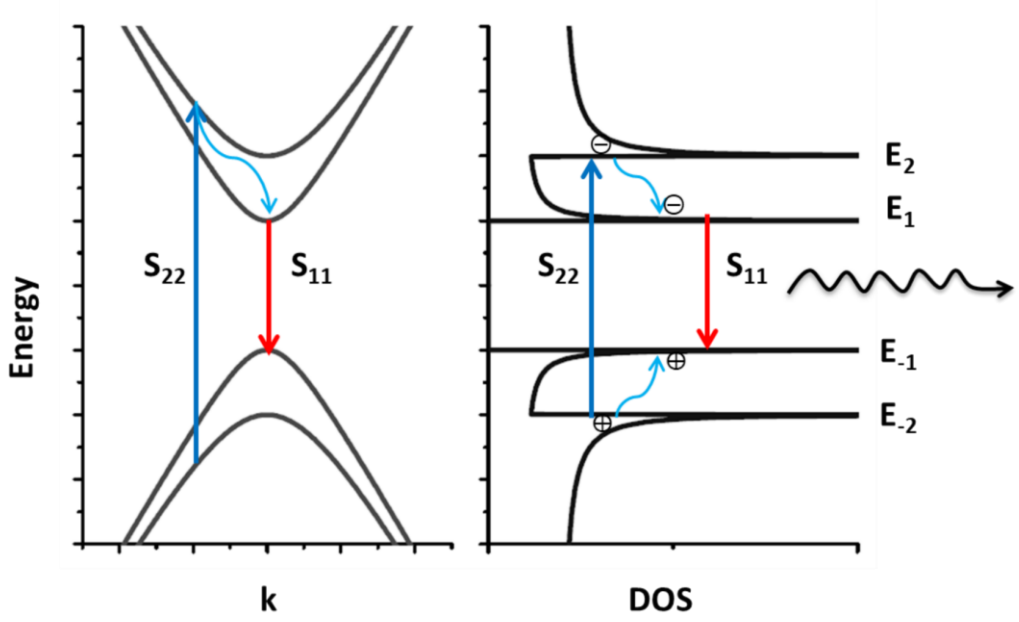

Figure 2.6: Schematic representation of absorption and emission from a semiconducting SWCNT. The relaxation of the S_{22} excited electron to S_{11} occurs with a phonon assisted relaxation and the S_{11} relaxation is emitted as a photon.

Both absorption and photoluminescence spectroscopy allow a comparison of different nanotube species' density in a sample. An absolute value can be determined with the corresponding (n, m) dependent optical absorption efficiencies and cross sections. Efficiency and transition are strongly dependent on the dielectric environment surrounding the tube.[88] Also, relaxation lifetime of the excited carriers has been addressed in literature using pump probe experiments. The timescale ranges in femto-seconds depending up on type of transitions. However, transitions in bundles are expected up to a pico second due to tunneling into the neighboring metallic or larger diameter tubes.[89–91]

2.4.3 Excitons in Carbon Nanotubes

The Coulomb interaction between an electron and a hole forming an exciton in a SWCNT is strongly enhanced compared to the bulk semiconductors. Although the optical properties till the previous section were explained using the single particle model, the single particle interband theory deviates substantially from the experimental observations due to enhanced electron hole pair interaction.[92,93] Hence, the many body effects come into play, where the electron – electron and electron –hole interactions play a major role in the exciton physics in a SWCNT. Experimentally, in absorption studies, it was reported that the energy transition ratios (S_{22}/S_{11}) were inversely dependent on the diameter instead of the remaining constant from the tight binding calculations.[94] Also, the excitonic nature probed by two photon absorption spectroscopy indicated the existence of excitonic states just below or lower than the free particle continuum states even at the room temperature.[92,93,95–99]

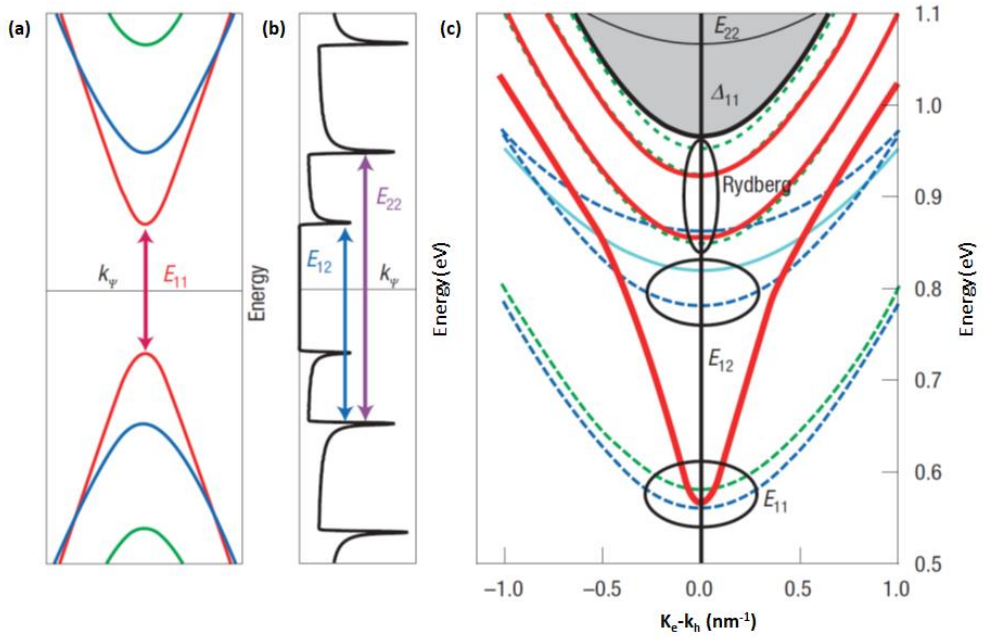

Figure 2.7: Band Structure of a (19, 0) semiconducting SWCNT, and corresponding (b) single – particle based density of states. (c) Low-lying exciton states of a (19, 0) CNT. Dipole-allowed or 'bright' transitions are solid lines and forbidden or 'dark' transitions are green ($k_{\perp} = \pm 2k_{\perp min}$) and navy ($k_{\perp} = 0$) dashed lines. The parallel ($k_{\perp} = 0$) or perpendicular ($k_{\perp} = \pm 3k_{\perp min}$) polarizations with respect to the CNT axis of a state relating to an allowed transition are indicated by red and blue solid lines, respectively. Black ellipses indicate the states relating to the following first allowed transitions: E_{11} for parallel and E_{12} for perpendicular polarizations. The state relating to the second allowed transition (E_{22}) and the free-particle continuum (Δ_{11}) are also shown in black. The ellipse labelled 'Rydberg' indicates Rydberg states with k = 0. k_e is the electron wave vector and k_h is the hole wavevector. ([Reproduced from 100])

Excitons in CNT constitute a series of bound states are analogous to the Rydberg series in an atom just below the free particle continuum. The Rydberg series is due to the two particle interaction within atomic hydrogen. Similarly, bound excitonic states can be found in semiconductors. The excitonic states are defined by the following equation

$$\mathrm{E^n} = \mathrm{E_{gap}} - \frac{\mathrm{E^R}}{\mathrm{n^2}} \tag{2.8}$$

where $\mathrm{E_{gap}}$ is the band gap energy and $\mathrm{E^R}$ is the the Rydberg energy. In CNTs, the electron density is confined to the plane of the rolled graphene sheet. Excitonic wavefunctions are expected to be delocalized along the circumference of the tube and extend along the tube axis. Hence the modified Rydberg's expression for the SWCNTs is as follows

$$\mathrm{E^n} = \frac{13.6\ \mathrm{eV}}{\mathrm{n^2}} \frac{\mu^*}{\mathrm{m_e}} \frac{1}{\varepsilon^2} \tag{2.9}$$

Here, μ^* is the reduced effective mass of the exciton, $\mathrm{m_e}$ is the effective mass of the electron and ε is the dielectric constant. The ability of the exciton to be influenced by the external applied electric field is determined by the dielectric constant. In some cases, the polarized medium can compensate an external electric field, so that the internal electric field is smaller. This is known as dielectric screening and is the reason for spectral shifts when characterizing CNTs in various solvents,[101,102] as well as embedded in composite materials[103] using photoluminescence spectroscopy. The repulsive forces between the electrons in

a tubes leads to a blue shift of the continuum states known as the band gap renormalization and is countered by the electron hole interactions that are responsible for the formation of the excitons. The optical transition energies can be expressed as follows

$$E^n = E_g + E_{ee} - E_{eh} \tag{2.10}$$

where E_g is the free carrier continuum states or the single particle band gap, E_{ee} and E_{eh} are the electron – electron and electron-hole interaction energies respectively.[100]

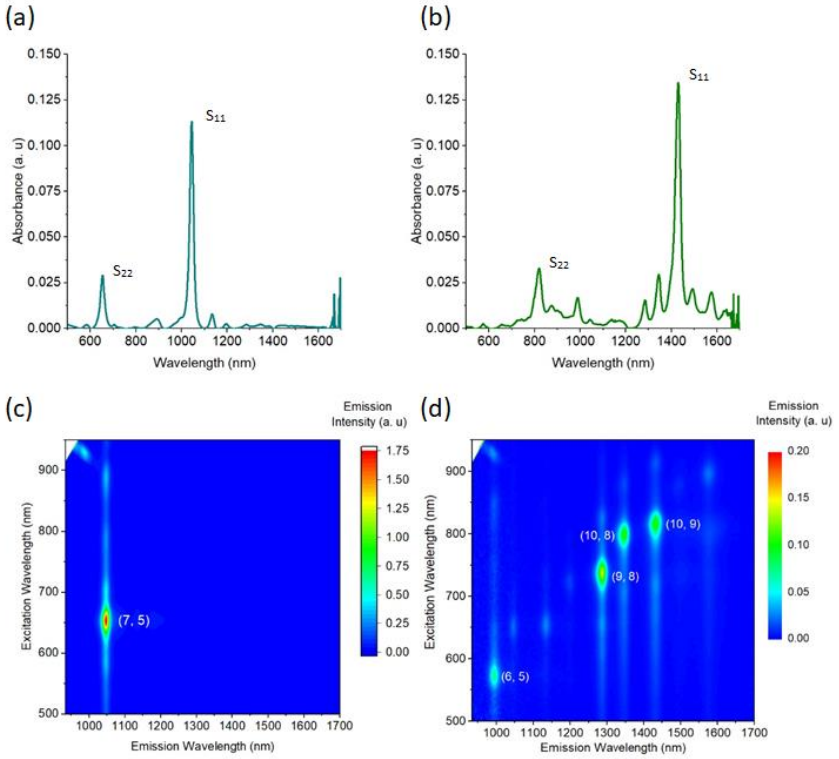

Figure 2.8: UV- Visible absorption spectrum of (a) monochiral (7, 5) and (b) multichiral CNTs with majority of (9, 8) along with the photoluminescence excitation map in (c) and (d) respectively.

The electron hole interaction energy is better known as the exciton binding energy $E_{eh} = E_b$. The binding energies E_b of excitons have been theoretically predicted and measured to be as large as several hundred meVs for s-SWCNTs[97] and tens of meVs for m-SWCNTs being the reason of reduced screening effect within the nanotube.[104] The dependence of E_b on the diameter, chirality and the ambient dielectric properties was studied by Perebeinos et al.[105] and described as

$$E_b \approx A_{CNT}\left(\frac{d_t}{2}\right)^{\propto-2} m^{*(\alpha-1)}\,\varepsilon^{-\alpha} \tag{2.11}$$

where ε is the dielectric constant of the medium, m^* the effective mass, d_t the CNT diameter, and the parameters $\alpha = 1.4$, $A_b = 24.1$ eV, derived by solving the Bethe - Salpeter equation. Most importantly,

E_b is inversely related to the CNT diameter and the surrounding dielectric environment ε.[106] In CNTs, the binding energy E_b was determined to be 0.4 eV to 1 eV,[96,97] which is about two order of magnitude larger than bulk semiconductor material.

In SWCNTs, due to the combination of their 1D structure and electronic property of graphene, the Coulomb interaction plays an important role in the band structure and the exciton effect in optical spectra. The presence of two valleys associated with the K and K' points at the corner of the first Brillouin zone, and the electron spin, the exciton states have a degeneracy of 16 in the lowest order ***k·p*** approximation.[107] These 16 degenerate exciton states are classified into four singlet states and twelve triplet states, out of which, only one singlet state with matched wavenumber and spin is optically active (bright exciton state), and the remaining fifteen are optically inactive (dark exciton states). These dark exciton states have been experimentally observed using temperature - dependent photoluminescence spectroscopy,[108–111] magneto - optical spectroscopy, electro - absorption spectroscopy[108] and even photocurrent spectroscopy.[112] This is because a dark exciton with a non-zero momentum can become visible through coupling to a phonon.

Figure 2.8 shows an example of the optical absorption spectrum and the PLE map of single (7, 5) SWCNTs and a multichiral suspension. The S_{11} and S_{22} regions are clearly visible as sharp peaks in the spectrum indicating the dominance of excitonic behavior over continuum transitions. The PLE maps are generated by exciting the CNTs over the wide range of wavelength as shown in Figure 2.8. Such maps show spectral features unique to different (n, m) species. With the PLE map, tables have been generated and are used for the assignment of the (n, m), as a metric to sort the CNTs. Even with certain shifts in the S_{11} and S_{22} peaks from the dielectric environment around the tubes,[113] it is still possible to deduce the different (n, m) species present. Although higher order transitions (S_{33}, S_{44} etc.) are difficult to observe and identify in the absorption spectra due to an overlap with a strong π - plasmon background,[114] they can distinctly appear in the PLE maps.[115]

2.5 Electronic Properties of Single Walled Carbon Nanotubes

The SWCNTs are more synonymous with the band structure of graphene. Especially the metallic SWCNTs have sub-bands intersecting at the symmetric Fermi point. Since Fermi points contribute a forward and a backward wave-vector, there are 4 forward and backward electron states considering the spin degeneracy at absolute zero. Assuming no scattering, the quantum conductance from each state would be

$$G_0 = \frac{e^2}{h} = (26\text{k}\Omega)^{-1} \tag{2.12}$$

Including the elastic scattering of charge transport in SWCNTs based on the Landauer theory,[116] the total conductance of all four states is

$$G = G_0 \sum T_i \tag{2.13}$$

On elaborating

$$G = \frac{4e^2}{h} \sum_i \int_{-\infty}^{\infty} \frac{df}{dE} \frac{[E - E_F]}{k_B T} T_i(E) dE \tag{2.14}$$

where $T_i(E)$ is the transmission probability of an electron at the i^{th} sub band at the Fermi level and df/dE is the energy derivative of the Fermi function. For an ideal m-SWCNT, the conductance is calculated to be $155\mu S$ considering T=1. The electron phonon scattering is strongly suppressed at low bias in SWCNTs unlike the bulk traditional metal due to their availability of fewer unoccupied electronic states which needs larger momentum transfer.[117] The scattering is reduced due to 1D structural confinement of nanotubes, only forward and backward scattering is possible, such that phase space for scattering is reduced. Typically, it has been found that the mean free path (l_{e-ph}) ranges $\sim 0.5\mu m$ at the room temperature for scattering.

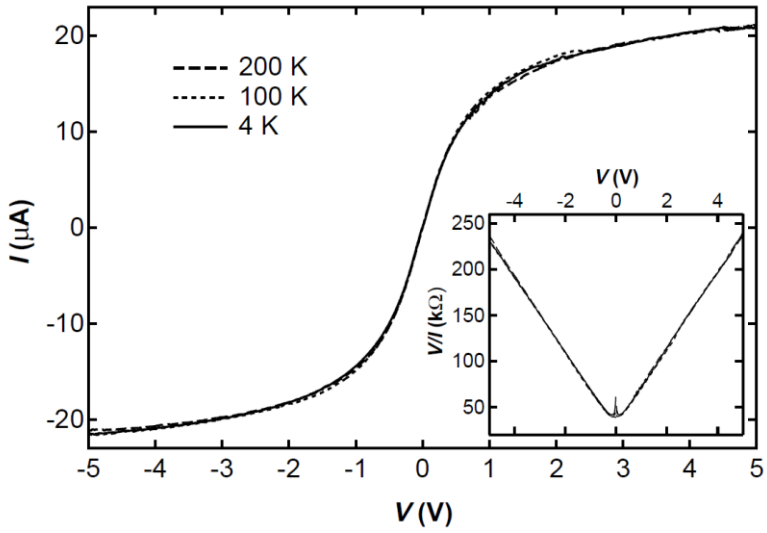

Figure 2.9: I-V Characteristics of SWCNT device at different temperatures along with the change in the resistance with respect to the voltage as the inset [reproduced from [118]].

Increasing the bias across the nanotube significantly increases the electron-phonon scattering, which leads to the increase in the resistance of the SWCNT. This applied bias, leads to a gain in kinetic energy which eventually leads to the emission of optical phonons about 0.18 eV, which have shown to couple strongly to the electronic system. SWCNTs are capable to carry currents up to 20μA (Current density of $10^8 A/cm^2$) without any degradation. The IV characteristics of the SWCNTs are constant till the optical phonon emission starts, beyond which it saturates. Thus in order to increase the current capacity, the emission have to be suppressed by scaling down the length of the nanotubes used which reduces the scattering and has been experimentally proven.[119,120]

Compared to the metallic SWCNTs, the semiconducting SWCNTs have a different band structure as discussed above. The best device configuration for putting them to test is the field effect transistor (FET). In s-SWCNTs the band gap and the mobility is much higher compared to bulk semiconductors making them suitable for high performance FETs.

2.6 Dielectrophoresis

The motion of dielectric particles under the presence of an inhomogeneous external electric field is called dielectrophoresis (DEP). The motion of the CNTs is mainly determined by the local electric fields creating imbalanced forces induced from the induced dipoles of the nanotubes. Depending on the applied electric

field, a favorable environment is created for nanotube deposition on targeted regions. Other than the dielectrophoretic forces, other effects like gravitational forces and Brownian motion also influence the nanotube motion during DEP.[121] DEP was primarily introduced as a method for separation of metallic from semiconducting nanotubes[52] but in recent times, its more prominently used for assembling the solvent suspended nanotubes on device structures.[52,56,122]

2.6.1 Polarizability of SWCNT

In presence of a uniform electric field $\vec{E}$, a dipole moment $\vec{p} = \alpha\vec{E}$ is induced, where α is the polarizability tensor of the nanotube. The tubular structure of the SWCNTs has only two non – zero tensor components existing out of the three Cartesian coordinates. The two non–zero components are the parallel $\alpha_{\parallel}$and perpendicular $\alpha_{\perp}$ to the nanotube axis.

$$\alpha_{\parallel} \sim \frac{d_{CNT}}{2\Delta E^2},\ \alpha_{\perp} \sim \frac{d_{CNT}^2}{4} \tag{2.15}$$

where d_{CNT} and ΔE denote the diameter and the transition energy of the SWCNTs. The electric field orientation with respect to the nanotubes also determines the strength of the dipole moment. If the electric field is perpendicular $\overrightarrow{E_{\perp}}$ to the nanotube axis, surface-bound charges lead to a local depolarization field thus opposing the applied electric field $\vec{E}_{tot}$. When the electric field $\overrightarrow{E_{\parallel}}$ is parallel to the nanotube axis, charges accumulate at the end of the nanotubes at a given $\vec{E}$. However, the resultant field is high for a nanotube with significantly larger length/diameter ratio. Hence, the local electric field experienced by the nanotube is a net electric field.

$$\vec{E}_{loc} = \vec{E}_{tot} - \vec{E} \tag{2.16}$$

Theoretical studies show that the dipole moments are primarily induced along the nanotube axis as $\alpha_{\perp}$compared to $\alpha_{\parallel}$.[123,124] This is due to the electronic wavefunction of the delocalized electrons which is more concentrated along the nanotube axis, indicating that the polarizability of the nanotube is completely dependent on the electronic structure of the nanotube.[125] (metallic tubes are more polarizable compared to the semiconducting ones)

2.6.2 Dielectrophoretic Force

DEP force F_{DEP} of the particle arises from the interaction of the dipole with the non - homogeneous electric field and can be expressed as:

$$\vec{F}_{DEP} = (\vec{p} \cdot \nabla)\vec{E} \tag{2.17}$$

$$\vec{p} = v\tilde{\alpha}\vec{E} \tag{2.18}$$

$$\tilde{\alpha}_n = \varepsilon_m \tilde{f}_{CM,n} \tag{2.19}$$

$$\vec{F}_{DEP} = \frac{\pi d_{CNT}^2 l_{CNT}}{8} \varepsilon_m \, Re\left(\tilde{f}_{CM,n}\right) \nabla \vec{E}^2 \tag{2.20}$$

$$\tilde{f}_{CM,n} = \frac{\tilde{\varepsilon}_{CNT} - \tilde{\varepsilon}_m}{(\tilde{\varepsilon}_m + (\tilde{\varepsilon}_{CNT} - \tilde{\varepsilon}_m) L_n)} \tag{2.21}$$

$$\tilde{\varepsilon}_{CNT,m} = \tilde{\varepsilon}_{CNT,m} - i \frac{\sigma_{CNT,m}}{\omega} \tag{2.22}$$

where l_{CNT} is the nanotube length, $\tilde{\varepsilon}$ and σ are the dielectric constants and conductivity of the nanotube and medium (m) respectively. $\tilde{f}_{CM,n}$ is known as the Clausius - Mossotti factor which represents the frequency dependence of the effective polarizability of the nanotube solution.[145] It also determines the direction or the sign of the DEP force. L_n is the depolarization index. It is determined by the CNT device geometry and can be derived through an elliptical integral which is in the order of $10^{-5}$for $1\mu m$ long tubes.[140,121] DC DEP is mostly carried out for the nanotubes dispersed in organic sovents with low polarity or low ionic concentrations such as toluene. CNT deposition with DC DEP can be increased by increasing the magnitude of DC electric field, but after a certain threshold the electrolysis of the electrodes starts leading to the removal of the fabricated contacts.[126]

2.7 Carbon Nanotube Transistors

As discussed above, in order to probe the electrical properties of the s-SWCNTs, they have been integrated to a three terminal transistor geometry.[21,127,128] The transistor channel is the CNT, connected with two metallic electrodes, namely the source and drain at the ends. Depending on the device architecture, the gate electrode is placed with a dielectric spacer. As majority of the CNT transistors are built on silicon platform, the substrate is the doped silicon with thermally grown oxide on the top acting as the spacer between the substrate as the gate electrode from the nanotube. The design resembles to the metal- oxide semiconductor field effect transistor (MOSFET). The switching behavior of the transistor is generally dominated by the contact, the device acts as a Schottky barrier (SB) transistor rather than a charge carrier channel dependent transistor. As mentioned in the above section, the conductance of SWCNTs are governed by Landauer's formula.

As stated, if the length of the nanotube is negligible in comparison to the mean free path of the electrons, the nanotubes can exhibit ballistic transport behavior. However, the experimental reports state a conductive behavior due to the intrinsic and contact resistances. Consequently, the total resistance across the channel from source to drain is as follows[129]

$$R = \frac{h}{2e^2 M} \frac{L_{ch}}{L_{MFP}} + R_q + \frac{2\rho_c}{L_c \, d_t} \tag{2.23}$$

Where h is the Planck's constant, M is the number of modes in the channel ($M = 2$ for a nanotube), L_{ch} is the channel length, L_{MFP} is the mean free path for phonon scattering, R_q is the quantum resistance limit ($\sim 6.5\ k\Omega$), ρ_c is the contact resistivity, L_c is the contact length and d_t is the nanotube diameter. The contact resistance ($R_q + \frac{\rho_c}{L_c \, d_t}$) is of particular importance as it comprises of resistances from the Schottky

barrier as well as any other resistances emerging at the metal - CNT interfaces. It governs the electrical transport across the device and also imposes limits on scaling and device densities.[130]

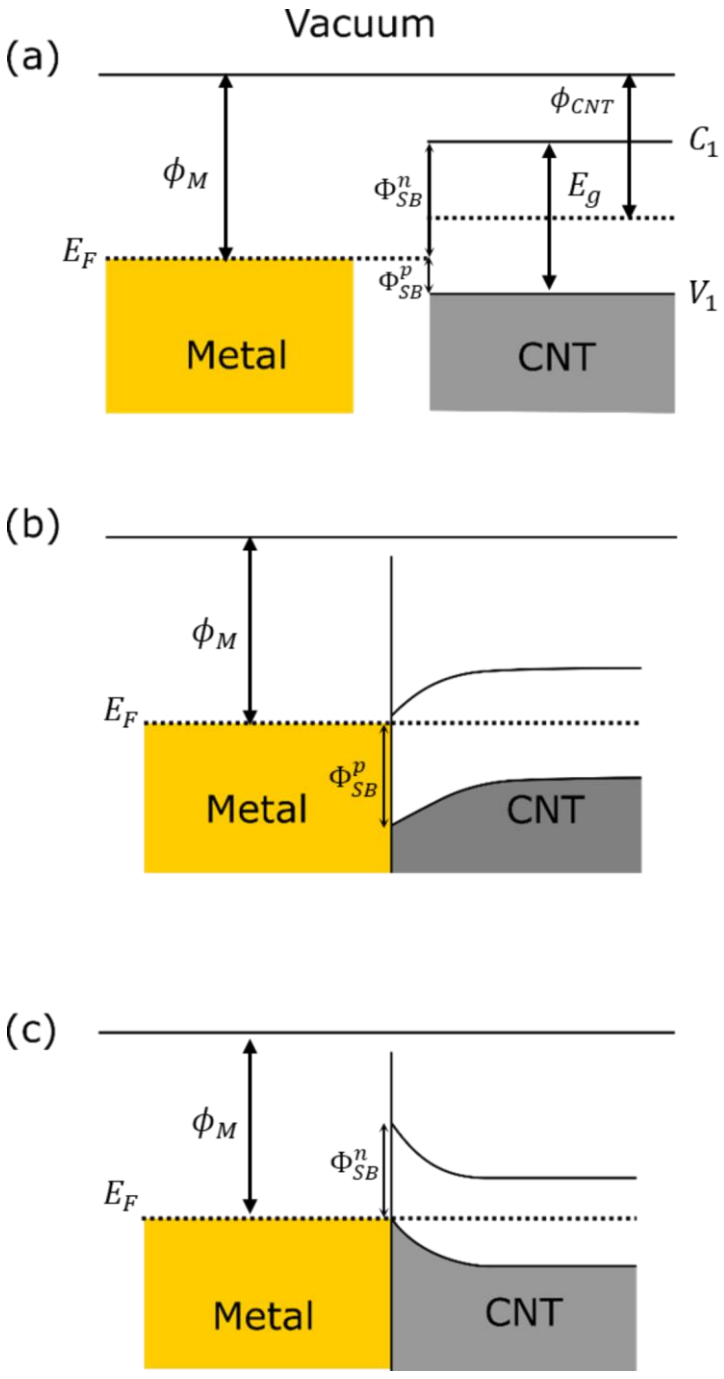

Figure 2.10: Schematics of the Fermi level of the metal, the (E_g) band gap of the nanotubes and the Schottky barrier height for electrons and holes (b) Band alignment for p type contacts and (c) n- type contacts.

The barriers that contribute to the electrical behavior are Ohmic and Schottky barriers that are formed at the metal nanotube interface. The Ohmic contacts are mainly caused from the metallic and contact resistance. A Schottky barrier is formed when the Fermi level of the metal lies in between the valence and conduction band of the s-SWCNT. One such interface also gives rise to surface states and wavefunction decaying exponentially into the tube.[131] The Schottky barrier height for holes and electrons can be determined with the following expressions

$$\Phi_{SB}^{p} = \phi_{CNT} + \frac{E_g}{2} - \phi_M \tag{2.24}$$

$$\Phi_{SB}^{n} = \phi_M - \phi_{CNT} + \frac{E_g}{2} \tag{2.25}$$

Here ϕ_M represents the work function of the metal, ϕ_{CNT} is the work function of the nanotube and E_g is the energy gap as represented in Figure 2.10, a visual representation of equation 2.24 and 2.25. On the contrary, when there is an alignment with the hole band, the barrier for hole injection is reduced but in contrast, it increases for the electrons. It can be seen from Figure 2.10 (b) and (c) as well as Equation 2.24 and Equation 2.25 that the Schottky barrier height for holes or electrons for a particular CNT will depend upon the work function of the metal contacts.[132]

There is a critical nanotube diameter dependence below which a Schottky barrier height increases with decreasing diameter for every metal.[132] Due to high work function of the metal and absence of hybridization between carbon and Pd atom, Palladium makes a Ohmic p-type contact with the large diameter s-SWCNTs.[133] The consistency in the contact property motivates the use of Pd electrodes to provide a metallic contact to the nanotubes in our work.

2.8 Photocurrent Generation Mechanism in Single Walled Carbon Nanotubes

The photocurrent generation mechanism in CNTs can be broken down into phonon assisted and electric field assisted. The phonon assisted or thermal based photocurrent generation is independent of exciton generation or relaxation process and can be further classified into bolometric as well as photothermoelectric effect (PTE). The bolometric effect dominates when a DC bias is applied across the nanotube channel and can efficiently dissociate the charge carriers across the entire nanotube channel.[60–62] The photoresponse (change in resistance) is dependent on the change in temperature due to the incident radiation. Bolometric effect can be differentiated from photovoltaic effect by electrostatic doping.[62]

In absence of a DC bias, the CNT devices generate either a PTE or a photovoltaic (PV) /electric field assisted photocurrent. Both mechanisms exist together and their relative strength depends on the nanotube type and electronic assembly of the CNT film along with the device geometry.[63–65] PTE works on the Seebeck effect, where the temperature difference is induced by absorption of light by two materials, generating a potential gradient due to the difference in the Seebeck coefficients between the metal electrodes and the nanotubes.

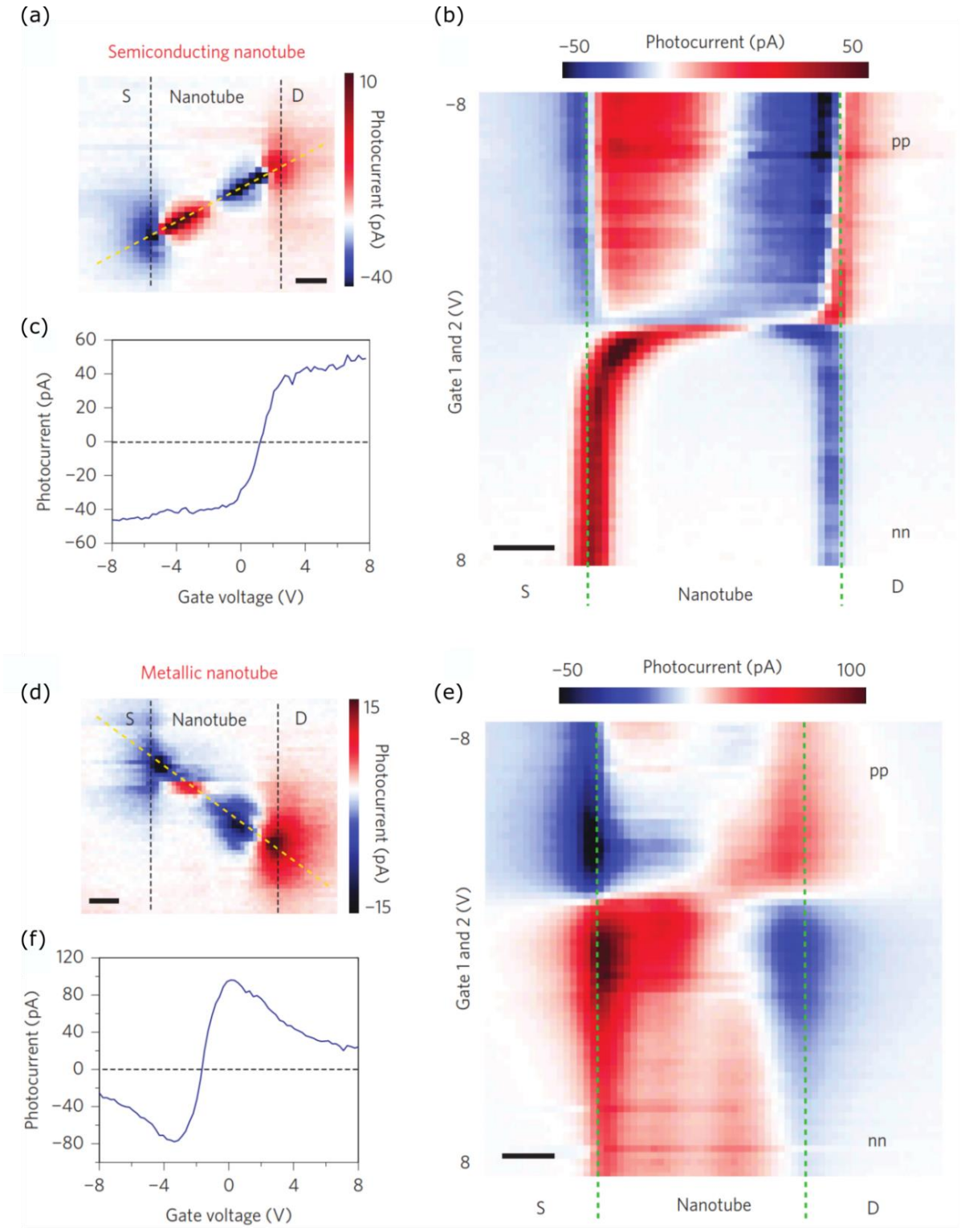

Figure 2.11: Photocurrent map of p - doped (a) semiconducting nanotube and (d) metallic nanotubes at different gate biases ($V_{G1} = V_{G2}$). The laser is scanned along the left green dashed line on (b) and (e) to generate a photocurrent profile across the (c) semiconducting and (f) metallic nanotube channel as well. This is repeated at different gate voltages to observe typical (b) semiconducting and (e) metallic variations in the photocurrent. (Reproduced from[134])

The generated photo voltage due to illumination can be expressed as

$$\Delta V = \Delta T \times (S_{CNT} - S_{electrode}) \quad (2.26)$$

where ΔV, ΔT, S_{CNT} and $S_{electrode}$ is the generated photo voltage, the temperature gradient between the metal electrode / CNT interface along with the Seebeck coefficient of the nanotube and metal electrode respectively. The magnitude of the photo voltage generated depends on the intensity of the incident radiation and the device architecture or the geometry.[65,135] In addition, the presence of heat sinks or quench sites suppresses phonon accumulation and reduces the photocurrent generated in turn.[136,137] The thermally generated photocurrent is more prominent in the suspended CNT devices, compared to the devices with CNT channels in contact with the substrate. The substrate acts as a heat sink suppressing the phonon population across the nanotube channel.

Whereas, the PV works on the electric field gradient generated along the nanotube film or at the contacts. Along the nanotube channel, the electric field gradient is generated by an electrostatic gating (split gate) and at the edge of the nanotube- metal contact, electric field gradient is generated due to the formation of Schottky barrier due to the difference in work-function between the nanotube film and the metal contact. But the Schottky barrier based photocurrent generation is more prominent in smaller diameter tubes, due to a larger difference in the fermi levels between the nanotubes and the metal contact. To realise photocurrent through electrostatic doping, a larger diameter tube or a different metal contact with lower work function should be considered, minimizing work-function difference between the nanotube and metal contact.

It is difficult to differentiate whether the photocurrent is due to the PTE or PV. However, these mechanisms can be distinguished from one another by electrostatic doping.[134,138] It is evident that the CNT transistor can exhibit two different signatures on homogenous doping of the channel. The photocurrent from the difference in Seebeck coefficient of metallic nanotube and the metal electrode is observed when the laser is positioned at the nanotube electrode interface (Figure 2.11 (e)). The line profile (Figure 2.11 (f)) along the left green line of Figure 2.11 (e) shows a non – monotonic dependence on gate voltage, a characteristic of the Seebeck effect. On contrary with semiconducting nanotubes, homogeneous doping shows photocurrent shifting towards the center of the nanotube with decreasing electrostatic doping (Figure 2.11 (b)). This arises from the shift in maximum electric field at the Schottky barriers towards the centre of the nanotube, resulting from the extension of the depletion region with decreasing doping concentration. A line profile of the photocurrent is presented in Figure 2.11 (c) taken along the left green line in Figure 2.11 (b), the continuous increase in photocurrent with increasing gate voltage on both positive and negative direction is an effect of electric field at the Schottky barrier changing sign (a signature of photovoltaic effect).

On measuring the photocurrent profile as function of position along the nanotube axis, the photocurrent from the semiconducting and metallic nanotubes across the p-n junction are shown in blue and red in figure 2.12, respectively. The photocurrent from the semiconducting tube shows a Gaussian profile. The data was fitted with Gaussian, divided by a factor four for clarity (Blue line). The tails come from the non-perfect laser spot due to diffraction limit. On contrast, the photocurrent from metallic nanotube extends up to 2µm on each side of the p-n junction. The broad triangular shape is due to the photo-generated hot carriers and follow a thermal distribution through the nanotube. At nanotube electrode interface, the sign change in photoresponse for metallic nanotube is due to difference in Seebeck coefficient between the

nanotube and electrode or band bending at the contacts. This difference in photocurrent response confirms that photocurrent in semiconducting nanotubes results from an electric field (Photovoltaic effect) and in metallic nanotube is due to the photothermal effect.[134]

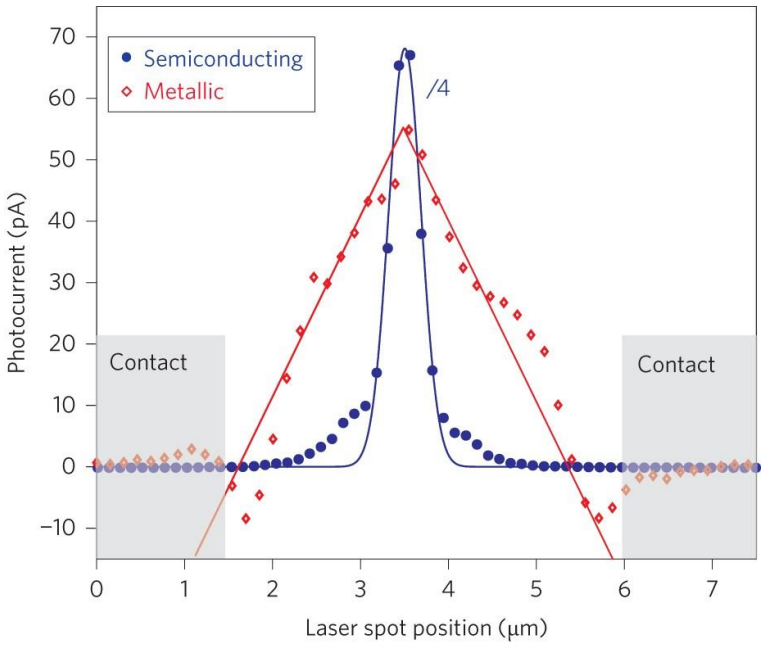

Figure 2.12: Photocurrent response plotted as a function of laser spot position for semiconducting (blue) and metallic (red) carbon nanotube p-n junctions. The photocurrent from the semiconducting nanotube is fitted with a Gaussian and divided by a factor four for clarity. The Gaussian profile originates from the laser spot profile and the electric field at the junction. The photocurrent response from the metallic nanotube shows a triangular profile, indicating hot carrier transport. Both measurements were recorded at 532 nm laser. (reproduced from [134])

3 Materials and Nanotube Dispersions: Preparation and Length Analysis

3.1 Carbon Nanotube Synthesis Methods

Carbon nanotubes can be synthesized under various conditions. With the appropriate parameters, they are synthesized using several techniques like chemical vapor deposition (CVD), arc discharge (AD), high pressure carbon monoxide carbon disproportionation (HiPCO), laser ablation (LA) etc. All the methods are majorly tailored with the requirement of the final product to be synthesized.

3.1.1 Chemical Vapor Deposition (CVD)

The technique involves chemical deposition under appropriate temperature and pressure. CVD is the most versatile technique for synthesizing large quantity of CNTs. The technique enables various forms of CNT growth right from thin films to entangled strands. The general architecture for the technique consists of a pressure controlled chamber containing a catalyst precursor over which a nucleation takes place. Catalysts can be placed with the requirement on from a surface of a substrate to pre patterned device geometry.

CNTs are grown at a desired temperature window for a specific mixture of the hydrocarbon gases such as ethylene, carbon monoxide etc. and the carrier gas such as hydrogen, nitrogen etc. is reacted over the catalyst for a calculated time of 15min to 90 min based on the desired output. SWCNTs are favored to grow at higher temperatures (typically 900°C - 2500°C) over MWCNTs[139] as shown in Figure 3.1. At such temperatures pyrolysis of the hydrocarbons results in amorphous carbon formation. Gases with high thermal stability such as carbon monoxide (CO)[140] and methane (CH_4)[141] are thereof widely used as carbon source. For further enhancement, Franklin et al. also added hydrogen (H_2) gas to the mixture in order to breakdown the excess carbon and increase the nanotube yield. Other hydrocarbons such as hexane[142] and benzene[143] along with H_2 have also been used for synthesis. Apart from temperature, the preference of SWCNTs over other types can also be facilitated by adjusting the feedstock, catalyst composition and size.

Hence, transition metals such as Fe is an important catalyst to its catalytic activity for the decomposition and formation of metastable carbides and because carbon is able to rapidly diffuse through and over its surface. From a scalable standpoint, CoMoCAT and HiPCO are two processes that are currently used for producing SWCNTs in bulk and are commercially available. The CoMoCAT process involves the disproportionation of CO at 700 °C - 950 °C in flow of pure CO at a total pressure that typically ranges from 1 to 10 atm.[144] The key ingredient in the process is the presence of the Co - Mo catalyst hence the name CoMoCAT. Separately, they are either inactive (Mo alone) or unselective (Co alone), however, a combination of the two can generate a significant amount SWCNTs (0.25 g SWNT/g catalyst). Although, the diameter distribution of the synthesized nanotube bundle broadens with an increase in temperature, it is still lower compared to the SWCNTs synthesized using HiPCO process.[145]

The HiPCO method involves decomposing an iron-based catalyst $Fe(CO)_5$ by allowing CO to flow over its surface at high temperature (900°C - 1100°C) and pressure (30atm - 50atm). A production rate of 10.8g/day is achieved by flowing a mixture of 1.4L/min of $Fe(CO)_5$ and 8.4L/min CO vapours, into a chamber at 1050°C temperature and 30atm pressure.[146] The field has further evolved over the years towards monochiral growth for few (n, m) species.[147]

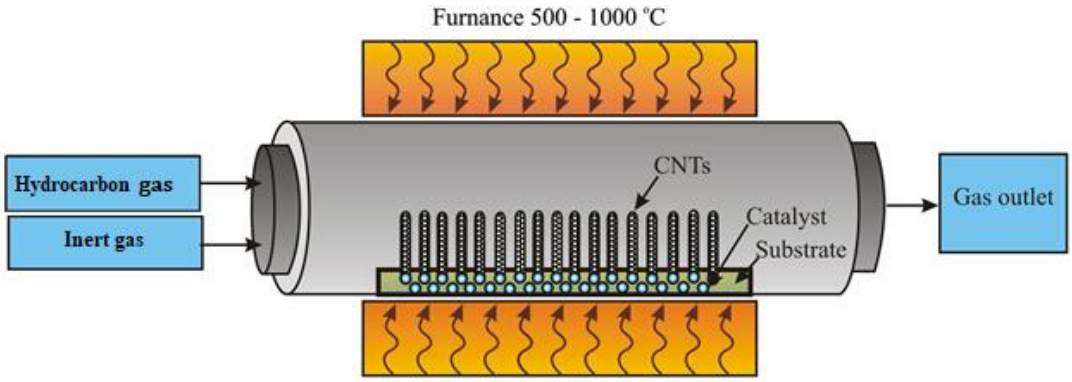

Figure 3.1: Schematic of Chemical vapour deposition (CVD) setup

3.1.2 Pulsed Laser Vaporization

Laser vaporization is a similar technique compared to the CVD technique, where the carbon source is now a solid feed stock instead of a gaseous source. Also, the feed stock is now heated with a pulsed laser inside the furnace. Variables such as laser wavelength, energy and duty cycle, temperature, gas type, flow rate and pressure, target morphology and position, and reactor geometry can be adjusted, and each have been shown to influence the production of SWCNTs. But the influence on the (n, m)-distribution is not considerably large. The diameter distribution can be influenced a little by changing gas pressure or oven temperature. Detailed reviews can be found in the literature [148,149]

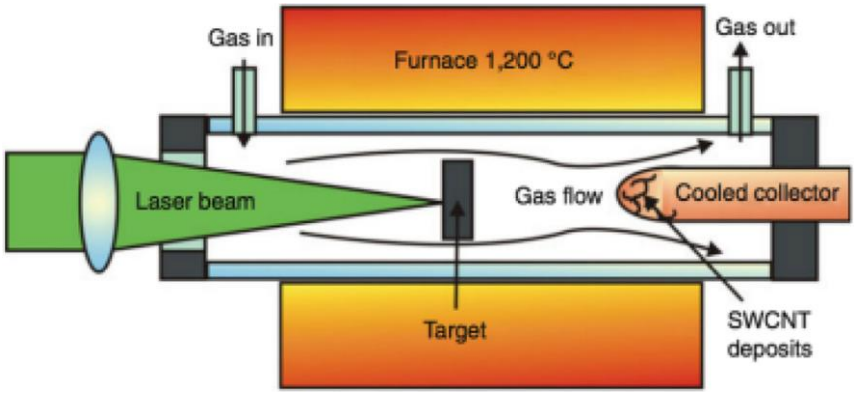

Figure 3.2: Schematics of Pulsed Laser vaporization setup

Uniform strands of SWCNTs of diameter ranging from 1 nm to 20nm were synthesized by heating 1.2% cobalt/nickel with 98.8% graphite and a Nd : YAG laser inside a furnace at 1200°C. The atmosphere was inert argon and helium and the pressure was kept constant at 500mTorr. This method is capable of producing SWCNTs at a large scale (1g/day), a purity of 70% -90% was reported using this method.[31] The first

use of a sub - picosecond pulsed laser (74.8MHz repetition rate, 400fs pulse width, and 350W average power) for the production of high quality SWCNTs was reported by Eklund et al.[150] yields up to 1.5g/hr were possible with such a system, which could be further improved to 45g/hr.

3.2 Dispersions of Single Walled Carbon Nanotubes

While CNTs are dispersed in different forms, the liquid dispersed SWCNTs are easier to handle compared to their solid counterparts where transferring, sorting and purifying is difficult. The liquid dispersed SWCNTs are promising candidates for integrating in complex device geometry and for studying the optical and electrical properties of the nanotubes. In order to obtain a liquid based suspension, either in water or in organic solvent, the tubes have to undergo a proper functionalization either covalently or non- covalently. Non-covalent functionalization is often used for water based dispersions and results in a surfactant based functionalization leaving the tube physically unaffected, however, covalent functionalization does exist to create water based suspensions. Similarly, both covalent and non-covalent functionalization exists for organic solvents, resulting in introducing functional groups on the tube ends and the sidewalls, enabling them to be dispersed in a specific organic solvent. While all this methods helps in sorting individual tubes with respect to the diameter and the electronic types, it also lowers the SWCNT's performance due to the disruption of the π bond conjugation by sp^3 hybridization.

3.2.1 Surfactant coating

Surfactant coating comes under the class of non-covalent approaches as explained above leading to an aqueous suspension of SWCNT. On adding the surfactant to the water, the surfactant molecules just form a random layer around the nanotubes up to a certain concentration called the critical micellar concentration. Above the critical micellar concentration, the surfactant molecules wrap the entire nanotube with a uniform coating forming a hemi micelle or a complete micelle based on the structure or the diameter of the nanotube. This also depends on the surfactant itself. SDS forms different micelles than Sodium Cholate. The correlation between the nanotube to the surfactant wrapping efficiency is dependent on the differences in the surface π electron states due to the SWCNT curvatures determining the interaction between the nanotubes and the surfactant molecules.[151] In order for Sodium dodecyl sulphide (SDS) molecule to surround a smaller diameter tube, it requires a large energy due to large curvature bond on smaller diameter tubes. Thus, the SDS molecule prefers coating a larger diameter tube with smaller curvature.[42,152] Besides the curvature, the SDS wrapping also depends on the electronic characteristics of the SWCNTs and SDS favors wrapping a m-SWCNT rather than a s-SWCNT due to the higher polarizability of the former one.[42,153]

The type and concentration of the surfactant determines the hydration layer and consequently determines the buoyant density which makes them critically important. For instance, sodium cholate surfactant can be used to separate semiconducting nanotubes according to the bandgap and diameter.[154] Adding NaCl to the surfactant allows the isolation of CNTs with average diameter ~1.4nm at purity levels close to 99%.[155] On the other hand, using DOC separates the mixture according to length.[156] In general, bile salts (sodium cholate, sodium deoxy-cholate, sodium taurodeocycholate) were found to be much more effective in suspending CNTs than the linear surfactants (sodium dodecylsulfate, sodium dodecylbenzenesulfonate).[157]

3.2.2 Polymer Wrapping

Dispersing SWCNTs by wrapping them with aromatic polymers produces stable SWCNT suspensions in organic solvents. The polymer wrapped SWCNT suspensions are gaining more attention over the years as it demonstrates the sorting selectivity greater than 99% for s-SWCNTs. In this process, the SWCNT raw materials are dispersed in organic solvents at first using ultra sonication in presence of the suitable polymer for the desired product, namely semiconducting, monochiral etc., followed by ultracentrifugation. Ultimately, just the CNTs which possess preferential interaction with polymer can suspend in the solvent.

Different polymers like poly (9,9-dioctylfluorenyl- 2,7-diyl) commonly PFO, poly (9,9-dioctylfluorenyl- 2,7-diyl)-co-(9, 10- anthracene) commonly PFH-A etc. have been used for isolating s-SWCNTs. The mechanism is commonly attributed to the π-π aromatic stacking between the SWCNT and the aromatic backbone of the polymer, thereby suspending the nanotube in the solvent. There are several factors to be determined for a polymer sorted suspension, however, beyond a certain concentration of the polymer bundling of metallic CNTs is observed in the dispersion.[158]

Small changes in the structure can yield highly (n, m) selective dispersions. For instance, dispersing poly (9,9-dioctylfluorenyl- 2,7-diyl) (PFO) with CoMoCAT material can yield suspensions high in (7, 5) SWCNTs. On the other hand, (6, 5) SWCNTs can be extracted from the same starting material when wrapped with poly[(9,9 - dioctylfluorenyl - 2,7 - diyl) - alt - co -(6,60 - {2,20 - bipyridine})] (PFO - BPy). Different parameters such as the type of solvent, temperature and molecular weight play a role in the selectivity process. For instance, replacing toluene with other solvents such as tetrahydrofuran (THF) or chloroform reduces the selectivity of polymers such as PFO to nanotubes. Wang et al. attributed this to the bundling of the nanotubes remaining in the solution after centrifugation because of the buoyant forces.[159] Hennrich et al. reported that dispersing PFO with CoMoCAT material produces monochiral (7, 5) suspensions.[160] Understanding the mechanism behind polymer wrapping remains a challenge. Theoretical studies have been carried out in order to understand nanotube - polymer interactions. Molecular dynamics (MD) simulations have been used to investigate the surface coverage as well as the conformation of polymers on different diameters and (n, m) species of CNTs.

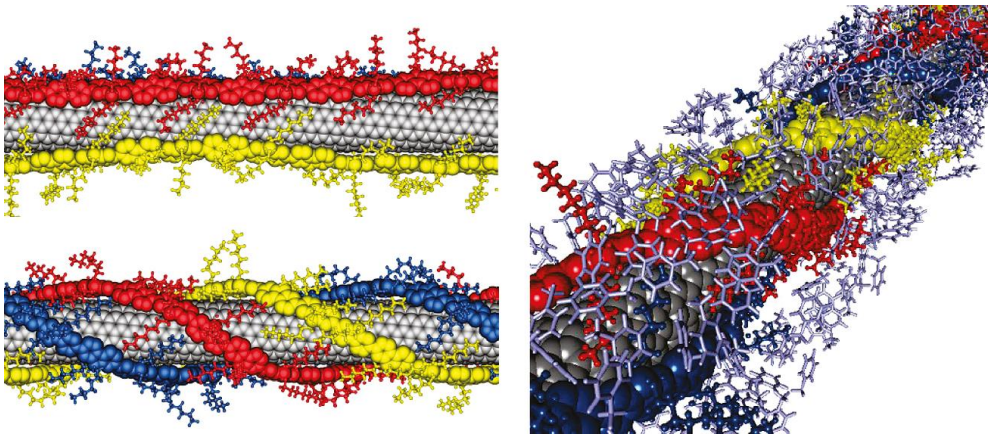

Figure 3.3: MD simulations of polymer wrapping of PFO reproduced from Gao ACS Nano 2011. [161]

3.3 Size Exclusion Chromatography

Size exclusion chromatography (SEC) or gel permeation chromatography (GPC) is the process of separating the CNTs according to their lengths. This technique is used to yield unmodified and impurity free CNT dispersion by passing the nanotubes through the column packed with porous gel.[151,162] Fractions of different length distributions are obtained by adjusting the pore size. The raw CNT material is initially wrapped with sodium dodecyl sulphate (SDS) and 1wt% SDS is used as the eluent. Typically, with the right combination of eluent and packing material or stationary phase, it is possible to sort CNT dispersions according to length and electronic type.[162] For instance, the use of agarose gel for packing material and sodium deoxycholate (DOC) as the eluent, it is possible to perform metallic/semiconducting separation.[163] This is due to the weak interaction of the metallic nanotubes with the gel resulting in rapid migration through the column. Alternatively, sephacryl gel has been reported to be more selective. Studies have shown that semiconducting nanotubes are more interactive and in order to elute them, SDS of increasing concentration can be employed.[164]

Hennrich et.al used the same technique for the first time for organic solvent based polymer wrapped tube to separate them with respect to their length. The technique also improves the purity of s-SWCNT and reduces the excess polymer wrapping content.[160] The CNT raw material was wrapped with poly(9, 9-di-n-dodecylflurenyl-2, 7-diyl) (PODOF) as mentioned in the section above and toluene was used as eluent. The SEC fractionation column was made by using Toyopearl HW 75, and was used for all the materials in this work. Figure 3.4 shows the chromatogram of the PODOF wrapped starting suspension. The chromatogram can roughly be divided into two regions: (i) elution time between ∼20−35 min during which only the polymer-wrapped SWCNTs elute, and (ii) elution time between ∼35−45 min during which both polymer-wrapped tubes and “free” polymer elutes. Fractions of 5−10mL were sequentially collected from the first broad band eluting from the column and were then analyzed by measuring UV−vis−NIR absorption spectroscopy. These spectra show mainly the first (S11), second (S22) and third (S33) inter-band transitions of s-SWCNTs.

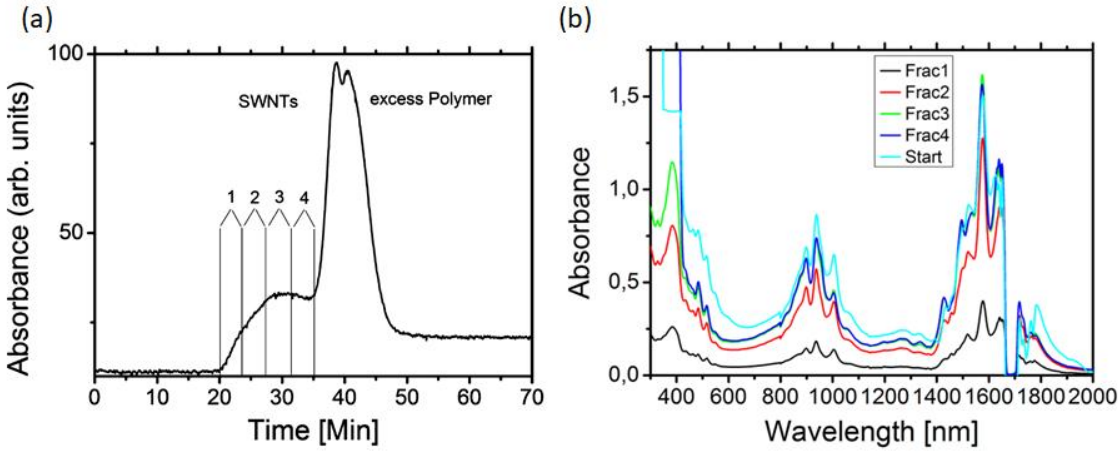

Figure 3.4: (a) Chromatogram of PODOF wrapped PLV SWCNTs. Grey lines indicate fractions collected for analysis. (b) Absorption spectra of SEC fractions of PODOF wrapped PLV SWCNTs in toluene, fractions refer those indicated in (a). Start indicates the starting suspension (diluted 5X for a better comparison) reproduced from [Hennrich et.al ACS nano 2016][160]

3.4 Length analysis of monochiral SWCNTs in toluene with Analytical Ultracentrifugation

The length of a CNT is an important dimension that has to be adjusted to the requirements of an experiment or application, e.g., through sorting methods. Hence, the length analysis of the sorted and dispersed CNTs becomes of crucial importance. Techniques like scanning electron microscopy (SEM) and atomic force microscopy (AFM) are widely used as a comparison to gauge the nanotube length. In particular, the AFM method has evolved over the years as the standard method to measure the nanotube length distributions,[165] despite requiring specific substrates and tedious preparation techniques along with associated uncertainties like bundling on surfaces or selective adsorption and time consuming data collection.[166,167] On the other hand, there is a range of in situ methods that have been explored, such as dynamic light scattering,[168–171] electrospray differential mobility analysis,[172] shear-aligned photoluminescence anisotropy[173] and length analysis by nanotube diffusion analysis method,[174] and more recently analytical ultracentrifugation (AUC)[175] and electric-field induced differential absorption (EFIDAS).[176] Most of these methods have been applied to aqueous SWCNT dispersions, whereas ultrapure semiconducting SWCNTs (>99% purity) can nowadays be obtained through wrapping of SWCNTs with polymers in toluene.[160] These non-aqueous dispersions are of great advantage to integrate nanotubes into device applications,[160,177] and methods to measure in situ length distribution of SWCNTs in toluene are required. Recently, EFIDAS was introduced as a method giving access to the average length of SWCNTs in non-aqueous dispersions.[176] In this part of the thesis, we explore a method for length analysis using AUC for non-aqueous dispersions for the first time, specifically of polyfluorene (PFO)-wrapped (7, 5) SWCNTs in toluene along with the AFM technique to gauge the AUC derived length distributions.

3.4.1 Atomic Force Microscopy

Atomic force microscopy is widely used to determine the length distribution in a nanotube dispersion. AFM is a scanning probe microscopy technique and has a resolution in the order of few tens of Angstroms, enabling it to a wide use to characterize the geometry of materials and molecules- typically the diameter and length in case of the CNTs.

3.4.1.1 Sample Preparation

In order to determine the average length distribution of the sorted nanotubes, samples were prepared by dropping 0.5µL of SWCNT solution onto a ~1cm^2 silicon wafer and spin coating at 3500rpm for 60sec. The silicon wafers were first surface treated by oxygen plasma treatment for 2 mins using a table top low pressure plasma cleaner ATTO® from Diener Electronic. Following the plasma treatment, the wafers were treated with carbon-di-oxide snow jet using a homemade heated vacuum chuck.

3.4.1.2 Atomic Force Microscope Measurement

The AFM measurements were performed in atmospheric environment with a multimode head and Nanoscope III controller (Digital Instruments), operated in tapping mode.[178] Commercially available silicon cantilevers with fundamental resonance frequency of 320kHz were used. 10 x 10µm^2 (see Figure 3.5 (a)) or 5 x 5µm^2 topographic and amplitude images were collected simultaneously at a scan rate of 1Hz with the parameters set point, amplitude and feedback control optimized for each sample.

3.4.1.3 Statistical Length Analysis of AFM Micrograph with SIMAGIS

The collected AFM micrographs were analyzed using a SIMAGIS image analysis software. The software detects the topographic gradients and plots the existence of the nanotube on a given field of the obtained micrograph. The SIMAGIS marked plots were then manually corrected to remove the errors caused by bundles and agglomeration due to the excess polymers etc. generating the final statistics for the length distribution. The generated statistics is then plotted as a histogram (see Figure 3.5 (b)) where typically 200-300 nanotubes are analyzed per fraction for the basis of length distribution and fitted with a Gaussian curve to obtain a distribution from each fraction of a single synthesized batch. Figure 3.5 (c) shows the peak value of the length distribution from each fraction and Figure 3.5 (d) shows the height versus length correlation of the analyzed tubes from the AFM micrograph proving that there are no bundles of more than three tubes in the dispersion or on the surface. All the data represented below are from the monochiral CoMoCAT PODOF wrapped (7, 5) samples as shown in Chapter 2 section 2.4.3.

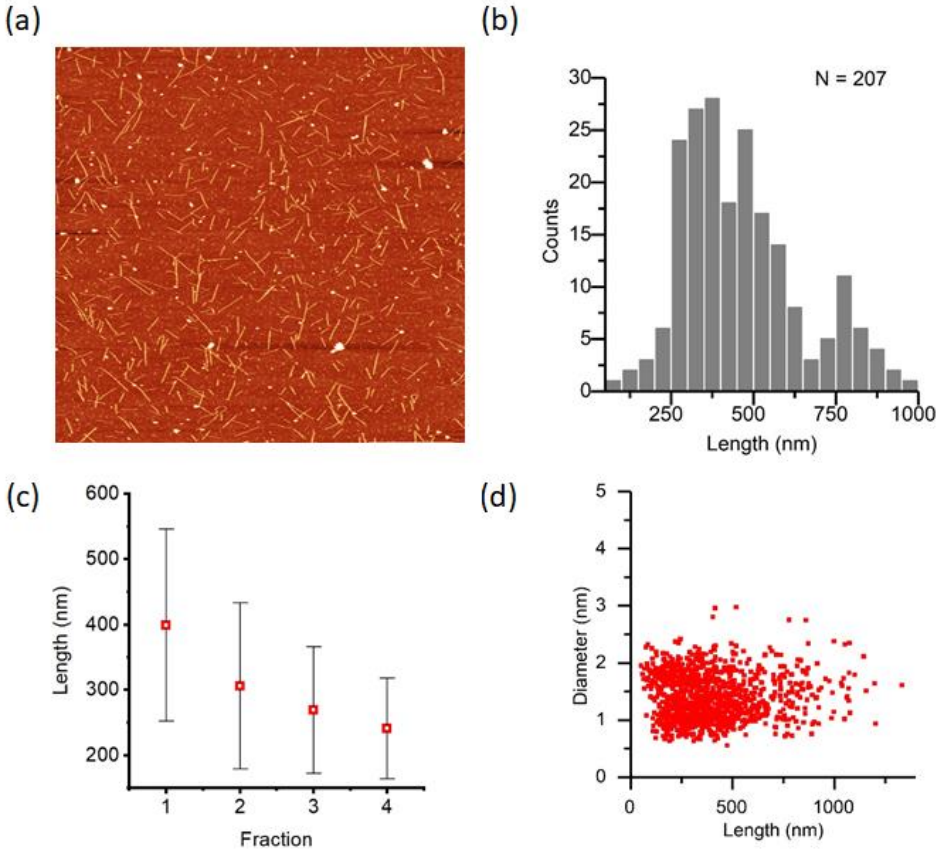

Figure 3.5: (a) AFM micrograph and its corresponding (the scale bar equals 2µ) (b) Length distribution histogram. The data presented here are obtained for a monochiral (7, 5) suspension [Reproduced from179] (c) shows the length correlation with fraction number and (d) shows the length versus height correlation from (a).

3.4.2 Analytical Ultracentrifuge (AUC)

Analytical ultracentrifugation (AUC) is a versatile and powerful method for the quantitative analysis of macromolecules in solution. AUC has broad applications for the study of bio macromolecules in a wide

range of solvents and solute concentrations. Size distributions of materials can be extracted from sedimentation velocity distributions, provided appropriate models for the friction coefficient are available. The fundamental requirements for the sample to be analyzed are that (i) it has an optical property that distinguishes it from the other solution components, (ii) it sediments or floats at a reasonable rate at an experimentally achievable gravitational field, and (iii) it is chemically compatible with the sample cell. The fundamental solvent requirements are its chemical compatibility with the sample cell and its compatibility with the optical systems.

3.4.2.1 Working principle

AUC combines an ultracentrifuge with the optical monitoring systems. In AUC, a sample's sedimentation profile is monitored in real time by an optical detection system. The sample is continuously monitored or detected using UV - visible light absorption and/or interference optical refractive index sensitive system. The system plots the evolution of sample concentration versus the axis of the rotation profile as a result of the applied centrifugal field. With modern instrumentation, these observations are electronically digitized and stored for further mathematical analysis.

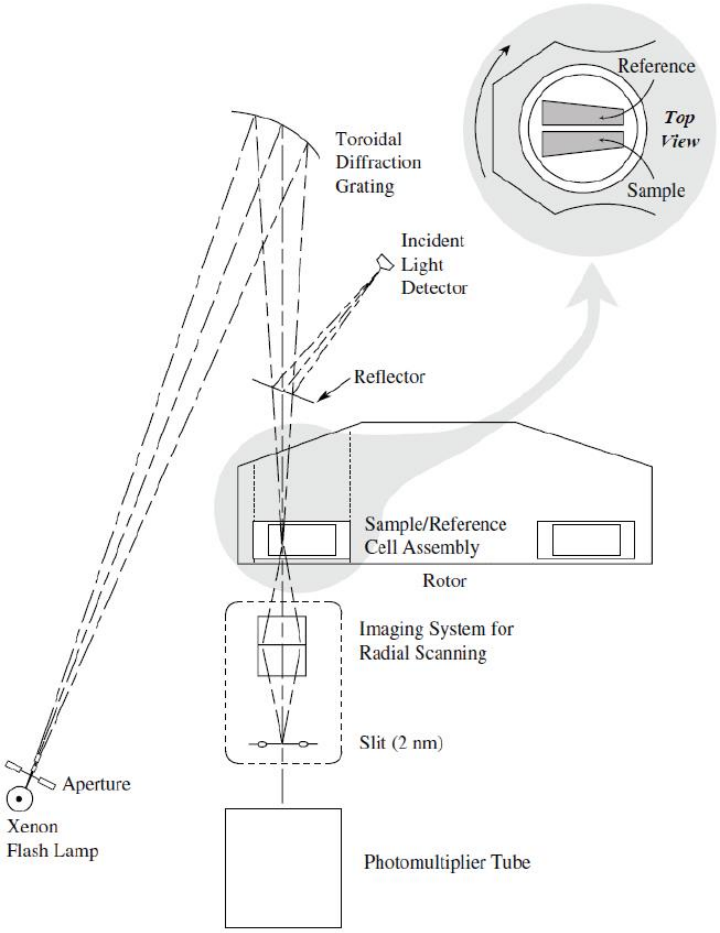

Figure 3.6 : Schematics of the Analytical Ultracentrifuge (AUC)

Figure 3.6 shows the schematics of the AUC technique. The rotor is capable to rotate at 50,000rpm. The 2nm slit underneath the rotor scans the sample and reference perpendicular to the rotational axis. Rest of the optical components are designated to execute absorbance UV-Vis measurements. The collected absorbance data across the cell is plotted as shown in Figure 3.7 (b) tagged with a time stamp. These absorbance curves are later processed to derive the sedimentation behavior of the suspended particles in terms of sedimentation coefficients (s).

3.4.2.2 Analytical Ultracentrifuge Data Analysis using SEDFIT

The obtained absorbance curves are then reproduced using numerical iteration technique with the Lamm's equation. Based on the mode of operation of the AUC, the Lamm's equation is modified and fitted to the absorbance data using a software package SEDFIT. SEDFIT solves Lamm's equation for the concentration profiles of each scan by numerical iteration of the sedimentation coefficients.[180] The software identifies s values, their relative weight and performs a regularization to obtain the distribution of sedimentation coefficients c(s), yielding the best fit to the time-dependent concentration profile. Also, SWCNTs in aqueous surfactant solutions or organic solvent solutions are characterized with AUC and length distributions are determined by modeling nanotubes as rigid rods.[175]

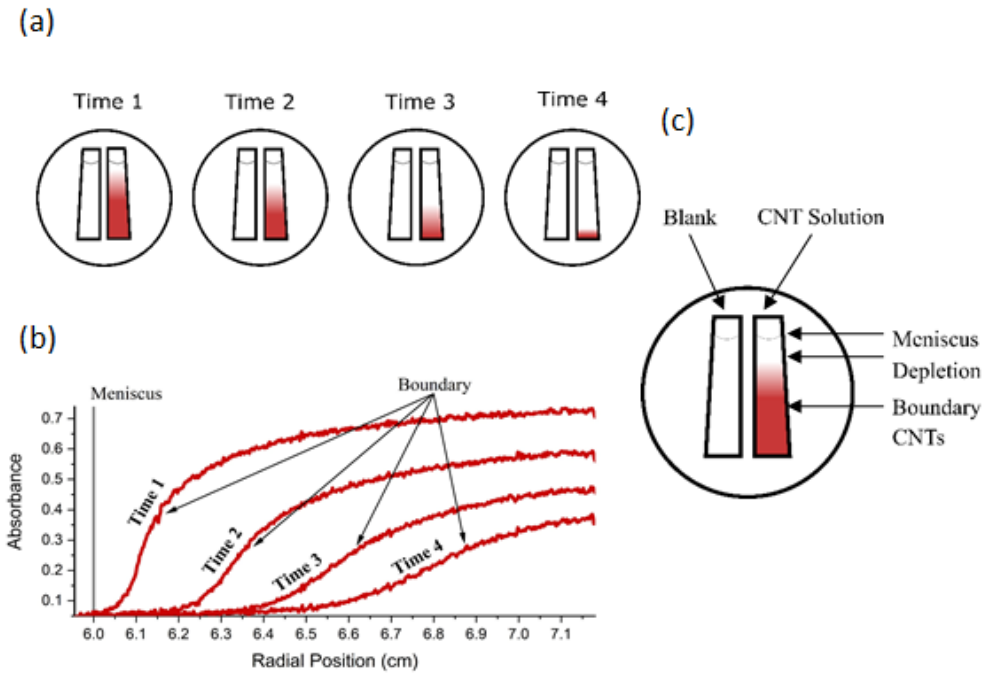

Figure 3.7: (a) shows the sector shaped cuvette filled with blank and sample for 4 different times showing the depletion of the particles in the sample due to the centrifugal force (b) shows the corresponding absorbance curves collected by the spectrometer (c) detailed layout of the centrifugation cell

3.4.2.3 Length Analysis of Toluene Dispersed (7, 5) SWCNTs using AUC

As mentioned above, AUC is widely used to measure the sedimentation velocity of materials such as biomolecules, polymers and nanoparticles.[181–186] Size distributions of materials can be extracted from sedimentation velocity distributions, provided appropriate models relating it to the friction coefficient are available. Here, a method to characterize and determine the length distribution of polymer wrapped toluene dispersed monochiral (7, 5) SWCNT is shown for the first time.

The two compartments of the AUC cell are filled with PFO-wrapped (7, 5) SWCNT dispersion, and the other with toluene as a reference, and centrifuged at 40000rpm- creating a centrifugal force of 116480g at the cell center. Inside the AUC, the concentration variation in space and time can be followed by absorbance, fluorescence, or interference optics, depending on the sample type and instrumentation. However, our AUC setup does not allow measuring fluorescence or absorbance in the nIR regime, nor does the interference optics provide sufficient sensitivity. Also, small but systematic, likely to be pressure induced shifts were observed in the S22 peak position during centrifugation, which in combination with the narrowness of the S22 peak gives erratic results when the S22 absorption of (7, 5) SWCNT is directly probed in the visible regime and S11 being as well out of the detection limit of the spectrometer of AUC. Hence the absorbance from the PFO was used to follow the sedimentation of the nanotubes, which is rather broad. The sedimentation was recorded every 10 min at an absorbance wavelength of 400nm along the radial position to follow the temporal and spatial evolution, hence leading to a series of absorbance scans.

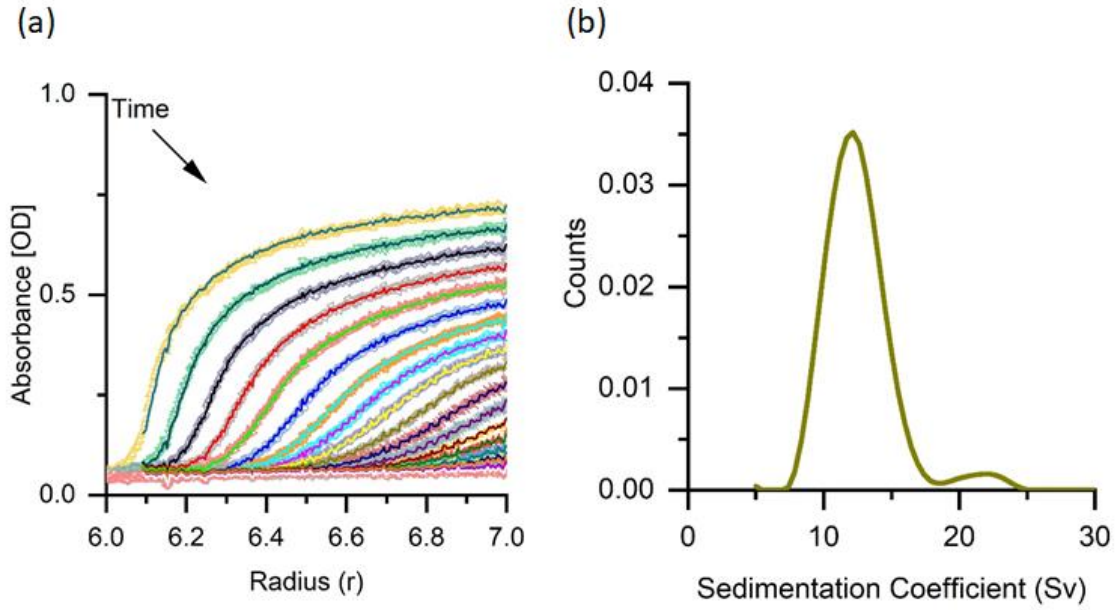

Figure 3.8 :. (a) Temporal and spatial evolution of the absorbance of PFO-wrapped (7, 5) SWCNTs during centrifugation in toluene. The radial position marks the distance from the AUC rotor centre along the centrifugal field. Absorbance scans were measured every 10min at 400nm wavelength. (b) Sedimentation coefficient distribution obtained from SEDFIT analysis based on the absorbance scans from (a).(All data are of same sample)[Reproduced from 179]

As absorbance is directly proportional to the concentration of the SWCNTs, Figure 3.8 (a) shows the temporal and spatial evolution of the concentration. As time progresses, nanotubes move along the centrifugal field and a depletion region appears on the top of the centrifugation cell, forming a boundary. The formed boundary gradually shifts to the larger radial positions. As the experiment proceeds with time, the boundary broadens due to the difference in the sedimentation or diffusion with different length of the nanotubes. In general, broadening will be dominated by the velocity distribution at longer times owing to its linear time dependence, whereas at short times, diffusive broadening with its square-root time dependence will be dominant.[187] This crossover shifts to a shorter time scales with increasing sedimentation velocity. The analysis of the data is greatly simplified when the diffusion is neglected, and it was evident that this is the case. Therefore, the data recorded within the first 50 min were discarded after reaching the targeted rotation speed. It has also been confirmed that PFO will not sediment under the present

conditions even after 6h at 40 000rpm, which otherwise could modify the results if residual free PFO would be present. The upper limit of absorbance decreases with time due to radial dilution caused by the sector shaped centrifuge cell. For such a cell, a partial differential equation called the Lamm's equation describes the transient transport of the species along the cell. On omitting the parts describing the diffusion, it leads to a simplified Lamm's equation as follows.

$$\frac{\partial n(r,t)}{\partial t} + \frac{1}{r}\frac{\partial}{\partial r}\left(s\omega^2 r^2 n(r,t)\right) = 0 \tag{3.1}$$

where n is the concentration at the radial position r, time t, ω is the angular velocity, and s is the sedimentation coefficient. Using Equation 3.1, the c(s) were determined from the absorbance/concentration scans across the centrifugation cell with the software package SEDFIT (ver.15.01b) using the Ls-g(s) model.[188] This model considers only ballistic motion and is appropriate when diffusion is negligible, as discussed above. SEDFIT solves Lamm's equation for the concentration profiles of each scan by numerical iteration of sedimentation coefficients.[189]

The software identifies s values along with their relative weight and performs a regularization to obtain the c(s), yielding the best fit to the time-dependent concentration profile. Figure 3.8(a) shows typically obtained excellent fits to the data, and the corresponding sedimentation coefficient distribution c(s) obtained via SEDFIT is shown in Figure 3.8(b). In Figure 3.8(b), a prominent peak of c(s) at 12 Sv can be assigned to the individual tubes, and the small or minor peak at 22 Sv of unknown origin can be related to nanotube agglomerates possibly dimers ($1\ \mathrm{Sv} = 10^{-13}\mathrm{s}$).To extract the length distribution c(L), which is encoded in the AUC-derived c(s) distribution, an appropriate model is required that correlates the sedimentation coefficient s with the length L of the PFO-wrapped (7, 5) SWCNTs (See Figure 3.9).

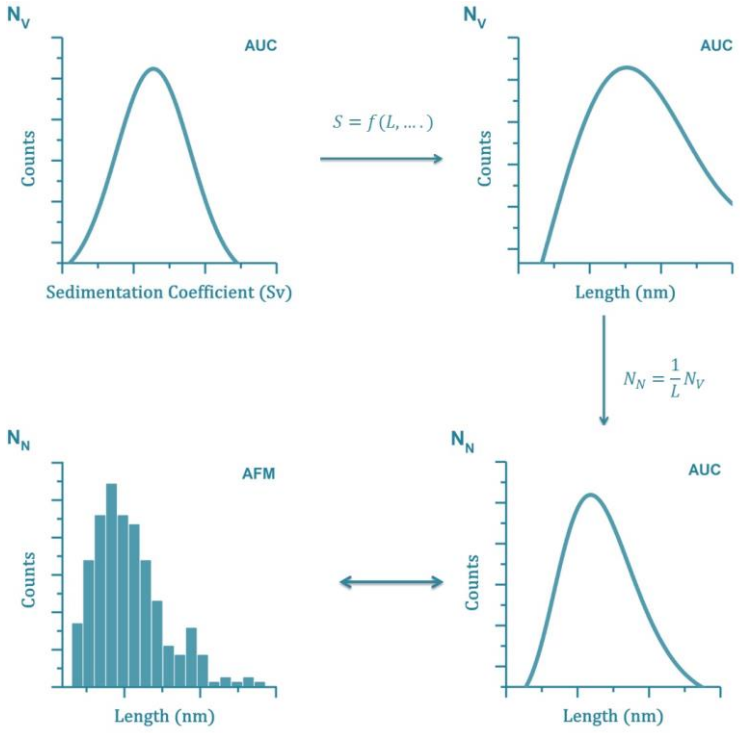

Figure 3.9: Schematic illustrating the data processing procedure. [Reproduced from 179]

It has to be considered that the absorbance of a particle scales with its volume and hence, AUC measures a volume distribution N_V, unlike with AFM, which yields a number distributions N_N. In order to compare both, the AFM obtained length distributions have to weigh the AUC-derived c(L) with the volume of the CNT. Since in the experiment most CNTs have the same diameter, N_V has to be converted into N_L by division with L.

$$N_N = \frac{1}{L} N_V \tag{3.2}$$

Otherwise, an overestimation from the presence of long CNTs would occur, since longer tubes absorb more light. The effect can be clearly observed in Figure 3.10 (a), where a comparison of AUC-derived length distributions c(L) and c(L)/L with the reference AFM data is shown.

In order to obtain a good fit between the AUC-derived length distribution c(L)/L and the AFM length distribution, the challenge is to find a function that maps the sedimentation coefficient, s, onto the nanotube length, L. Such a function critically depends on the friction coefficient, f.

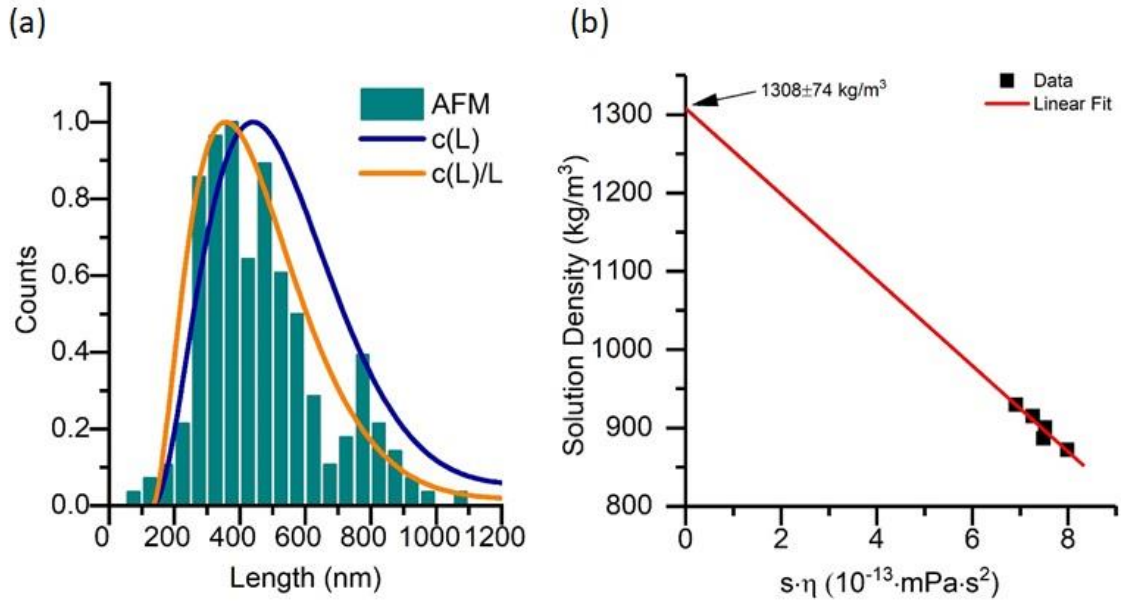

Figure 3.10: (a) Comparison of different length distributions. The AUC derived volume distribution c(L), converted number distribution c(L)/L along with AFM reference data, a number distribution. All data are of the same sample (b) Density determination of PFO – wrapped (7, 5) SWCNTs via AUC measurements in mixtures of toluene/toluene-d8. [Reproduced from 179]

In AUC under steady-state conditions (reached within 2 min), the centrifugal force, F_C, is balanced by the friction force, F_F, and these forces are defined as

$$F_F = f \cdot v_t \tag{3.3}$$

$$F_C = m_e \omega^2 r \tag{3.4}$$

where v_t is the terminal velocity (here ~100µm/min), m_e is the effective mass of the particle, ω is the angular velocity, and r is the distance of the object from the center of rotation. The sedimentation coefficient s is defined as the ratio of the terminal velocity to centrifugal acceleration

$$s = \frac{v_t}{\omega^2 r} \tag{3.5}$$

Equation 3.5 can be rewritten using equation 3.3 and 3.4 and $m_e = m.\left(1 - \frac{\rho_s}{\rho_p}\right)$. We obtain

$$s = \frac{V_P(\rho_P - \rho_s)}{f} \overset{\text{CNT}}{\Longrightarrow} \frac{\pi R_{eff}^2 L(\rho_t - \rho_s)}{f} \tag{3.6}$$

with V_P being the volume of the particle, and ρ_P, $\rho_s$and ρ_t being the density of the particle, solvent, and nanotube, respectively. For a CNT, s is expressed in terms of L and the effective nanotube radius, R_{eff}, which includes the polymer shell. The density of PFO-wrapped (7, 5) SWCNTs in toluene ρ_t = 1308 ± 74kg/m^3 was determined experimentally (Figure 3.10 (b)), which lies within the range of buoyant and anhydrous densities, reported for ionic-surfactant-wrapped SWCNTs in aqueous dispersions.[175,187,189,190] Furthermore, pressure- and temperature-corrected values were used for the toluene density and the toluene dynamic viscosity, ρ_s = 872kg/m3 and η = 0.622mPa s, respectively[191] (details in the appendix). Then R_{eff} and f remain as unknowns.

Modeling of sedimentation experiments is simplified in the case when the fluid flow around the SWCNT is laminar. Since the Reynolds number of the system given by $R_e = \rho_s v_t L/\eta$ is calculated to be less than 10^{-5}, a laminar flow is assumed for such a condition. The rigid-rod models were first used to calculate f and to find the desired function s(L). Rigid-rod models that are appropriate for smooth objects with a large aspect ratio have been successfully used in previous AUC works to describe the hydrodynamic behavior of ionic-surfactant-wrapped CNTs in water.[175] The same slender body theories were applied in this work (see appendix). These theories have in common that f is proportional to a logarithmic function of L/R_{eff_rod},[192–195]and here one of the hydrodynamic rod model is discussed, called the Mansfield Douglas[195] model for the friction, f

$$f = \left[6\pi\eta R_{eff_{rod}} A\left[\ln\left(\frac{4A}{e}\right)\right]^{-1}\right] \cdot \left[\frac{1 - 0.782t + 0.691t^{1.67} + 0.622t^{1.77} + 0.418t^{2.16}}{1 - 0.677t + 1.601t^{2.07} + 0.178t^{2.26}}\right] \tag{3.7}$$

with $t = (\ln A)^{-1}$ and $A = L/2R_{eff\_rod}$. Using Equation 3.6 and 3.7, the $c(L)/L$ from $c(s)$ for fractions with different lengths have been calculated and compared with the AFM reference data. In this approach, the only free parameter is R_{eff}, which was varied to obtain the best fit to the data by using the method of least squares. R_{eff} in Equation 3.6 is the radius of an effective cylinder, whereas R_{eff_rod}in equation 3.7 describes the location of the apparent radial plane of shear. These two radii must not share the same value as per the definition but since R_{eff} is used as an effective free parameter, its precise value does not matter as long as we can find an R_{eff} value to fit the data. Figure 3.11 shows that such an R_{eff} value does not exist. The Mansfield Douglas model systematically overestimates the population for the longer CNTs (Figure 3.11 – blue line) and this is observed for all fractions and also for all the rod models mentioned in the appendix.

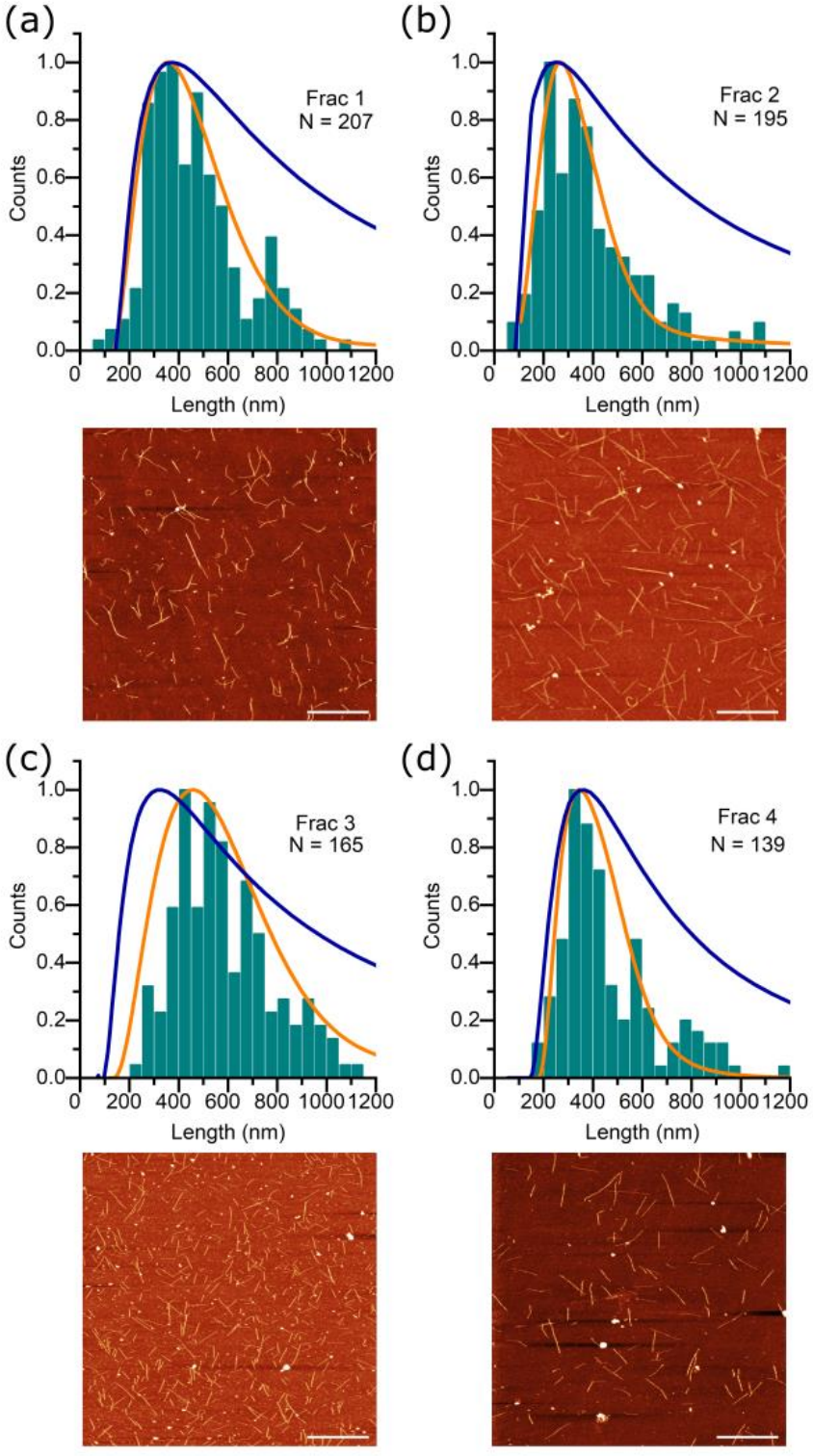

Figure 3.11: AFM reference data represented in histogram compared with AUC derived length distribution from the rigid rod model (blue lines) and flexible chain model (orange lines). Four different samples are compared here of different length distributions and their corresponding AFM micrographs are shown below each distributions. Scale bars in the AFM micrographs equals 2 μm for fraction 1, 3, 4 and 1 μm for fraction 2. [Reproduced from 179]

Besides R_{eff}, the fixed parameters ρ_t, ρ_s, and η were also varied nominally but any combination could not yield a good fit. The problem can be traced back to the shape of the $s(L)$ curve, which for rigid rods is unsuitable to properly map $c(s)$ onto $c(L)/L$. Varying all the above mentioned parameters merely changes the offset of the $s(L)$ curve and changing to other rigid rod models do not change the overall shape of the $s(L)$ curve as well. Eventually, a conclusion was drafted that the logarithmic length dependence of the friction coefficient is not an appropriate description for PFO-wrapped (7, 5) SWCNTs and $s(L)$ functions were explored empirically to solve the problem. Surprisingly, a square root length dependence of the frictional coefficient fixes the problem as mentioned below.

$$s = b\sqrt{L} \tag{3.8}$$

Using the above equation allows mapping of the AUC length distribution very well onto the AFM reference data for all fractions of (7, 5) SWCNTs (Figure 3.11- orange line). The coefficient b, which is the only free fit parameter, was found to be very similar in all datasets, with $b \approx (1.9 \pm 0.3) \times 10^4\ \mathrm{Sv/m^{1/2}}$.

If both Equation 3.6 and Equation 3.8 were equated

$$\frac{\pi R_{eff}^2 L(\rho_t - \rho_s)}{f} = b\frac{L}{\sqrt{L}} \tag{3.9}$$

It is clear that b has to depend on ρ_t, ρ_s, η, and R_{eff}. Since these parameters are identical for all fractions of PFO-wrapped (7, 5) SWCNTs, it is reasonable that similar b values were observed for all datasets. For other CNTs with (n, m)s, however, different values of b are expected and we look forward to generate an empirical b versus (n, m) calibration table for the future to make this method viable for all the chirality to the polymer combinations.

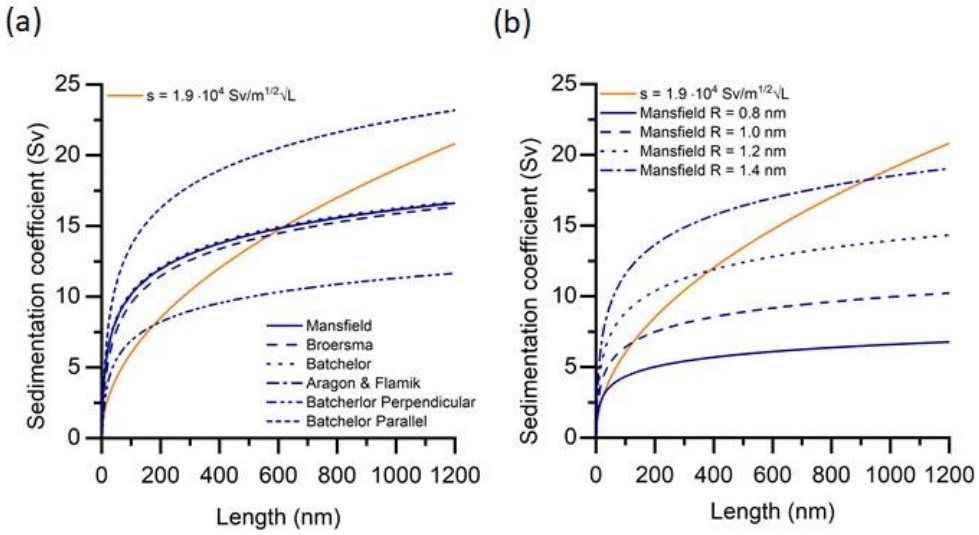

Figure 3.12: $s(L)$ for (a) different rigid rod models (blue lines) for a fixed diameter and (b) for a single model with different diameters compared to the flexible model.

Unfortunately, a microscopic explanation for the square-root length dependence of the friction coefficient cannot be provided. Figure 3.12 (a) shows the comparison of different rod models with the square-root model and Figure 3.12(b) shows the comparison of different fit radius for a rod model. However, the

flexible long chain molecules also exhibit a similar relation of $s \sim \sqrt{L}$ dependence.[196,197] This raises a question whether thermal fluctuations of PFO-wrapped (7, 5) SWCNTs could play a role here on long AUC time scales, although the nanotubes are smaller than 3 µm and are assumed to be straight.[197] At the moment, the origin of the observed length dependence is not clear, but the influence of the polymer side chains of the attached polyfluorene molecules has to be taken into consideration as well and might be resolved by MD simulations in the future. A concern that interaction between nanotubes could influence the sedimentation velocity has been addressed. Such an interaction will come into play once the concentration of the nanotubes per unit volume exceeds the critical concentration. A concentration above which the collective motion might set in can be estimated by the inverse swept volume. As shown in Table 3.1 and Table 3.2 below, critical concentration is not exceeded and we conclude that nanotube–nanotube interactions are not significant. In agreement, dependence of the prefactor b on the mean length of a fraction was not observed.

Fraction	Average length (nm) – from AFM	concentration (mol/l) - using S11 peak value	Concentration (mol/l) - using area under curve
1	367	6.5E-9	1.2E-7
2	270	2.0E-8	3.5E-7
3	554	5.9E-10	1.2E-8
4	370	7.5E-9	1.5E-7

Table 3.1: The concentration and the swept volume was determined from the absorption and AFM measurements for various fractions. The analysis of the concentration is based on the absorption cross-sections from [Streit et al. (Nano Lett. 14, 1530; 10.1021/nl404791y)] and we have used the S11 peak absorption as well as the integrated absorption under the S11 peak:

Length (nm)	Critical concentration (mol/l)
200	4.0E-7
300	1.2E-7
400	5.0E-8
500	2.5E-8
600	1.5E-8

Table 3.2: Calculating the critical concentrations corresponding to one tube per swept volume 4/3*pi*(length/2)^3 (J.K.G. Dhont et al., Colloids and Surfaces A: Physicochem. Eng. Aspects 213, 131; 10.1016/S0927- 7757(02)00508-3) yields:

To conclude, the length distributions of monochiral SWCNT in an organic solvent were measured for the first time using analytical ultracentrifugation. For PFO-wrapped (7, 5) SWCNTs in toluene, an unexpectedly simple correlation between the sedimentation coefficient and the nanotube length ($s = 1.9 \times 10^4\ \mathrm{Sv/\ m^{1/2}} \cdot \sqrt{L}$) has been found empirically, which enables calculating the length distribution from the sedimentation coefficient distribution. The underlying square-root length dependence of the friction coefficient suggests that shape fluctuations might come into play during the centrifugation process; however, a microscopic model taking into account the attached polyfluorene polymer has yet to be developed. The results have been benchmarked with AFM reference measurements by converting volume to number distributions. The approach has the potential for routine in situ length characterization of PFO wrapped SWNTs in organic solutions as is required during nanotube solution processing.

3.5 Nanotube Device Fabrication

Over the years, photocurrent studies have been carried out on CNTs deposited on silicon substrates and contacted with metal electrodes from the top. On the other hand, the CNTs are grown from one electrode to the other using CVD or laser ablation technique and the metallic tubes are burned electrically after metalizing the contact on the top of the nanotubes. However, it is significant how the orientation of the contact is i.e. either from the top or bottom, the behavior of the devices differs on it and are fabricated depending on the convenience of the facility. A solution processed single (n, m) CNTs have been incorporated into devices as stated above for the investigation in this thesis.[138,198–200]

3.5.1 Fabrication of Metal Electrodes

In order to generate the electrode structures for the nanotube devices, electron beam lithography (EBL) was used to pattern the chips. In this thesis work, four different wafer materials were used, namely silicon wafers with $300\ \mathrm{nm}$ and $800\ \mathrm{nm}$ oxide, sapphire substrates and silicon on insulator substrates with 250nm silicon on top of $3\mu\mathrm{m}$ oxide thick silicon wafer. Each of these wafers were cut into $1 \times 1\ \mathrm{cm}^2$chips, and were thoroughly rinsed with acetone and iso-propanol (IPA) followed by oxygen plasma treatment using a table top plasma cleaner from Dieter Electronics at $0.2\ \mathrm{mbar}$, $50\ \mathrm{sccm}$, $200\ \mathrm{W}$ RF for 2 min. A few mL of poly - methyl methacrylate (PMMA -950K A4.5 –positive photoresist) dissolved in Anisol was then spin coated at $5000\ \mathrm{rpm}$ for 3 min, which formed a $\sim 200\mathrm{nm}$ thick layer.

Then the spin coated sample was pre-baked at 160 °C for 30 min in order to remove the residual solvent, and the samples were placed inside a scanning electron microscope (Zeiss LEO 1530 Gemini) for e-beam lithography.[201] The electrode structure was designed using CAD Elphy-32 software, and consisted of a common drain electrode and 12 floating source electrodes positioned in a 2 × 6 array with a $800\mathrm{nm}$ source - drain gap in between as a standard structure. Therefore, each structure yielded 12 CNTFETs after nanotube deposition. Additionally, 2 pads were also included in the structure, which were used to probe the bottom gate from the top of the wafer. The designs were optimized and changed for every substrate material used (along with the device geometry).

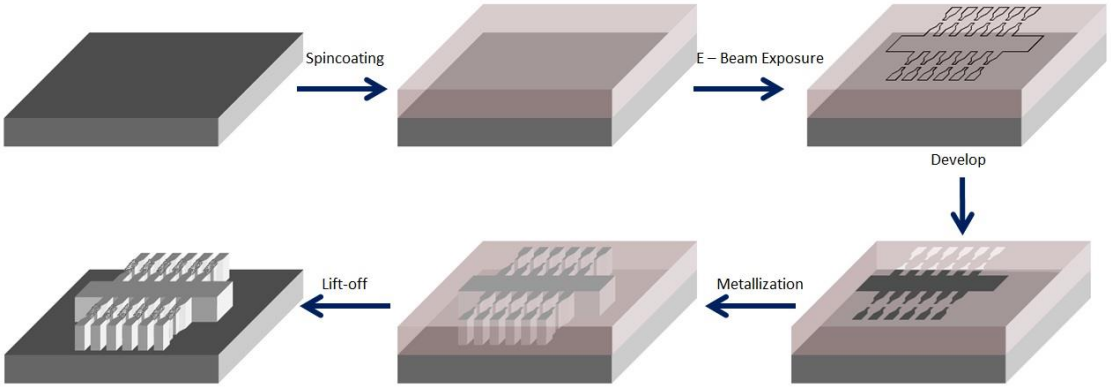

Figure 3.13: Fabrication of Metal Electrodes

An electron beam with an exposure dose of $360\ \mu C/cm^2$ at $30\ kV$ was then used to pattern the desired layout. On collision with high energy electrons inside the SEM, the PMMA breaks into smaller chains of

lower molecular weight which could be dissolved away with the right solvent. In this thesis, a mixture of methyl isobutyl ketone (MIBK) and IPA (1:3 ratio) was used to dissolve away the exposed PMMA. The sample was immersed in MIBK : IPA solution for 30 sec to dissolve the exposed material and generate a mask for metallization.

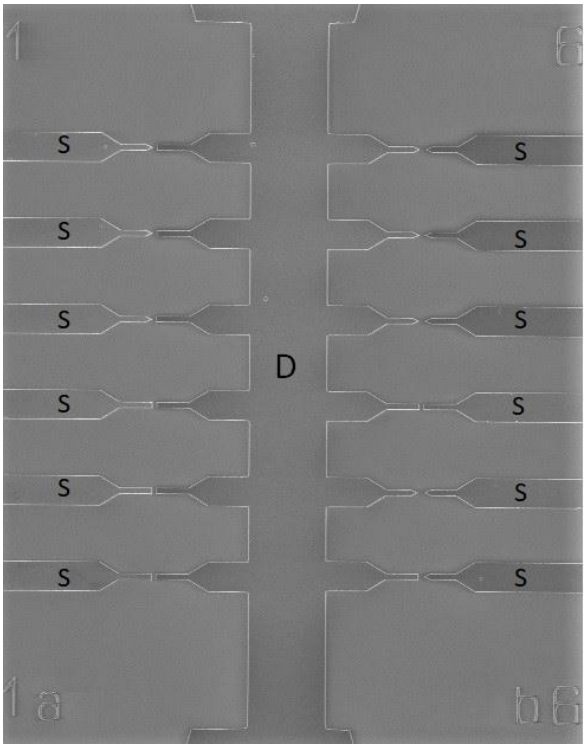

Figure 3.14: SEM micrograph of the fabricated source (S) and drain (D) electrodes of the standard structure

Depending on the substrate used, the back gate of the substrate has to be electrically connected. For this purpose, the oxide layer was scratched from the silicon substrates using a diamond scriber, while for the sapphire substrates, a metallic back gate was pre-fabricated using the same process mentioned above and then covered with a dielectric using atomic layer deposition (ALD). The metallization process was carried out using magnetron sputtering and molecular beam epitaxy (MBE).

Magnetron sputtering is carried out with the DC or RF power given in table 3, where a target plate is bombarded by a energetic ions generated in a glow discharge plasma, generated under the pressure of $5 \times 10^{-4} mbar$. The plasma is situated in front of the target and the bombardment process causes the removal of target atoms (sputtering), which then condenses on a substrate.[202] A thin wetting layer of chromium of $\sim 3.5\ nm$ was deposited initially, followed by palladium $40\ nm\ -\ 80\ nm$ depending on the substrate design and used as the contact electrode for the nanotube devices.

Metal	**Power [W]**	**Rate [nm/min]**
Chromium	100 W (RF)	7
Palladium	70 W (DC)	27

Table 3.3: Parameters for metal deposition using magnetron sputtering

MBE was carried out by heating the material of interest in a closed effusion cell. This develops a pressure inside the effusion cell due to the heating of the metal beyond the boiling point. The sample was placed in a cooled stage at $-123℃$ inside an ultra high vacuum chamber maintained at $1 \times 10^{-9} mbar$. Once the effusion cell is open, the difference in the vapour pressure causes the metal to deposit on the cooled substrate. A thin wetting layer of titanium $\sim 5\, nm$ was deposited initially, and followed by aluminum $\sim 80\, nm$ for the sapphire substrates to generate back gates.

Metal	Shutter open temperature[℃]	Deposition temperature[℃]	Rate [nm/min]
Titanium	1200	1640	0.5
Aluminium	1000	1200	6.5

Table 3.4: Parameter for metal deposition for the Molecular Beam Epitaxy (MBE)

3.5.2 Dielectrophoresis

In order to make the nanotube deposition by dielectrophoresis from solution work well, the suspensions were sonicated for 2 to 3 minutes and diluted in order to lower the nanotube concentration to ~1 CNT/µm^3 to ensure individual CNT deposition and to avoid aggregation prior to touch down. Dilution also reduces the amount of polymer content for the higher fractions as explained in the previous chapter, as well as the metallic nanotube concentrations if present. The samples were then contacted on a probe station (Cascade Microtech GmbH), where 50 µL of the CNT suspension was dropped on top. Due to the negligible ion concentration in the polymer wrapped suspensions, DC-Dielectrophoresis is used for all the suspensions in this thesis. The DC bias is applied between the gate and common electrode for the global back gate samples, and between the source and drain for sapphire and SOI samples. Typically, a voltage bias up to 6 V was applied for silicon with natural oxide substrates (Si/SiO_2 – Drain| Gate Bias) and the SOI substrates (Source – Drain Bias). The DC bias was applied for 5 min using a DC sourcemeter (Keithley 2400), when depositing nanotubes from toluene - based dispersions.

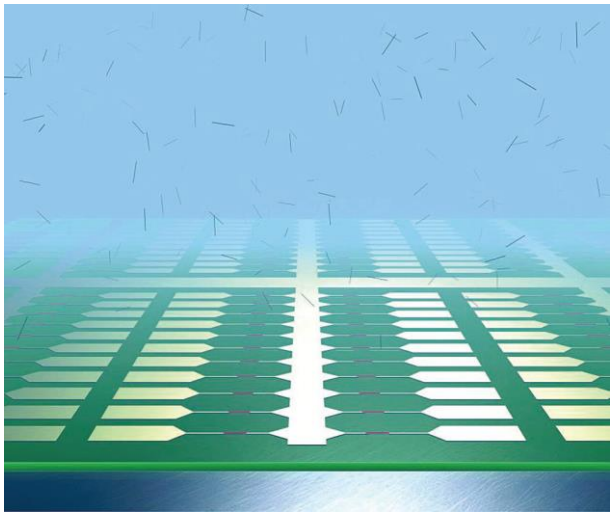

Figure 3.15: Illustration of dielectrophoretic deposition of CNTs by applying DC or AC bias based on toluene or water based dispersion respectively [Depicted from A. Vijayaraghavan et al. Nano. Lett. 2007][56]

The samples were then rinsed three to four times with toluene to remove the excess polymer, while keeping the bias turned on. Finally to ensure the removal of the solvent completely, the samples were then annealed at $100°C$ for 90 minutes. This reduces hysteresis and also increases the on - current due to suspected change in metal work function and hence the Schottky barrier. Typically, 10 - 15 tubes were deposited across the source to drain electrode gaps, which was sufficient to generate a detectable photocurrent signal in the system as described in Chapter 5.

Such CNT devices show p-type characteristics when in contact with palladium due to the close positioning of the Fermi level of palladium to the valence band of the nanotube, thereby reducing the Schottky barrier for holes.[203] In addition, these characteristics can also arise from the trap states due to the adsorbates near the conduction band which inhibit the electron flow.[204] These adsorbates are generally environmentally adsorbed oxygen on the surface of the nanotubes.[205]

3.5.3 Electrical Characterization

The devices were initially characterized electrically by using transconductance measurements before conducting the photocurrent measurements to obtain the transistor characteristics (on/off ratio). All the measurements presented in this thesis were obtained after samples were wire – bonded onto a ceramic package (Figure 3.16 (a, b)). The samples were bonded using a Universal Wedge Bonder - Model 4123, equipped with Al - Si 1% wires, and utilizing minimum stress on the metal pads and the oxide underneath.

Figure 3.16 (c) displays the holder, where the chip was placed for characterization. Its internal circuitry (Figure 3.16(d)) consists of individual switches corresponding to the 16 pins of the package. Each electrode was wire - bonded onto a pin labelled 1 to 16. Furthermore, the groups 1 to 12, 13 to 14 and 15 to 16 were electrically connected, thus yielding three coaxial outputs corresponding to the source, drain, and gate as a standard configuration to measure samples on silicon substrates. Using this configuration, single or multiple devices can be characterized at a time. However, the holder was reconfigured for the sapphire samples, later shown in this thesis, as its device configuration had two gates to be controlled individually.

The measurements were performed in ambient conditions using an Agilent 4155C semiconductor parameter analyzer. Individual devices were connected via triaxial probes having a detection limit less than 40 fA. The Desktop Analyzer software was used to operate the Agilent 4155C. Measurements were carried out at 3 different sources - drain biases. The sweeping range of the gate voltage depended upon the thickness of the dielectric in order to avoid breakdown or charging up. For a thick oxide such as $800\ nm$, the device was biased with gate voltages up to $\pm 30\ V$ at $200\ mV$ intervals. With a large dielectric strength ($> 10^7\ V/cm$), the applied voltages are insufficient to initiate electrical breakdown of the oxide layer.[206] On the other hand for thinner oxides such as $50\ nm$, this was reduced to $\pm 3\ V$ at $200\ \mu V$ intervals. All the measurements were carried out with 5 power line cycles (NPLC) and with no delay time between the measurement steps.

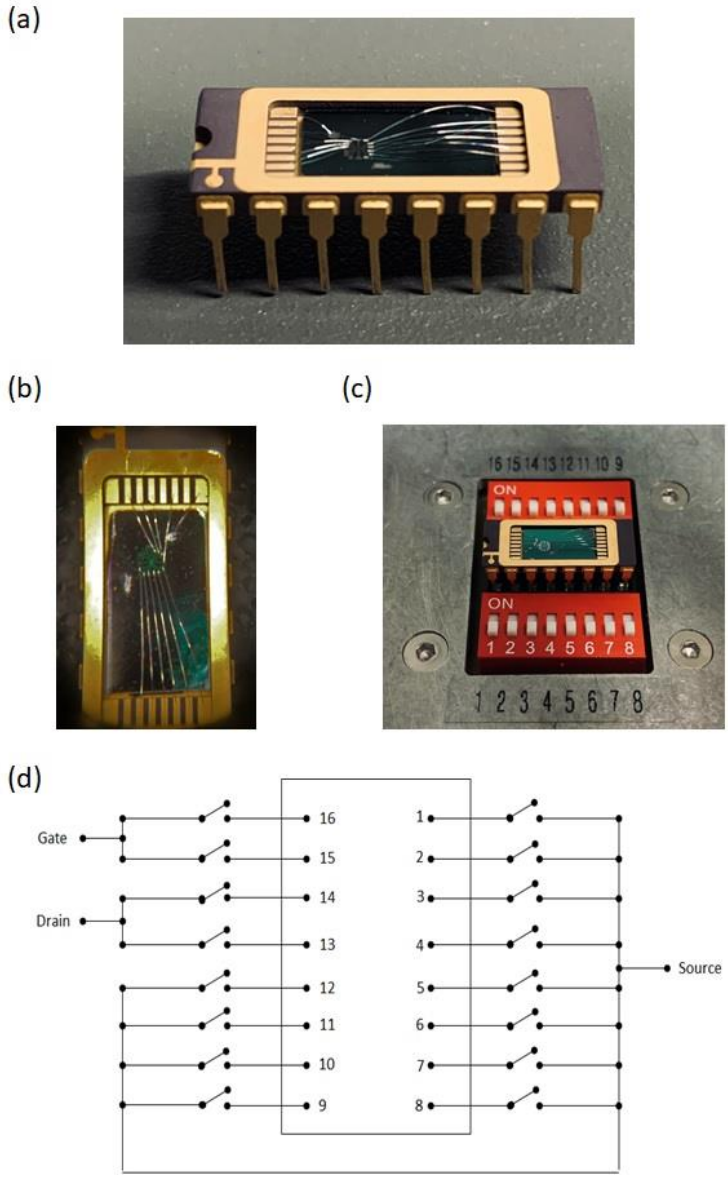

Figure 3.16: (a) Fabricated sample wire - bonded on to a chip carrier. (b) Zoomed in top view of (a). (c) Chip carrier holder for the electrical measurements. (d) Internal circuit diagram of the chip holder.

4 Photocurrent Spectroscopy: Experimental Methods

Carbon nanotubes (CNTs) have different optical transitions over a very large range of the spectrum defined by their chirality. CNT dispersions prepared with previously discussed techniques contain various types of SWCNTs with S_{11} transitions ranging from 800nm to 1500nm. In order to perform spectroscopy measurements, a tunable quasi-monochromatic light source with high spectral resolution large enough to resolve the collected photocurrent signal from the devices is required. In this thesis, a commercially available supercontinuum light source (SuperK Extreme, NKT Photonics) was used to illuminate the fabricated devices. It consists of a pulsed monochromatic 5 ps seed laser of 1064nm, feeding the pulsed light along a solid-core photonic crystal fiber (PCF) at a repetition rate of 80 MHz. The electric field confinement inside the fiber leads to non - linear effects and consequently to spectral broadening.[207,208] The unpolarized light emerging from the supercontinuum source is then collimated into an acousto- optic tunable filter (AOTF) (SuperK SELECT, NKT photonics) to select the wavelength for conducting spectral studies.

There are other light sources available that could be used for illumination purposes, such as superluminescent light-emitting diodes (SLED), amplified spontaneous emission (ASE) sources, and incandescent or thermal sources. Although the incandescent source has a broad spectrum as a PCF supercontinuum light source, its intensity is quite low compared to the other. The SLED and the ASE sources do not have a wide range of spectrum compared to the former two, as shown in Figure 4.1 below. Hence, the PCF based supercontinuum source is the preferred option for the broad wavelength range of interest (500 nm – 2100 nm).

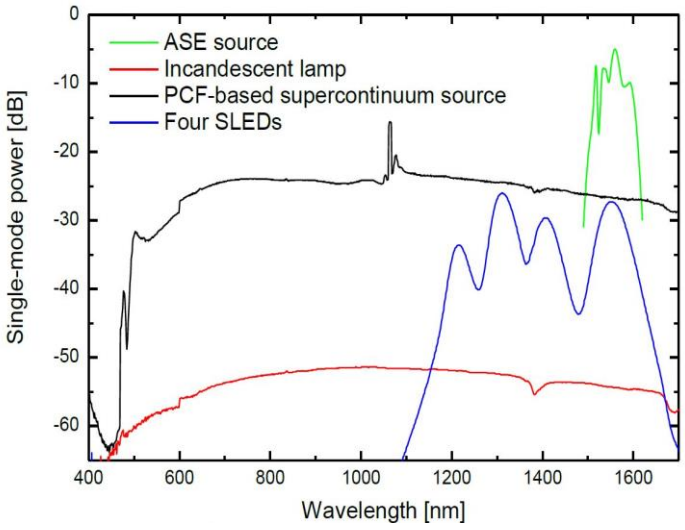

Figure 4.1: Comparison of different light spectral sources (reproduced from NKT photonics application note)

4.1 Supercontinuum Light Source

Supercontinuum laser technology combines conventional broadband light sources with the properties of single-mode lasers. They are capable to cover a broad range from 400nm to 2400nm emitted as a continuum with an integrated power of up to several watts. As mentioned above, supercontinuum generation is the formation of the continuous spectrum by the propagation of high power pulses through a non-linear media, first reported in 1970 by Alfano and Shapiro.[209,210]

Supercontinuum refers to a plethora of nonlinear effects which in combination, lead to a spectral broadening of optical pulses and, thereby potentially octave-spanning output. The nonlinear effects involved depend on the nonlinear material, effects like self-phase modulation (SPM), Raman Scattering, phase matching along with soliton dynamics, etc. With enough power, supercontinuum generation can be observed even in the air and a drop of water. With a clever dispersion design, power requirements can be significantly reduced. The widest spectrum is obtained when the pump pulses are closer to the zero-dispersion wavelengths of the nonlinear media. In this regard, the nonlinear photonic crystal fiber with zero dispersion wavelengths close to the pump laser wavelengths were the pioneer combination leading to a boom for the supercontinuum experiments. However, the nonlinear effects have a significant effect on the pulse duration.

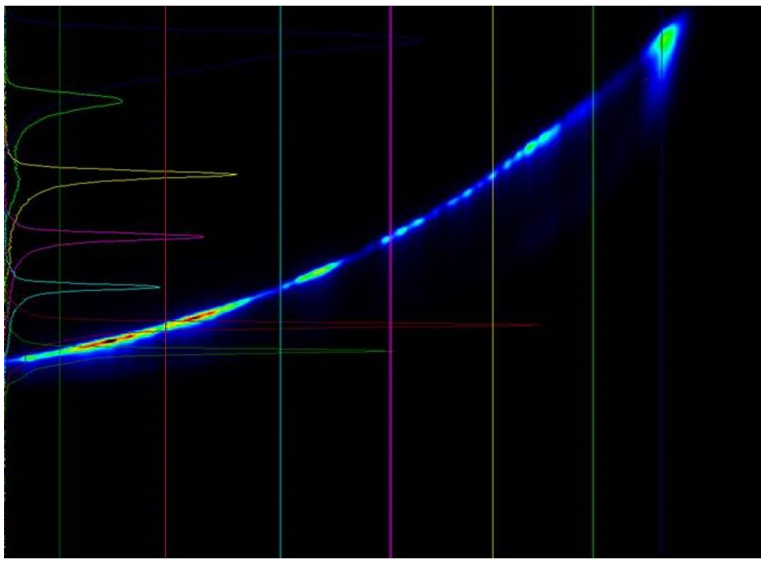

Figure 4.2: Streak camera plot of EXW-12 SuperK Extreme light source. X-axis (Wavelength):~775 nm-420 nm, Y-axis (Time): 0-1 ns (Source: NKT Photonics)

Figure 4.2 shows the streak camera measurement of the NKT SuperK Extreme EXW-12 source output used in this thesis work, with wavelength on the x-axis (~775 nm (Left) – 420 nm (Right)) and time on the y-axis (~0 ns (bottom) – 1 ns (top)), the figure shows pronounced curvature towards shorter wavelengths, indicating longer pulse duration. The pulses of the laser are chirped due to the dispersion from the PCF. The wavelengths near the seed laser (1064 nm) have a shorter pulse duration and the pulse duration increases, as we get farther away from the seed laser wavelength in both directions (IR region not shown). The pulse duration of the total spectrum from the seed laser at 1064 nm to 400 nm or 2400 nm is about 700 ps for the supercontinuum laser source used. The vertical line profiles show the pulse duration at fixed wavelengths, ranging from ~ 10 ps -100 ps as tabulated in Table 4.1.

Wavelength	Pulse Duration	Line profile colors
470 nm	81 ps	Darl blue
500 nm	45 ps	Green
550 nm	22 ps	Yellow
600 nm	19 ps	Pink
650 nm	16 ps	Cyan
700 nm	14 ps	Red
750 nm	13 ps	Dark green

Table 4.1: List of line profiles from Figure 4.2, with corresponding wavelengths and pulse duration (Source: NKT Photonics).

In the green line profile at 500 nm displays a shoulder in the time domain, a pre-pulse is present along with the main pulse at 45 ps FWHM. Depending on the measurement technique different pulse duration is observed, but with single-photon detectors, the pulses can also be wider.

4.1.1 Nonlinear Photonic Crystal Fiber (PCF)

The efficiency of a supercontinuum source relies on the nonlinear medium with tailored dispersion and nonlinearity. Every commercially available supercontinuum source consists of a pulsed pump laser and a custom-designed micro-structured fiber called the nonlinear photonic crystal fiber that serves as the non-linear media. A standard fiber guides light from one end to the other end by total internal reflection with a high refractive index core and a low refractive index cladding. The term photonic crystal arises from the unique cladding structure used in the fibers. In PCFs, the refractive index variation is achieved by forming a matrix of different materials with high and low refractive indices referred as a hybrid material. The hybrid cladding is thus configured according to the requirements.

The fibers are generally fabricated using a combination of high purity fused silica and air holes, and not any crystalline material as the name indicates. Out of the two fundamental classes of PCFs, namely the index guiding and light confining fibers, the supercontinuum generation relies on the index guiding PCFs. An index guiding PCF comprises a solid glass high-index core embedded in an air-filled cladding structure where several air holes are arranged in a pattern that runs along the length of the fiber, thus creating a hybrid air-silica material with a refractive index lower than the core.

Nonlinear fibers are typically designed with a pitch of $1 - 3\mu m$ and the microstructured region is about 20 to 50 % of the fiber cross-section. Unlike the standard fiber, the triangular PCFs do not exhibit a second-order mode cutoff, which is unique to them. Hence, they are called endlessly single-mode fibers and such condition can be realized by selecting sufficiently small holes in the cladding. On the other hand, larger holes make the fiber likely to be multimoded but due to the larger holes, the gaps between the holes become narrower making the silica core further isolated from the cladding. While the smaller holes make them single moded, the decrease in their effective refractive index makes them susceptible to bending losses. The condition of bending radius for low loss is as follows

$$R \gg R_C = \frac{8\pi^2 {\eta_{core}}^2 \rho^3}{\lambda^2 W^3} \tag{4.1}$$

where W is the dimensionless modal parameter, ρ is the core radius, η_{core} is the refractive index of the core, λ is the wavelength, and R_C is the critical bend radius before the bending loss in a waveguide becomes large.

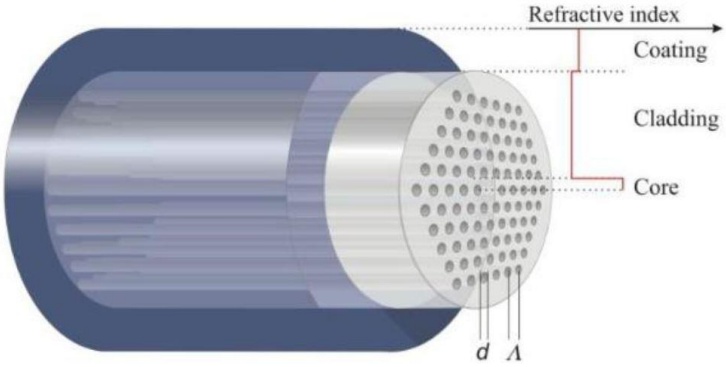

Figure 4.3: Schematic of a classical triangular cladding single core photonic crystal fibre. The light is transmitted through the central core embedded in the air holes. Here d is the diameter of the hole and Λ is the hole pitch.The layer denoted in grey is the high refractive index polymer coating for protection [reproduced from211].

4.2 Acousto Optic Tunable Filter (AOTF)

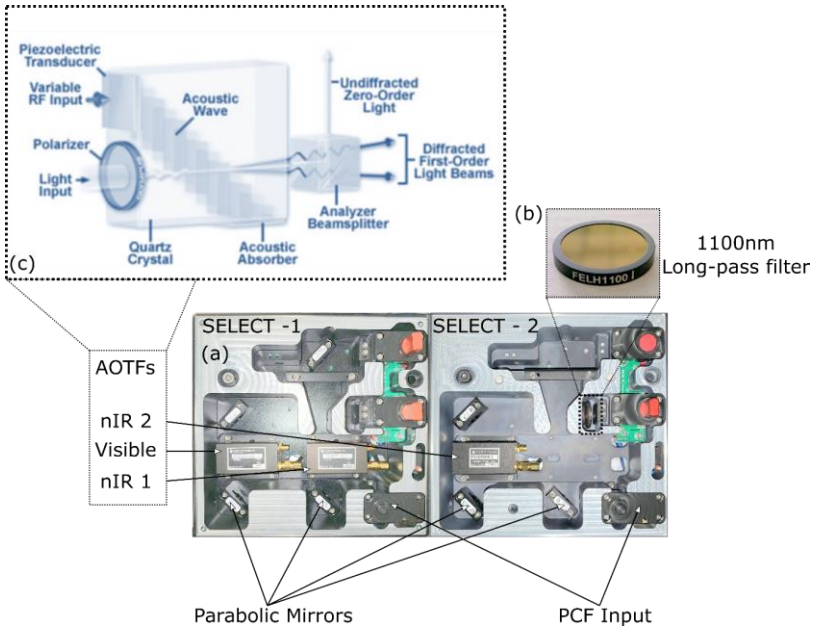

Figure 4.4: (a) Schematic layout of AOTFs: Top view of two NKT Select boxes with 3 AOTFs for ranges 500 nm-825 nm (Visible), 825 nm-1420 nm (nIR) and 1100 nm-2100 nm(nIR2).1100 nm (b) Long pass filter added to the beam path of nIR2 AOTF to remove high energy leakage light. (c) Schematic of a collinear AOTF configuration in crystalline Quartz [Application note Olympus life science]

On combining a supercontinuum source with a tunable spectral filter, the white light source is transformed into a tunable laser. The spectral filter consists of an anisotropic crystal, attached to a piezoelectric transducer. On applying a radio frequency (RF) electrical signal, the transducer generates a high vibrational frequency (acoustic) wave that propagates into the crystal. The alternating ultrasonic acoustic wave induces a periodic redistribution of the refractive index through the crystal that acts as a transmission diffraction grating or Bragg diffractor to deviate a portion of incident laser light into a first-order beam. When an acoustic wave propagates through the anisotropic crystal, it produces a periodic modulation of the refractive index via the elasto-optical effect. This provides a spatial modulation to an incident light beam. The so driven spatial modulation is then divided into two components, the transverse and longitudinal components. The transverse spatial modulation deflects the incident light beam with an angular distribution according to the frequency spectrum of the acoustic waves. This phenomenon constitutes the basis of acousto optic deflectors or Bragg cell – used for processing electronic signals. The spectral bandpass of the filter can be quickly tuned over the spectral regions by changing the RF signal frequency. Based on the direction of the interaction between the acoustics and the incident light, the AOTFs can be categorized as collinear[212] and non-collinear.[213] Typically, the RF signals applied are in the MHz range and it decreases with the increase in the wavelength. Also, the amplitude of the monochromatic light is directly proportional to the RF power. AOTF does not have any influence on the pulse duration, it only affects how narrow is the cut out from the white light pulse. A long pass filter from 1100 nm and below from Thorlabs is added to the beam path (Figure 4.4(b)) of the second NKT select box encasing the nIR2 AOTF crystal (1100 nm-2100 nm) to avoid any lower wavelengths of light leaking from the AOTF.

4.2.1 Fiber Coupling

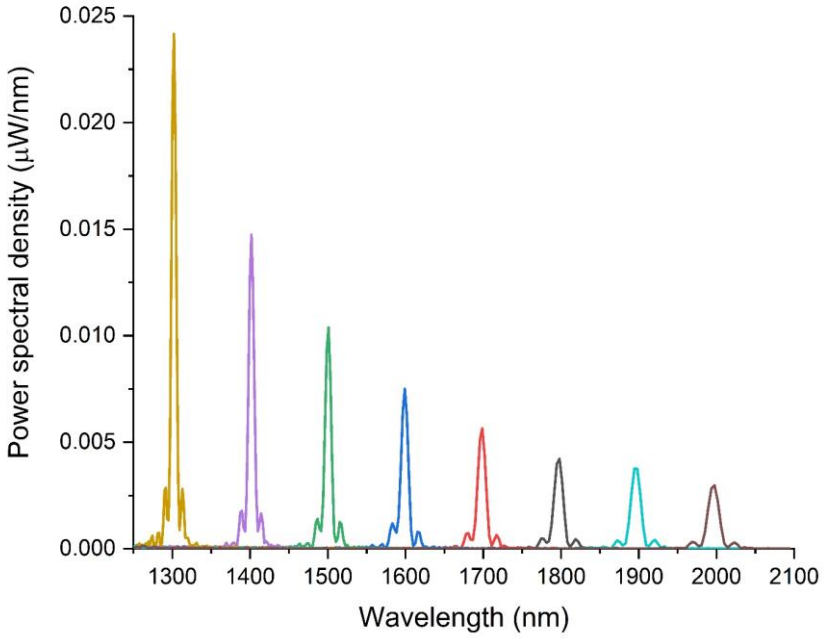

Figure 4.5: Spectrum of the nIR2- AOTF/FD6 –PM fiber output measured with Neospectra FTIR spectrometer.

The combination of the supercontinuum and AOTF constitutes a tunable light source. The monochromatic light emanating from such a system is then coupled on to a broadband single – mode fiber. This coupling is achieved using commercially available SuperK Connect and a fiber delivery system from NKT photonics. The coupling process is fine-tuned by manipulating two parallel aligned mirrors to couple the light on to the fiber delivery system. In order to gauge the coupling, a spectrometer is used to ensure that the best light intensity is achieved and the chosen wavelength is coupled on to the optic fiber on the other end. Three optic fiber types FD7, FD9 and FD6 from NKT photonics were used for wavelength ranges 500 nm-825 nm, 825 m-1420 nm and 1100nm-2100 nm respectively, where FD7 and FD9 are endlessly single-moded and FD6 is a polarization maintaining fiber. Typically, two spectrometers were used to calibrate the source in different spectral ranges. HR400 spectrometer from Ocean Optics was used for a range from $500\text{nm} - 1100\text{nm}$, while beyond 1100nm uptil 2200nm, Fourier transform infrared (FTIR) spectrometer – SWS62221-2.1 from Neospectra was used. Figure 4.5 shows the output spectra from nIR2-AOTF/FD6-PM fiber measured with Neospectra FTIR spectrometer. The power spectral density is the Fourier transform of the interferogram generated inside the spectrometer.

4.3 FTIR Spectrometer Intensity Calibration

In order to calibrate the FTIR spectrometer, a standard with known characteristics is required, such as the calibrated light source from Ocean Optic - HL-3P-INT-CAL-EXT. The source is calibrated for absolute radiance from NIST – Figure 4.6 shows the calibrated data. The source emits over a diffuser of diameter 6 mm

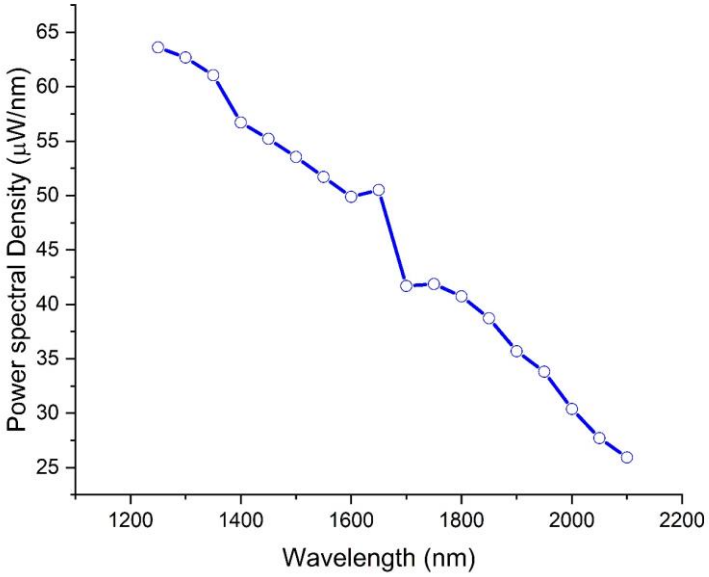

Figure 4.6:Power spectral density reference data of the NIST Calibration data for HL-3P-INT-CAL-EXT source

On modelling the HL-3P-INT-CAL-EXT light source as a circular Lambertian source, the radiation transfer between circular apertures, whose centers are located along the same optical axis and are set apart over

a fixed distance s. The ratio of the light that is detected by the detector is given by $\text{Ratio}\ (s) = \frac{E_d}{E_s}$, where $E_d$and $E_s$are the intensity at the source and the detector center[214]

$$\text{Ratio}\ (s) = \frac{2 \cdot r_s^2}{r_s^2 + r_d^2 + s^2 + \left[\left(r_s^2 + r_d^2 + s^2\right)^2 - 4 \cdot r_s^2 \cdot r_d^2\right]^{1/2}} \tag{4.2}$$

The approximation shown below in Equation 4.3 is obtained by assuming that the radii are completely negligible compared to the distance s between the source and the detector.

$$\text{Ratio P}(s) = \frac{r_s^2}{s^2} \tag{4.3}$$

where, r_s is the radius of the source, $r_d$is the detector radius, and s is the distance between the source and the center of the detector. Equation 4.3 is same as the relation that would be obtained from a point to point approximation. Taking the absolute values for $r_s = 3\text{mm}$, $r_d = 0.2\text{mm}$ and $s = 4\text{cm}$, $\text{Ratio}(s) = 5.593 \times 10^{-3}$ and $\text{RatioP}(s) = 5.625 \times 10^{-3}$ were calculated. It is clear that the difference is in order of 10^{-5} on considering the point to point approximation.

In order to match power spectral density data points from the NIST reference data (Figure 4.6) for the source with the power spectral density spectra from the FTIR spectrometer. The NIST reference data was interpolated and fitted with a 3rd order polynomial fit to remove any artefact from the NIST reference data as shown in Figure 4.7.

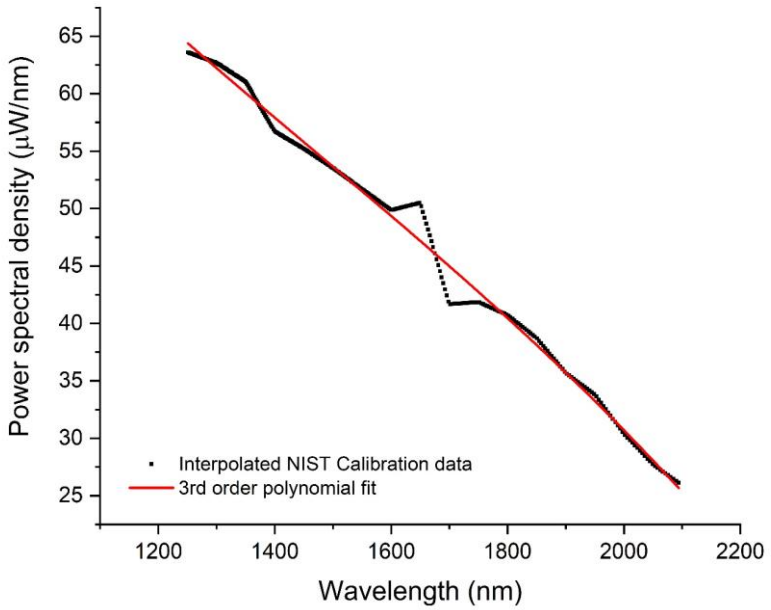

Figure 4.7: Interpolated NIST calibrated power spectral density data (Black) fitted with 3rd order polynomial fit (red).

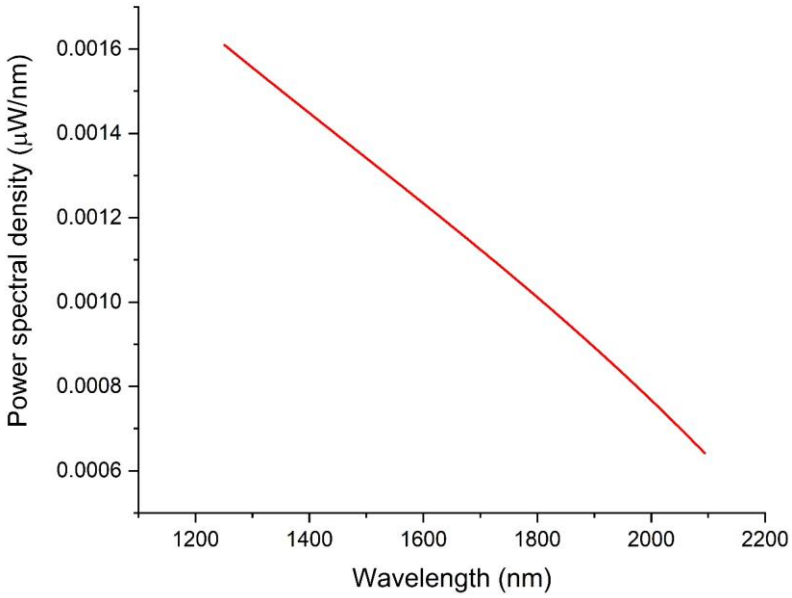

Figure 4.8: Calculated power spectral density of the 3rd order polynomial fit of NIST calibrated source transmitted, to the detector aperture (∅ 400um) when centro-symmetrically placed 4 cm apart from the source.

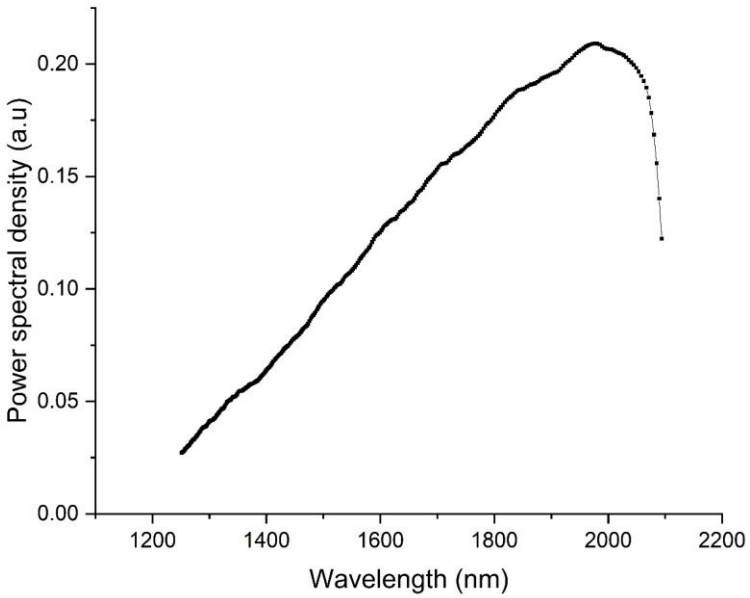

Figure 4.9: Power spectral density (PSD) measured at a distance of 4cm between the source centre and the detector centre.

As intensity is the power transferred per unit area, the ratio of intensity in Equation 4.2 and Equation 4.3 can be rewritten as the ratio of the intensities at the detector and source as follows

$$\frac{E_d}{E_s} = \frac{\frac{P_d}{A_d}}{\frac{P_s}{A_s}} = \frac{P_d}{P_s} * \frac{A_s}{A_d} \tag{4.4}$$

Where E_d is the intensity of light at the detector, E_s is the intensity of light at the source, P_d is the detected power of light at the detector, P_s is the emitted power of light at the source, A_d is the active area of the detector and A_s is the surface area of the Lambertian source or an emitter. On rearranging Equation 4.4 the power ratio is calculated to be $P_d/P_s = 2.5 \times 10^{-5}$, which should the correction factor for the intensity of light arriving at a detector which is placed 4 cm apart from the source. Figure 4.8 shows the calculated power spectral density of the 3rd order polynomial fit to the NIST calibrated source, transmitted to the detector aperture (∅ 400 µm) when centro-symmetrically placed 4 cm apart from the source. Measured power spectral density (PSD) from the spectrometer at source to detector distance of 4 cm is shown in Figure 4.9. The calibration curve is then given by the ratio of the curves in Figure 4.8 and Figure 4.9 and shown in Figure 4.10. The arbitrary units of the FTIR spectrometer can now be converted into µW/nm by multiplying with the calibration curve.

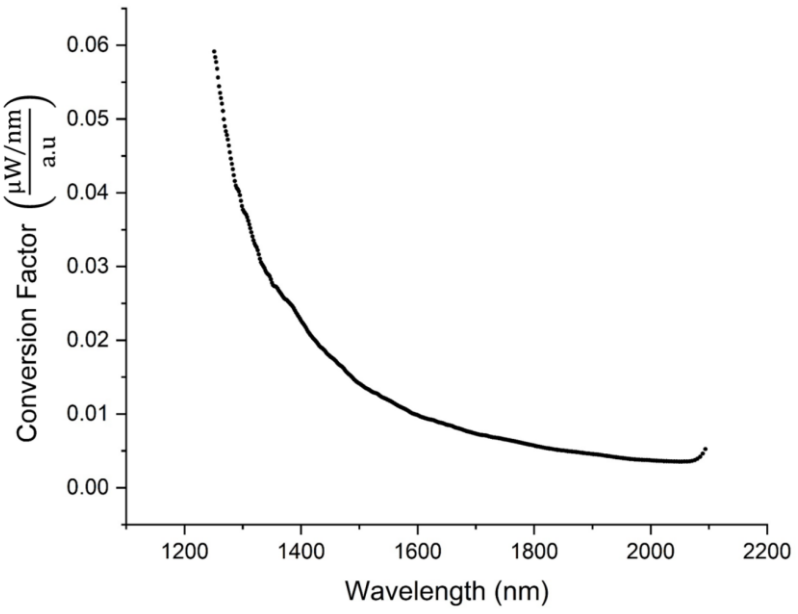

Figure 4.10: Calibration calculated power spectral density at the position of the detector (data in Figure 4.8) and the measured power spectral density (data in Figure 4.9).

4.4 Experimental Setup

The wavelength tuning range of an AOTF is limited for a single crystal by the piezo electric transducer. The SuperK SELECT from the NKT photonics accommodates up to two crystals, each designed with a specific spectral bandwidth. The beam from the light source is split according to the bandwidth of the appropriate filters. With two AOTFs accommodating in total 3 crystals, three wavelength ranges are accessible: visible $(500\text{nm} - 825\text{nm})$, the nIR $(825\text{nm} - 1400\text{nm})$ and nIR2 $(1100\text{nm} - 2100\text{nm})$.

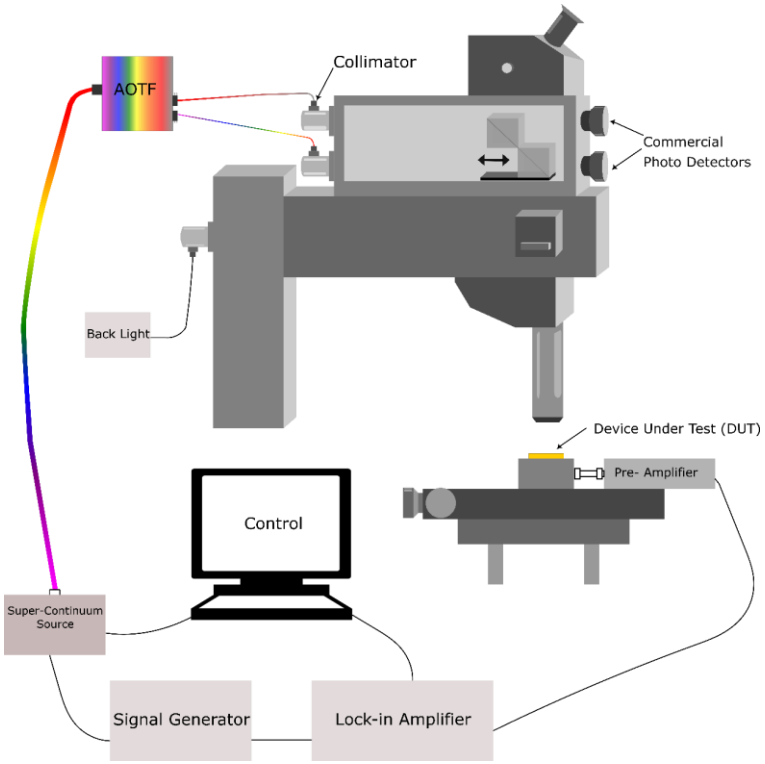

Figure 4.11: Schematic of the experimental setup

The Figure 4.11 shows the schematic of the experimental setup used to carry out the photocurrent experiments. The linearly polarized monochromatic light from the AOTFs is fiber coupled and delivered to a collimator on to a standard optical microscope (ZEISS Axiotech Vario). Each wavelength ranges are coupled on to the microscope using specific NKT photonic fiber delivery optic fibers: visible- FD7, nIR-FD9 and nIR2-FD6. The microscope houses an infinity corrected broadband microscope objective (100X MPLAN, Mitutoyo), a camera (Moticam Pro 252A, Moticam) and a photodetector (PC50-6, First Sensor). A customized module was added separately which houses two reflective collimators and two 90:10 beam splitters (Thorlabs) to guide the fiber coupled light towards the sample. The reflective collimator contains an off-axis parabolic silver mirror that can reflect over 95% of the beam over the range of $450\text{nm} - 20\mu\text{m}$. The collimated beam diameter could be calculated by $\mathrm{D} = 2 \times \mathrm{NA} \times \mathrm{f}$, where NA is the numerical aperture of the single mode fiber and f is the focal length of the parabolic mirror. The reflective collimator on an average provides a 2 mm beam diameter for a fiber NA of 0.13 and the collimator focal length of 7mm.

The two 90:10 beam splitter for visible (BS028, Thorlabs) and nIR (BS030, Thorlabs), which reflects the 90% of the collimated beam intensity towards the objective to focus on to the sample. The remaining 10% beam intensity is transmitted on to a calibrated photodiode (Ophir Photonics) PD300 and PD300IR or RM9

for visible and IR, respectively. As the beam-splitters have a specified range, a custom made module was built to accommodate two beam-splitters of desired ranges, *i.e.*, $500\text{nm} - 825\text{nm}$ for the visible and $825\text{nm} - 2100\text{nm}$ for the nIR/IR region of the spectrum. Both the beam-splitters are mounted on to a DC motorized stage, which allows a precise alignment and switching between them.

The quasi-monochromatic collimated light from the beam-splitters is then focused on to the device under test by an infinity corrected objective (Mitutoyo Plan Apo NIR 100x, NA=0.5). The focused beam diameter d is estimated by

$$\mathrm{d} = 1.22\frac{\lambda}{\mathrm{NA}} \tag{4.5}$$

where λ is the selected wavelength from AOTF and NA is is the numerical aperture of the objective. For a wavelength range of $500\text{nm} - 2100\text{nm}$, the spot diameter ranges from $1.22\mu\text{m} - 2.93\mu\text{m}$. The laser spot was focused and positioned on the sample with the help of a camera from Motic 1SP and the X - Y translation stage - 8MTF - 102LS05 from Standa. The positioning of the laser spot over the fabricated devices is achieved using the stepper motor controller - 8SMC5 – USB from Standa for the spectroscopic measurement or as the start point for the photocurrent 2D mapping.

In order to obtain the 2D mapping, photocurrent is recorded while a focused laser is scanned across the surface of the sample over a defined area with a minimum step size of 375nm. The reflected or back scattered light from the sample during the mapping is detected by a photodetector (PC50-6, First Sensor). The generated current output from the photodetector is recorded with a DC source meter (Keithley 2400) and recorded with respect to the stage position. Both the photocurrent and the backscattered light, are recorded simultaneously to determine the exact position of the photocurrent generation from the device. As PC 50 is a silicon based detector, the detection range is limited from $500\text{nm} - 1200\text{nm}$, and therefore, an InGaS PIN Femto Watt photo-receiver – FWPR-20-IN from Femto was used in the range of $1200\text{nm} - 1700\text{nm}$. For spectroscopic measurements, the laser spot is focused on to the CNT device and the excitation wavelength is scanned across the specific range of the AOTF crystal selected in steps of 5 nm. It is to be noted that selecting a step size less than 5nm would not make a difference owing to the finite spectral resolution of the AOTF crystal. All the measurements were executed and the data were acquired using a custom built python program. During the course of this thesis the stage controller of X-Y translation stage (8MTF-102LS05, Standa) was upgraded, due to the incompatibility of the new controller (8SMC5-USB-B9-2, Standa) with the existing code, the entire stage controller code was rewritten.

The photocurrent signal was measured and recorded using a lock-in amplifier, as the lock-in is capable to detect even very weak signals buried in the noise. The incident light was modulated at the reference sync frequency of the lock-in generated from an external signal generator (Agilent 33210A). The modulation of the light source is achieved by tuning the amplitude of the RF signal that drives the AOTF. Both the photocurrent signal and the reference signal are multiplied by the lock-in and integrated over a specified time generating the DC signal.

Eventually, due to the modulated incident light, an alternating photocurrent is generated in the device. The generated alternating photocurrent is then amplified with a low noise current to voltage amplifier (DLCPA 200, Femto). At the maximum transimpedance gain factor of 10pA/V, the DLCPA generates a low input noise of 0.1297fA. The maximum high gain factor was selected since the photocurrent signals are in the picoampere range. To minimize 1/f noise the light source was modulated at the cutoff frequency at 1.1kHz, tolerating an attenuation of 3dB. By feeding the output of the preamplifier to the SR830 lock-in

amplifier (Stanford Research Systems), the photocurrent signal is multiplied with the reference signal and integrated over time. The SR830 output is a DC signal that is proportional to the alternating photocurrent signal of the same reference frequency. Contribution from any signal that is not at the same frequency as the reference signal is attenuated close to zero.

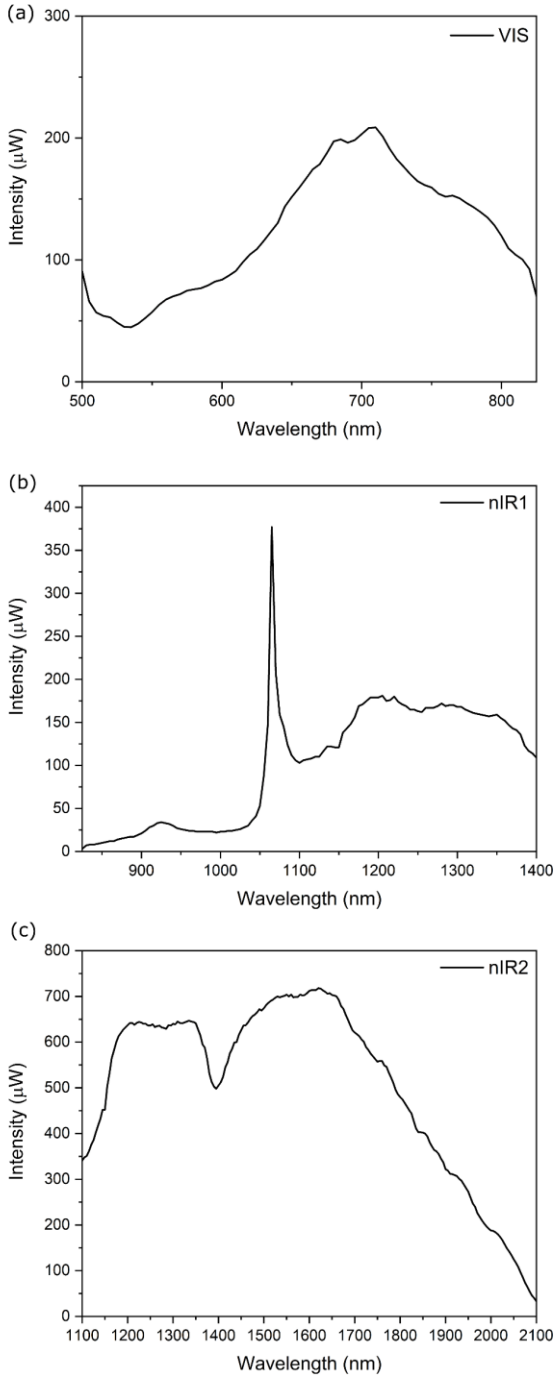

Figure 4.12 : Intensity spectrum of the three AOTF crystals (a) Visible, (b) nIR1 and (c) nIR2

The SR830 generated DC signal can be recorded either as in-phase signal X and out of phase signal Y or as magnitude R and phase θ. The photocurrent measurements reported in this thesis are recorded in two different ways, which are described in the subsequent chapters. The time constant was set to 300ms and the slope at 16dB/Octave determining the acquisition time by measuring over a single wavelength, which in this case 10 times of the time constant.

Figure 4.12 shows the measured intensity using calibrated photodetectors from Ophir (PD300, PD300IR and RM9). The seed laser driving the source is visible at 1064 nm evidently as a sharp peak as shown in Figure 4.12 (b). The AOTF is always operated at the optimum mode as the overdrive mode operates at the maximum RF power and shows non linearity beyond a threshold. In this thesis, all the measurements were obtained at 100%RF in the optimum mode.

5 NIR Photocurrent Spectroscopy on (9,8) Single - Walled Carbon Nanotubes

5.1 Introduction

Semiconducting single walled carbon nanotubes (s-SWCNT), are a material of interest due to their unique electrical, optical properties and their processability. With their narrow band absorption and emission, they have a tremendous potential in the field of optoelectronics,[215] and are promising building blocks in nanoscale light emission as advanced electro-optical transducers[6,26,216] for quantum communication[217] as single photon emitters and as a photoactive material for photovoltaics[28,218,219] and photo-detectors.[220–222] As the technological relevance of the telecommunication band lies between 1260nm -1610nm, probing the selected s-SWCNT with specific chiral index is of great importance, due to diameter and chiral angle dependent optical transition of SWCNTs.[113] The optical absorption coefficient of CNTs at their optical transition is nominally one or two orders of magnitude[223] larger than the conventional semiconductors.[224–226] Hence, their integration on to an optical microcavities would enhance the performance of the photodetection, also, their integration on to a complex photonics circuit can be achieved.[217,227] In order to develop an on chip photodetector that works hand in hand with the waveguide integrated CNT driven light emitters, s-SWCNTs have to be apt photoactive material in the near-infrared (nIR) region. In this chapter, the steps towards creating appropriate conditions for CNTs as an efficient nIR photodetector are discussed. For this reason, we targeted (9, 8) CNTs, as the optical at 1450 nm absorption matches well with the technologically relevant telecom band.

Photocurrent spectroscopy studies were performed on devices fabricated from solution processed few chiral s-SWCNTs dispersed in toluene. The devices were probed in short circuit mode with no external bias applied. The objectives of these measurements were to understand the photocurrent generation mechanism, electrostatic tunability along with the substrate effects on the photocurrent.

5.2 Material & Methods

Device fabrication was carried out as described in Chapter 3 section 3.5. The SWCNT raw material was prepared by Wang et.al using $CoSO_4/SiO_2$ as a catalyst and CO as the carbon source.[228] The catalyst of $200\ \mathrm{mg}$ loaded in a $1\ \mathrm{inch}$ tubular reactor was reduced under $50\mathrm{sccm}\ H_2$ flow under a pressure of $1\ \mathrm{bar}$, while the reactor temperature was increased to 540 °C. Then, the reactor temperature was further increased to 780 °C under Ar flow of $50\ \mathrm{sccm}$ under a pressure of $1\ \mathrm{bar}$. Afterward, the catalyst was exposed to $\mathrm{CO}\ (6\ \mathrm{bar}, 100\ \mathrm{sccm})$ to initiate SWCNT growth for $1\ \mathrm{h}$. Raw SWCNT soot was obtained after dissolving SiO_2 in the catalyst loaded with SWCNTs in $1\mathrm{M}\ \mathrm{NaOH}$ solution. For the SWCNT suspensions, 100 mg of the raw SWCNT soot and 100 mg of the polymer, poly(9,9-di-n-octylfluorenyl-2,7-diyl) –PFO from Sigma-Aldrich, were mixed in 100 mL of toluene and subjected to a sonication treatment for 2 h

using a titanium sonotrode from Bandelin. During sonication, the suspension was placed in a water-circulation bath to aid cooling. After sonication, the suspension was centrifuged for 2 h at 20 000g.

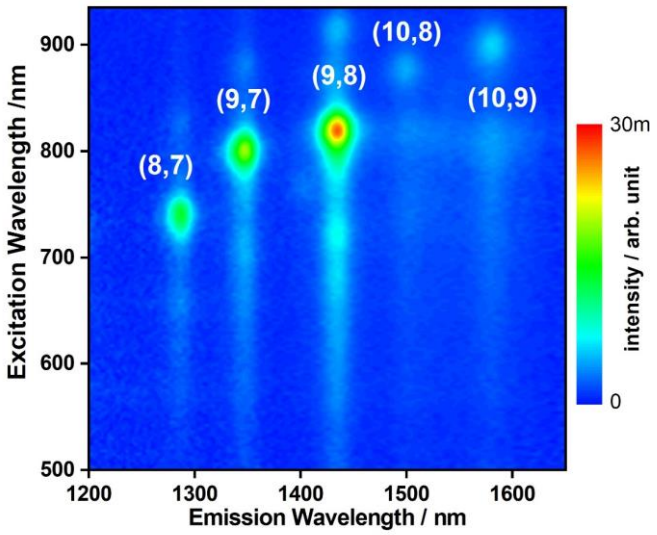

Figure 5.1: Photoluminescence excitation Map of the toluene dispersed sample containing mainly (9,8) CNTs

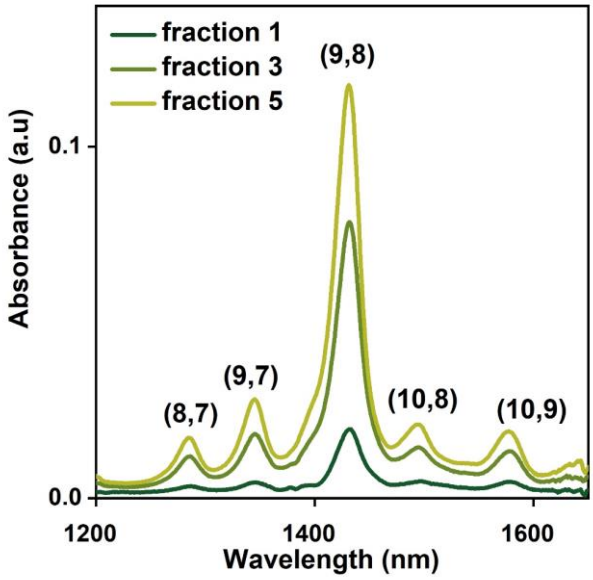

Figure 5.2: UV-Vis-nIR absorption spectra of toluene dispersed polymer wrapped sample containing mainly (9,8) CNTs

To generate the starting suspensions for SEC separation (see Chapter 4), the supernatant was concentrated to ~ 10 mL by evaporating ~ 90 mL of toluene. Semi-preparative size-exclusion chromatography was performed using Toyopearl HW-75 resin from Tosoh Bioscience filled into a glass column having 16 mm inner diameter and 20 cm length. For the separation, 5 mL of SWCNT starting suspension was

applied to the top of the column, and toluene was used as the eluent run by gravity flow at a rate of ~ $2\mathrm{mL/min}$. Fractions were collected in $3-4$ mL portions. First fractions collected, consists nanotubes of length 1 -2 µm. Photoluminescence maps of SEC purified suspensions were recorded using a Bruker FTIR Spectrometer IFS66 in 3nm steps of excitation from $500-950\mathrm{nm}$ and emission in the range of $900-1700\mathrm{nm}$ detected with a liquid nitrogen cooled Ge photodiode. UV-Vis-NIR absorption spectra were recorded on the SEC sorted samples using Varian Cary 500 spectrophotometer.

The toluene based suspension contains few-chiral semiconducting nanotubes of diameters up to $1.2\mathrm{nm}$, with higher concentration of (9,8) tubes. Individual tubes were then simultaneously deposited on multiple device structures by DC dielectrophoresis probing the source and the drain electrodes as described in the previous chapters, on device structures prepared with e-beam lithography as in section 3.5. The stock suspensions were diluted up to a factor of 10 in order to deposit few tubes between the electrodes. A DC bias of $2\mathrm{V}-5\ \mathrm{V}$ was applied for the silicon substrates with $300\mathrm{nm}\ /\ 800\mathrm{nm}$ oxide and $0.1\ \mathrm{V}\ -\ 1\ \mathrm{V}$ for sapphire substrates. To confirm the deposition of CNTs, transport characteristics of the devices were measured at ambient conditions in a probe station with TRIAX probes using an Agilent 4155C semiconductor parameter analyzer before and after annealing (see section 3.5). The samples were then mounted on to a chip carrier and were wire bonded for the photocurrent measurements (see section 3.5.3).

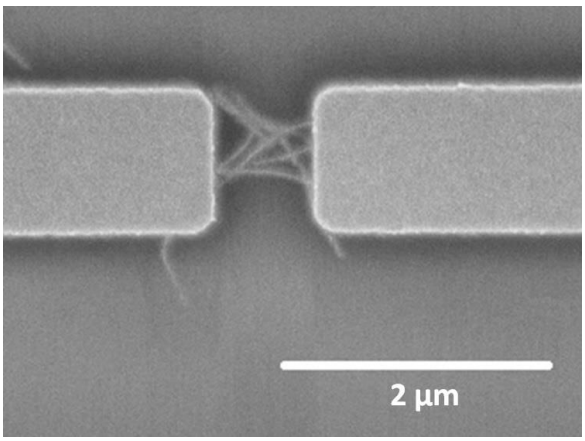

Figure 5.3: SEM micrograph polymer (9,8) sorted tubes deposited on a device with 800nm gap size after DC dielectrophoresis (DC-DEP)

5.3 Photocurrent Spectroscopy

Photocurrent measurements were carried out using a DLCPA 200 low noise current to voltage pre-amplifier from Femto in combination with a SRS 380 Lock-in amplifier to record magnitude R and phase θ of the photocurrent modulated at $1.099\mathrm{kHz}$ & $1.213\mathrm{kHz}$ by the AOTF (See chapter 4.4). The modulation was kept at $1.213\mathrm{kHz}$ for all the measurements in this chapter and the preamplifier was set to 10x unless noted other otherwise. A high modulation frequency were used to get a reduced noise averaged photocurrent signal obtained in picoampere range. The data were collected using a custom python program. All the measurements reported in this chapter were obtained in short circuit configuration, such that no external bias were applied, and the photocurrent generated by the tube was measured between the source and drain electrodes. The drain and the gate electrodes were end terminated with a 50Ω terminator. The incident light generates thermal carriers as described in section 2.8. Excitons generated in the nanotubes

on absorbing the incident light (see section 2.4.3), undergo separation by the built-in electric field from the Schottky barrier formed at the metal/nanotube junction or interface generating a photocurrent.

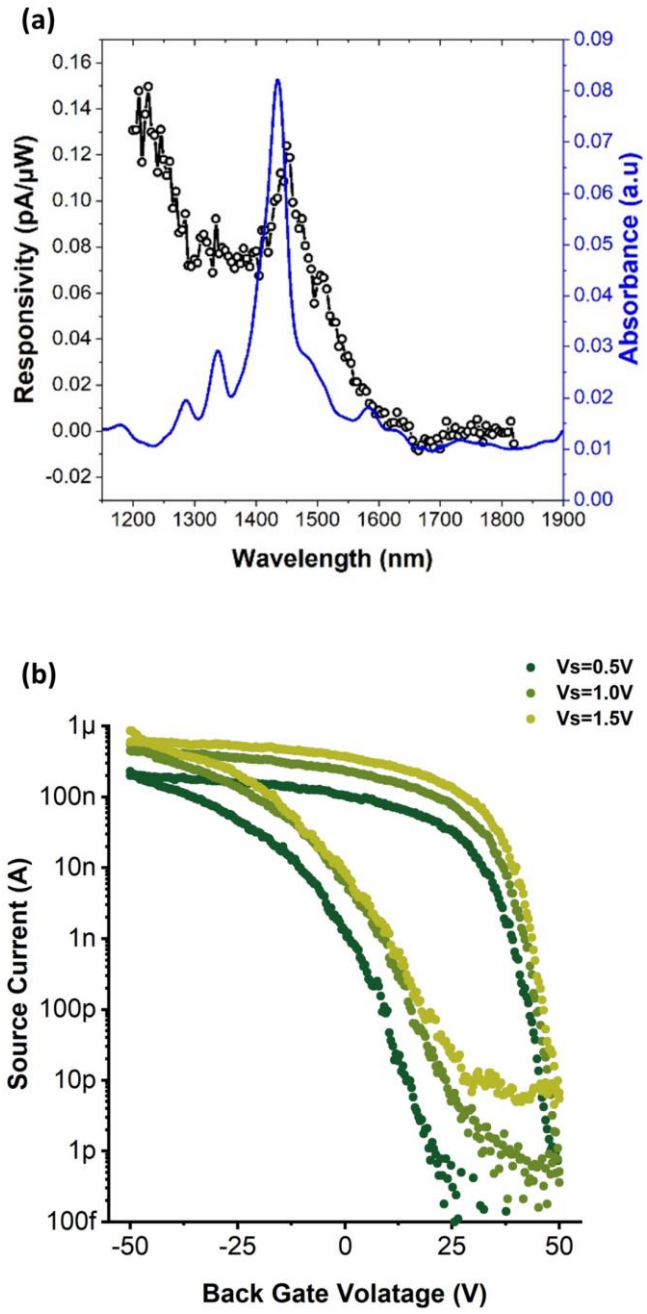

Figure 5.4: (a) Photocurrent spectrum of a PFO sorted (9,8) device on 300nm SiO2/Si stack in comparison with the absorption spectrum of the corresponding suspension. (b) Transconductance measurements of the corresponding device at three different source drain bias or voltage

The photocurrent spectra were recorded in steps of 5nm steps on devices fabricated on standard silicon substrates of two different thermal oxide thicknesses, to determine the influence of the substrates on the generated photocurrent. The substrates were Boron doped silicon wafers with resistivity less than $0.005\Omega\mathrm{cm}$, from Active Business Company- covered with $300\mathrm{nm}$ and $800\mathrm{nm}$ of thermal silicon oxide.

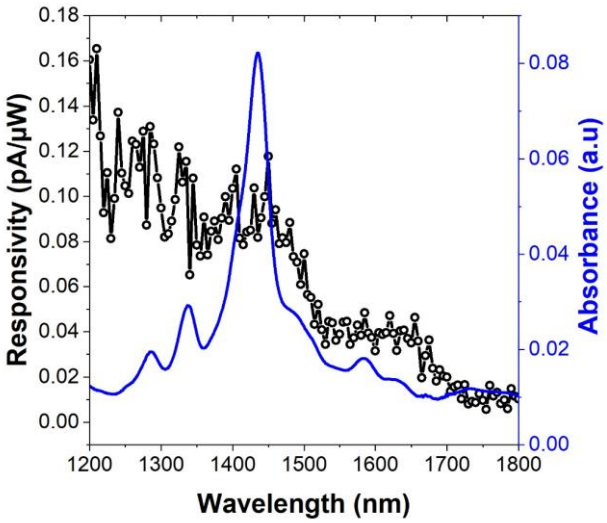

Figure 5.5: Photocurrent spectrum of a PFO sorted (9,8) device on 800nm SiO_2/Si stack in comparison with the absorption spectrum in toluene suspension.

The photocurrent spectrum obtained from a PFO sorted (9,8) SWCNTs is shown in comparison with the nIR absorption spectrum in Figure 5.4 (a) along with the trans-conductance measurement of the silicon / silicon-dioxide (300nm) substrate with incident light as shown in Figure 5.4(b). The fabricated devices have a channel length of 800nm. The measured photocurrent spectra are plotted as responsivity. The Responsivity R is calculated as $\mathrm{R} = \mathrm{I_{PC}}/\mathrm{I_L}(\lambda)$, where $\mathrm{I_{PC}}$ is the photocurrent generated from the device and $\mathrm{I_L}(\lambda)$ is the wavelength dependent source intensity (see Figure 4.10 in section 4.4).

For each SWCNT integrated on to a device, a photocurrent peak from nanotube alone is expected. However, a linear background of unknown origin is observed (1100 nm-1325 nm) along with the expected single peak from the tube at 1465 nm. This linear background that is observed can be correlated to the photocurrent generated from the underlying silicon in the substrate due to photogating effect. From the X-ray photoelectron spectroscopy (XPS) measurements it is known that close to the p-Si/SiO_2 surface, a significant downward bending of the bands of -0.4 eV is observed.[229,230] This is due to the process of accumulation minority charge carriers at p-Si/SiO_2 interface from the silicon side under illumination is called photogating effect, making the oxide side of the interface positively charged. This band-bending acts as a trap to produce a significant photovoltage.[231,232]

The peak at 1465 nm of the photocurrent spectra is assigned to the S11 transition of the (9, 8) nanotubes by correlating with the absorption spectra (blue) (see Figure 5.4 (a)). Such correlation of the photocurrent spectra associated to the absorption spectra have been reported in the literature.[66,198,233] Also, the variation in the linewidth and central peak wavelength is due to the dielectric environment surrounding the nanotube. For our measurements reported in this thesis, the photocurrent peaks observed are slightly

broader and red shifted in comparison to the absorption spectra. We have assigned the peaks in the photocurrent spectra to the (n, m) species present in the dispersion. Which is challenging since the changes in the dielectric environment (toluene versus substrate) causes red or blue shifts in the transition energy depending on whether a CNT belongs to mod-1 or mod-2 family.[234]Also, a similar photocurrent response was observed for several devices from two different 300 nm SiO_2/ Si stack substrates, but their data is not presented here to avoid deviation from focus.

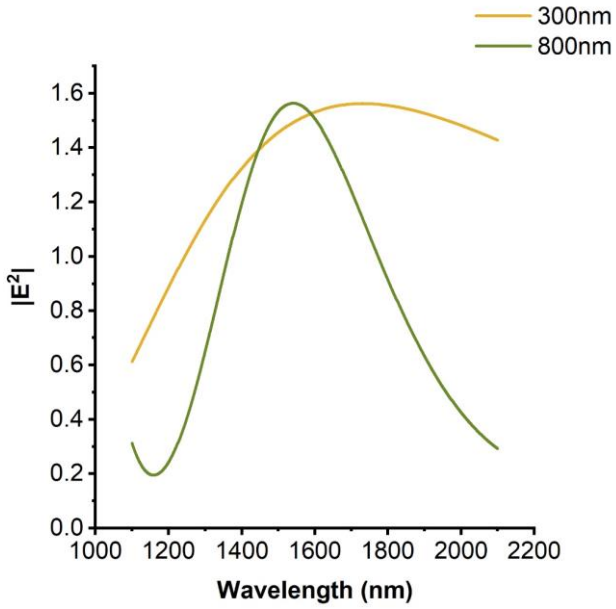

Figure 5.6: Simulated electric field on the on the surface of SiO_2/Si stack with respect to the incident beam for 300nm and 800nm oxide thickness with respect to the wavelength

To verify if the linear background is from the substrate (silicon), photocurrent spectrum measurements were repeated with 800nm (thicker oxide) thermally grown oxide wafer and sapphire wafers. The photocurrent spectrum of PFO wrapped (9,8) integrated devices in silicon with 800nm thick oxide wafer is shown in Figure 5.5 in comparison with absorption spectrum. It is evident that the linear background from the substrate is present irrespective to the change in the oxide thickness. Also, we do not see a distinct peak from the (9, 8) nanotube S11 transition as correlated in Figure 5.4(a).

To understand the light intensity distribution with respect to the wavelength on the surface of the substrate, electric field simulations were also calculated using transfer matrix method. The electric fields on oxide surface for different wavelengths are shown for two different oxide thicknesses for the layered substrate stacks with respect to perpendicular incident light in Figure 5.6. The variation in the light intensity with respect to wavelength is caused due to multiple reflections from the interface of different layers of the substrate. The electric field intensity is favorable with maximum light intensity with respect to the S_{11} transition of (9, 8) nanotube at 1450nm.

Similarly, the photocurrent measurements were carried out on sapphire wafers, which are transparent in the target wavelength range (1100 nm-2100 nm). The photocurrent spectroscopy measurements were performed on devices with same geometry. The nanotubes were integrated by fine-tuning DC DEP, for sapphire substrate. The photocurrent spectrum of PFO wrapped (9,8) nanotubes integrated devices on sapphire substrate is shown in Figure 5.7 along with the absorption spectra of the nanotubes in toluene

suspension. A single peak with a shoulder is observed corresponding to the S11 transition of (9,8) at 1455nm and shoulder on the left from S11 transition of (9,7) at 1390nm. Compared to the photocurrent spectrum obtained on the SiO_2/Si stacks in (Figure 5.4(a) & Figure 5.5), we do not see any linear background photocurrent in the photocurrent spectra. This confirms our assumption of linear photocurrent background arising from the silicon. On contrary, Sapphire yields photocurrent response only from the tubes, making sapphire a preferable substrate material for photocurrent measurements.

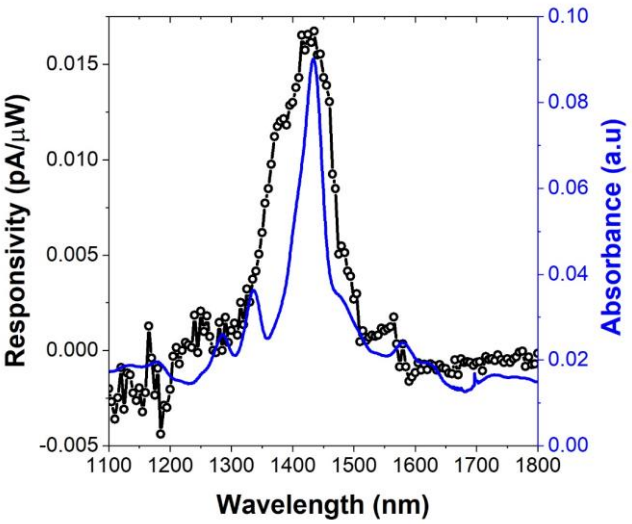

Figure 5.7: Photocurrent spectrum of a PFO sorted (9,8) device on sapphire substrate in comparison with the absorption spectrum in toluene suspension.

5.4 Photocurrent Spectroscopy of Carbon Nanotube Split Gate Devices

As sapphire is an insulating substrate, a conducting gate is desirable to tune the photocurrent spectra. The generation of photocurrent is entirely dependent on the Schottky barriers[235–237] formed between the metal and the nanotubes splitting the generated excitons. For a device we have two such junctions which generate photocurrents of opposite sign. Due to fabrication imprecision (electrode roughness, nanotube /electrode overlap) and by non-symmetric illumination we nevertheless collect photocurrent from the devices. In order to improve the efficiency of photocurrent generation, a split gate was fabricated with a gap of 50nm to create a pn-junction along the tubes by electrostatic doping, which has been proven to be 100 times more efficient.[238] Such a junction would create the necessary field to split the excitons, which increases the conversion of excitons to photocurrent.

A schematic of a device on sapphire and SEM micrograph are shown in Figure 5.8. The structure was formed by a 3-step lithography process. First, the split gates are fabricated with $5\mathrm{nm}/50\mathrm{nm}$ – Ti/Al using an ultra – high vacuum (UHV)molecular beam epitaxy (MBE) to obtain smooth gate electrodes. Then a $50\mathrm{nm}$ aluminum oxide (Atomic layer deposition –ALD) was grown on top as dielectric spacer between the back gate and the source-drain electrodes. In the final step $5\mathrm{nm}/70\mathrm{nm}$ –Cr/Pd source-drain electrodes

were sputtered. The SEM micrograph shows the fabricated structure. The channel length between the source and drain is 800nm.

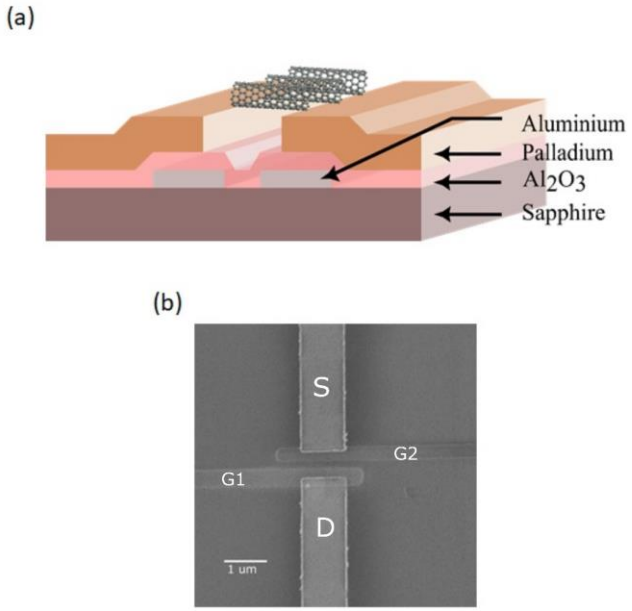

Figure 5.8: (a) Split gate device schematic (b) Top view SEM micrograph of a split gate device on sapphire substrates

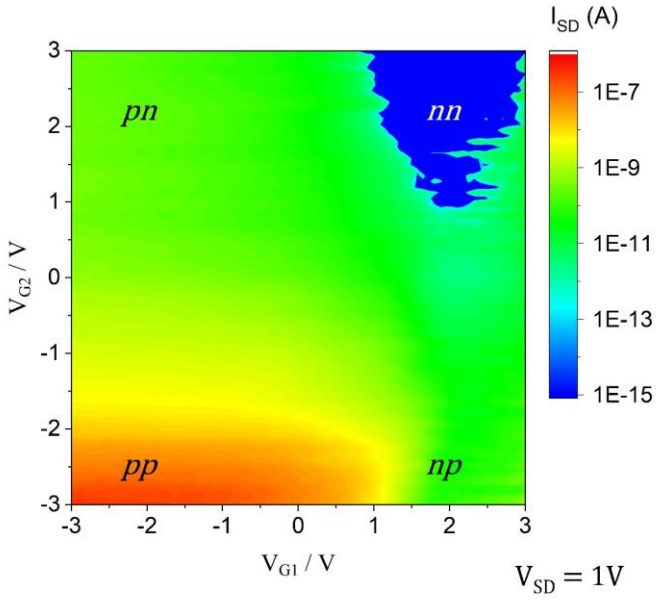

Figure 5.9: Transconductance map of dual gated device on sapphire substrates measured at a constant source drain voltage of 1V and the gates tuned at steps of 750mV

The devices were then subjected to nanotube dielectrophoresis (DC-DEP at 0.5V, 5mins) and subsequently annealed (200°C, 4 hours). The devices were then wire bonded and their transconductance map were measured to understand the device characteristics. Figure 5.9 shows the transconductance map of the device under test. At constant source drain voltage of $V_{SD} = 500\text{mV}$, the gate potentials $V_{G1}$and V_{G2} were tuned with a step size of 750mV. It is clearly seen that the device shows a higher conductance in the pp region than in the nn region, similar to the transconductance curve of the single gate (9, 8) device in Figure 5.4. However, we do not see any sign of a pn or np junction formation on the pp or np region in the left upper quadrant or the right lower quadrant of the transconductance map. In order to form a pn or np junction across the nanotube channel by electrostatic doping, higher gate voltages would have been favorable. But the gate bias values were limited to $\pm 3\text{V}$ to avoid the breakdown of the dielectric ($50\text{nm} - Al_2O_3$).

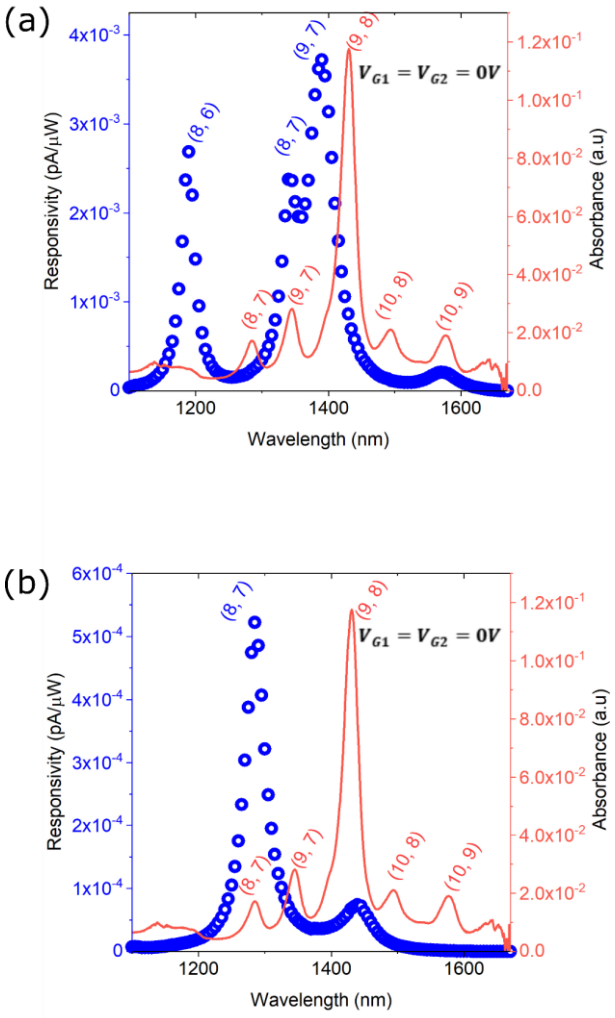

Figure 5.10: Photocurrent spectra plotted in comparison with UV-Vis –nIR absorbance spectra in toluene from two devices on the same sapphire chip.

The photocurrent generated from nanotubes in a device could be tailored by applying a gate bias. In presence of such a gate bias, the Schottky barrier is tuned to favor the transport of holes or electrons across the tube channel. The devices demonstrate a distinctive gate dependent increase or decrease in photocurrent generation due to the effect of the electric field on the Schottky barrier.[134] The influence of electrostatic field on a nanotube is diameter dependent. Electrostatically, larger diameter tubes are influenced first for a given gate bias. On a multi-chiral nanotube integrated device as presented in this study (Figure 5.2), the electrostatic gating plays a major role on relative (n, m) specific contribution to the photocurrent.

Figure 5.10 shows the open circuit photocurrent for two split gate devices on the same sapphire substrate chip at zero gate bias ($\mathrm{V_{G1}} = \mathrm{V_{G2}} = 0\mathrm{V}$). On the same chip, the photocurrent spectra of the two devices are not identical although fabricated on the same chip and same nanotube dispersion. We have assigned the peaks in the photocurrent spectra to the (n, m) species present in the dispersion. Which is challenging as mentioned earlier, since the changes in the dielectric environment (toluene versus sapphire) causes red or blue shifts in the transition energy depending on whether a CNT belongs to mod-1 or mod-2 family, as stated above.[234] Figure 5.10 (a) shows photocurrent contribution from (8, 7) and (9, 8) where as in Figure 5.10 (b), a contribution from (8, 6) and (9, 7) is observed. As there is no control over the chirality of the tube being deposited, the relative contribution of photocurrent from different tubes differs for every device.

As transconductance shows no evidence of pn / np junction formation. In order to examine if pn junction appears in photocurrent measurements, photocurrent was measured as a function of the two gate voltages $\mathrm{V_{G1}}$ and $\mathrm{V_{G2}}$ to find the exact condition for forming a pn junction. The devices were subjected to a different gate potential combination over a range of $\pm 3\ \mathrm{V}$ with steps of $1\ \mathrm{V}$. Also, as exact opposite polarities on the gates might not generate the right conditions for forming a pn junction, due to fabrication dissimilarities like nanotube placement, variation in dielectric thickness etc. The Figure 5.11 (a) shows photocurrent responsivity map of a device illuminated with a wavelength of 1450nm (S11 transition of (9,8) tubes) with respect to the gate potentials $V_{\mathrm{G1}}$and V_{G2}varied at $1\ \mathrm{V}$ step. Figure 5.11 (b) shows the photocurrent spectrum of the same device at $\mathrm{V_{G1}} = -2\mathrm{V}, \mathrm{V_{G2}} = -3\mathrm{V}$, which is also marked with a black square on the photocurrent responsivity map.

The photocurrent spectrum shows a maximum close to the S_{11} transition of the (9,8) tubes with additional contribution from other (n, m) species in the solution, unlike the photocurrent spectrum shown in Figure 5.10(b) is of the same device, it is clear that the photocurrent contributions from individual tube types can be tuned by the applied gate potentials. Also, the photocurrent responsivity map shows, that the highest photo-response is achieved in the pp region not in the pn or np region of the map, which implies that the photocurrent generated at the pn junction is negligible compared to the photocurrent generated by the Schottky barrier, dominating in the pp region.

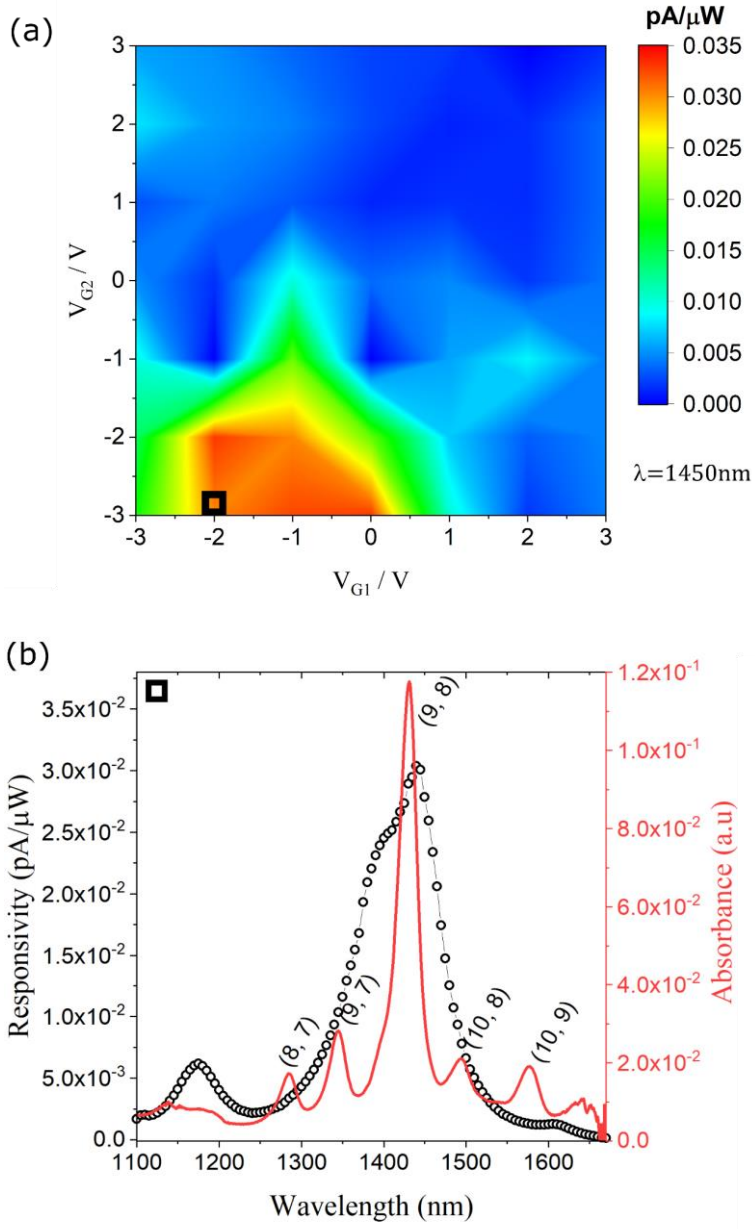

Figure 5.11: (a) Photocurrent responsivity map excited at 1450 nm ((9,8) S11 transition) (b) Photocurrent spectrum measured at $V_{G1} = -2V$ and $V_{G2} = -3V$

For further analysis, the device was subjected to a constant current mode using Agilent semiconductor parameter analyzer 4155C. The measurement setup maintains a constant current across the entire dual gate map (Figure 5.12) irrespective of changes in device resistance. This avoids the exponential suppression of the current as observed in the transconductance map (Figure 5.9). Figure 5.12 shows the constant current map measured at 1nA source drain current, with the probed voltage converted to resistance. The resistance map shows the least resistance in the pp region and the highest resistance in the nn region, the resistance in the pn region is exactly half the value of the nn region.

Figure 5.4 (b) shows that (9, 8)-pd devices are low resistive for hole conduction (p-region) and high resistive for electron conduction (n-region), a consequence of a low Schottky barrier for holes and a high Schottky barrier for electrons. For the resistance map in Figure 5.12, this means that in the pp region, the two low resistive junctions limit the current, whereas in the nn region the two high resistive junction limit the current. In the pn and np region one high and one low resistive junctions are active which explains why the resistance on the pn and np is half of the resistance in the nn region.

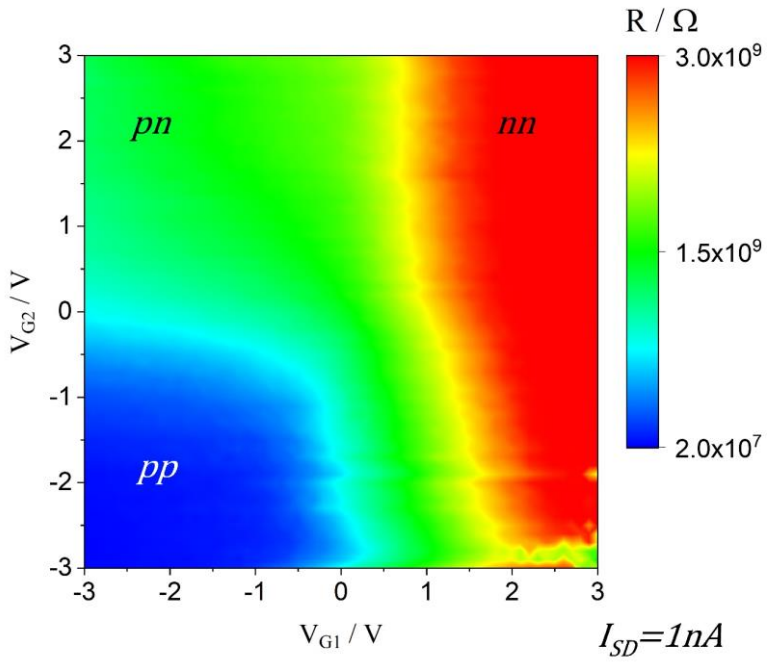

Figure 5.12: Constant current map recorded at $1nA$ against the gate bias voltages varied in steps of $750mV$. The voltage color scale is converted to a resistance scale for a better understanding.

Similar results were observed for four other devices, implying that the pn junction formed by the electrostatic doping from the gates is dominated by the competing Schottky barriers. Hence, the photocurrent collected from the device is generated at the Schottky barriers and not from the pn junction. Nonetheless, even if the pn junction generated a photocurrent it could not be collected across the highly resistive Schottky junctions. However, the relative contribution of the (n, m) specific photocurrent could be controlled with the local split gates – constituting a tunable photo-detectors in the near infrared regime of the spectrum. Figure 5.13 shows relative (n,m) specific contributions to the photocurrent for various combinations of gate voltages V_{G1} and V_{G2}. Although, on chip integrated s-SWCNTs as photodetectors have been reported,[103,134,239] but with few chiral (n, m) resolved photocurrent spectroscopy in telecommunication band has not been reported. In the past, M.Engel et al.[198] reported chirality resolved photocurrent for smaller diameter tubes in the wavelength range of 500 nm to 900 nm. And recently, McCulley et al.[240] reported an efficient method for photocurrent generation in larger diameter SWCNTs with optical absorption beyond the telecom band, with S_{22} in the telecom band. But all the measurements reported were measured under a source drain bias, unlike photocurrent measurements in this study

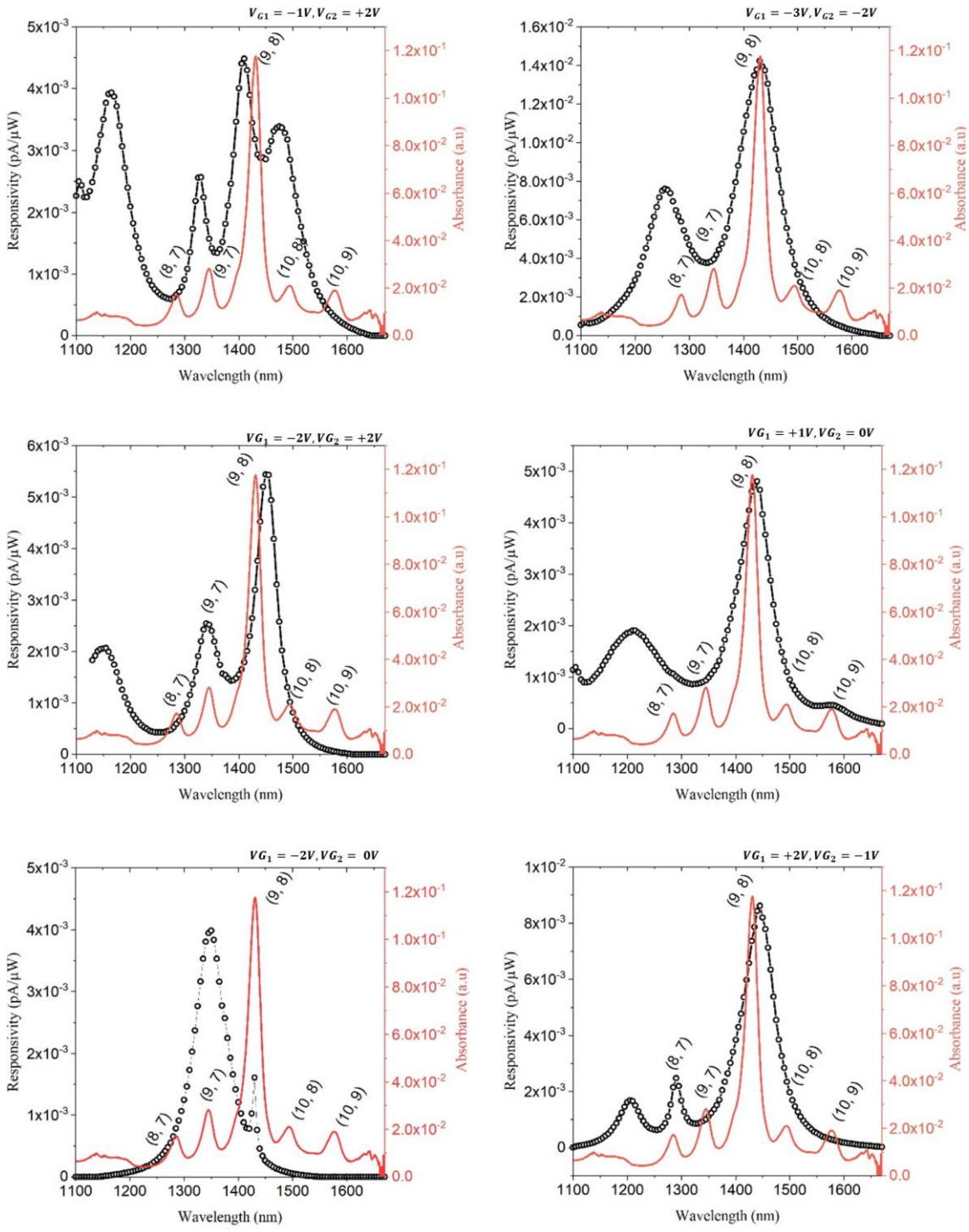

Figure 5.13: Relative (n,m) specific photocurrent contributions for a specific combination of gate bias applied across VG_1 and VG_2.

5.5 Conclusion

In this chapter, photocurrent measurements from solution processed CNTs integrated into transistor geometry were discussed. The background contribution due to Silicon substrates from surface photo voltage were unavoidable, thus moving to a sapphire substrate yields photocurrent responses from the nanotubes only. The resulting photocurrent spectrum resembles the absorption spectrum of the nanotube dispersion and could be used as a qualitative method to determine the different (n, m) species present in the fabricated device.

The transistor like geometry with the local split gates enables the devices to tune the relative contribution of (n, m) specific photocurrent on applying specific combinations of the gate voltages there by constituting potentially, a tunable photo-detector in the nIR regime of the spectrum. Measuring the constant current map eliminates the exponential suppression of the current observed in the trans-conductance map, giving a clarity on the competing electrostatically formed pn junction and the Schottky barrier. It is clear that the Schottky barriers dominate the electrostatically formed pn-junction. Ultimately, the exciton dissociation originates from the electric field provided by the Schottky barrier across the nanotube metal junctions and not from the pn-junction. Schottky barrier could be overcome by increasing the contact length at the nanotube and metal interface, which requires integration of longer nanotubes. Also, a better dielectric film quality between the gates and the electrodes would provide a larger window for applied gate potential assisting in generation of a stronger pn-junction along the nanotube channel.

6 Photocurrent Study of Carbon Nanotube Silicon junction

6.1 Introduction

Single walled carbon nanotubes (SWCNTs) have been integrated into optical waveguides and were operated as on chip electro-optical transducers. While carbon nanotubes have already proven to be promising light emitting single photon sources for quantum communication, they are also active materials in photovoltaics and photodetectors.[26,28,216–222] Also, as discussed in chapter 5, nanotubes can also serve as a complementary optoelectronic transducer over a specific wavelength range, can harvest light across metal/CNT junction. A challenge for using CNT as an optoelectronic transducer though, is the small geometrical cross-section for light absorption, which would be difficult to operate at single tube level. Hence, on integrating them on to a photonic micro cavity would enhance the photo-detection by orders of magnitude due to increase in light matter interaction,[223] and also monolithic integration of nanotubes onto complex Nano photonic structure has been achieved.[217,227] Photonic components on SOI are preferred for operation in the optical communication band due to its low loss and high refractive index, along with the compatibility with silicon technology.[241] However, to harvest waveguide coupled light with a nanotube efficiently, exciton splitting should occur at the silicon waveguide / nanotube junction. So far CNT/Si junctions have been studied in solar cells[242,243] and for photodetection in thin films.[232,244,245] However, chirality resolved photocurrent contribution of CNT in contact with p-Si was not reported. Responsivity of photodetectors were recently measured by Salvato et al.[245], based on n-doped silicon in contact with CNT film in the wavelength range of 300-1000 nm and An et al.[244] measured with CNTs and p-doped silicon substrate showing similar results. Also, Sczgelski et al.[232] used larger diameter CNTs and observed positive and negative photocurrent contribution from silicon and CNT, respectively.

We have performed, spatial and spectral photocurrent measurements on multi-chiral CNTs absorbing in the telecom band, integrated on to a silicon waveguide with silicon electrodes, forming a nanotube silicon junction for the first time. The results show that the small diameter nanotubes such as (7, 5) and (7, 6) can produce photocurrents when in contact with p-Si, whereas larger diameters nanotubes (8, 7), (9, 7) and (9, 8) do not due to unfavorable HOMO and LUMO positions.[66] However, photocurrent measurements were further continued on monochiral (6, 5) toluene based s-SWCNT/p-silicon junctions, to gain better understanding on photocurrent generation mechanism. Surprisingly, we observed a similar photocurrent spectral response as reported earlier despite using a different monochiral suspension. In this chapter, our first published results and new unpublished results are discussed in detail.

6.2 Material & Methods

Device fabrication was carried out as described in Chapter 3 section 3.5. The SWCNT suspensions, 100 mg of the raw SWCNT soot (HiPCO material and CoMoCAT- Sigma Aldrich) and 100 mg of the polymer, poly(9,9-di-n-octylfluorenyl-2,7-diyl) –PFO from Sigma-Aldrich, were mixed in 100 mL of toluene and subjected to a sonication treatment for 2 h using a titanium sonotrode from Bandelin. During sonication, the

suspension was placed in a water-circulation bath to aid cooling. After sonication, the suspension was centrifuged for 2 h at 20 000g. For the starting suspensions, photoluminesence maps and absorption spectra were obtained as mentioned in section 5.1.

Two dispersions, one containing several chirality (7, 5), (7, 6), (8, 7), (9, 7), (9, 8) and one containing only (6, 5) CNTs were used. From each dispersion, CNT were simultaneously deposited on multiple device structures by DC dielectrophoresis probing the source and the drain electrodes as described in the previous chapters. A 250 nm p-Si / 3 µm SiO_2 / p-Si SOI substrate (total thickness: 675 µm) and a 600 nm p-Si / 460 µm sapphire SOS substrates from University wafer was employed as substrates. It was cleaned with acetone and isopropanol (IPA), blown dry with nitrogen, and spin-coated with poly (methyl methacrylate) (PMMA). Electrodes were then patterned by using aluminum as an etch mask (20 nm for SOI and 80 nm for SOS) via e-beam lithography and metal evaporation. Subsequently, reactive ion etching was performed with a mixture of CHF_3 (20 sccm), SF_6 (5 sccm), and O_2 (5 sccm), forming the source and drain electrodes underneath the aluminum etch mask. The distance between the source–drain electrodes was kept at 800nm. The etching rate was determined by reflectance measurements using a thin film analyzer F20 from Filmetrics. Finally, the aluminum layer was removed by exposure to 3% metal ion free tetramethylammonium hydroxide (MIF 726) for about 50s. Figure 6.1 (a) shows the schematics of the fabricated SOI substrate along with the SEM micrograph of the 12 device layout

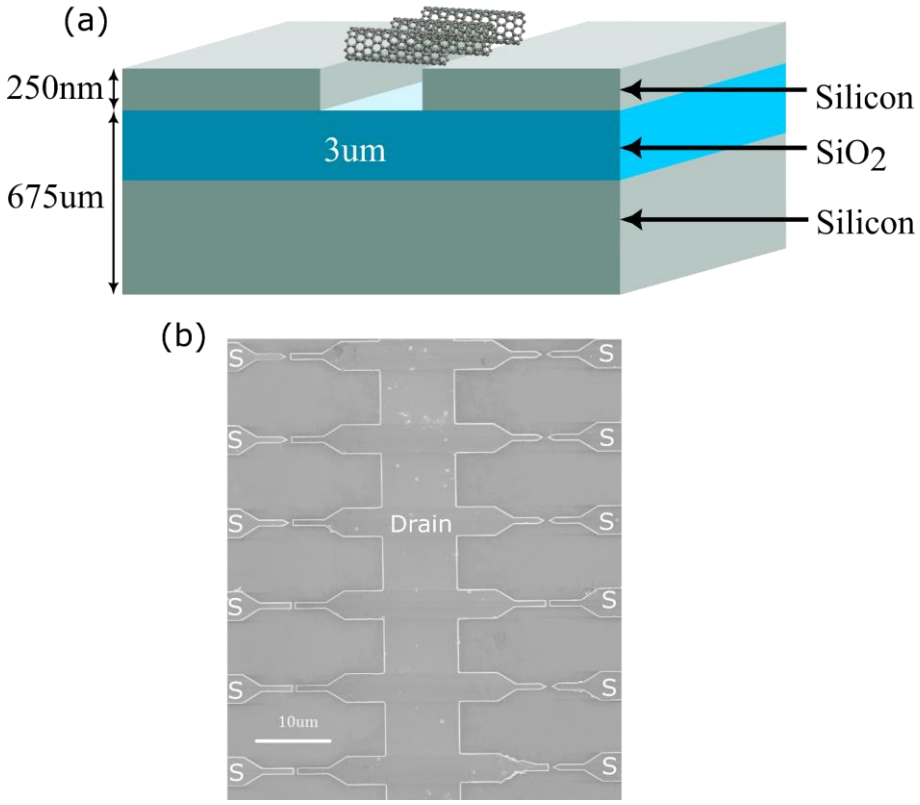

Figure 6.1: (a) Schematic of one device on a SOI substrate (b) SEM micrograph of 12 devices on the SOI substrate (S denotes source electrodes).

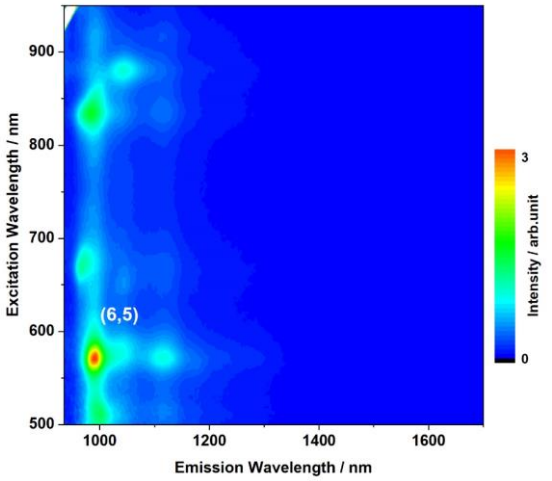

Figure 6.2: Photoluminesence excitation map of the toluene dispersed sample containing mainly (6, 5) CNTs

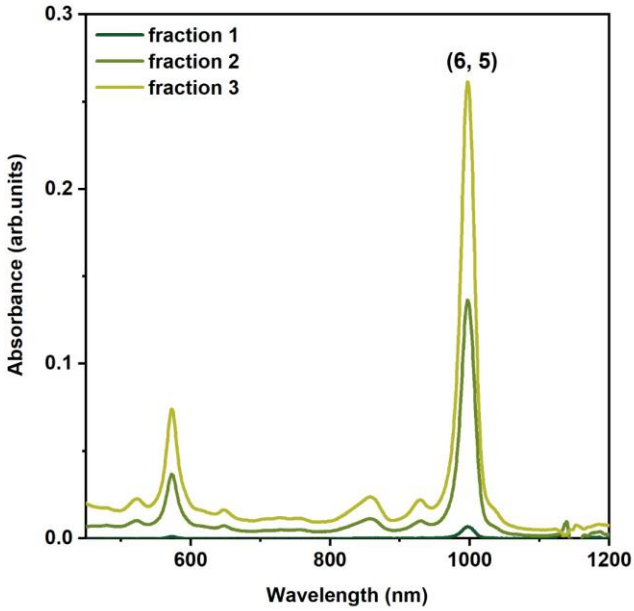

Figure 6.3: UV-Vis-nIR absoption spectra of toluene dispersed polymer wrapped monochiral (6, 5) CNTs

The toluene based monochiral suspensions were diluted up to a factor of 10 in order to deposit 5-10 tubes (0.16 CNTs/µm^3), with a DC bias of $2\text{V} - 6\text{ V}$. Figure 6.4 shows the typical SEM micrograph of polymer

sorted monochiral (6, 5) CNTs bridging the source and drain electrode of the 800nm gap on the SOI substrate. To confirm the deposition of CNTs, transport characteristics of the devices were measured at ambient conditions in a probe station with TRIAX probes using an Agilent 4155C semiconductor parameter analyzer before and after annealing (see section 3.5). The samples were then mounted on to a chip carrier and were wire bonded for the photocurrent measurements (see section 3.5.3).

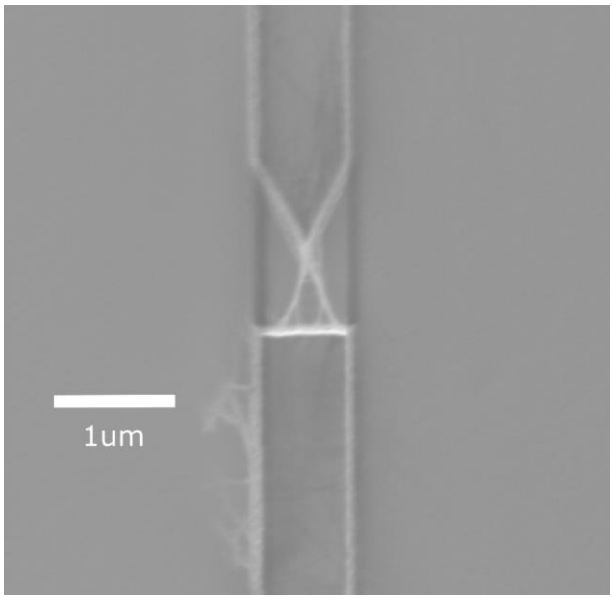

Figure 6.4: SEM micrograph polymer sorted mono-chiral (6, 5) integrated on to a device structure after DC dielectrophoresis (DC-DEP).

6.3 Photocurrent Spectroscopy

Photocurrent measurements were carried out using a DCPLA 200 low noise current to voltage preamplifier(Femto), in combination with SRS 380 lock-in amplifier to record magnitude R and phase θ of the photocurrent modulated at 1.099 kHz as described in Chapter 5. The photocurrent spectra were recorded in steps of 5 nm on devices, fabricated on silicon on insulator (SOI) substrates and silicon on sapphire substrates (SOS), to determine the photocurrent generation mechanism on s-SWCNT/p-Si junction. To evaluate the photocurrent generation in the entire telecom band, spectrally well separated optical transitions in the nIR are required. For that purpose, the few chirality dispersion comprising of (7, 5), (7, 6), (8, 5), (8, 6), (8, 7), (9, 7) and (10, 9) CNTs have been prepared and integrated into the devices on SOI substrate with waveguide structure (inset: Figure 6.5).

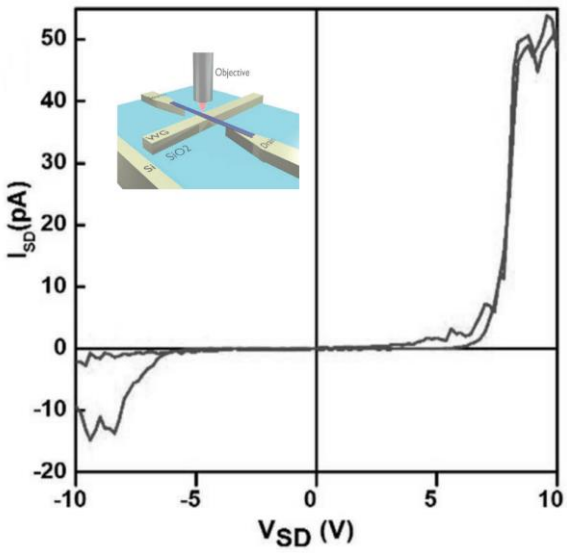

Figure 6.5: IV characteristics of waveguide integrated nanotube p-Silicon junction. Inset: Schematic of the waveguide device geometry on SOI [reproduced from 66].

The IV characteristics of Si-CNT-CNT-Si junctions in series is shown in Figure 6.5. The curve represents diode like heterojunctions, the turn on voltages in both the positive and the negative directions are determined by the breakdown voltages of the junction operated in reverse bias. The measurements reported in this chapter are obtained in short circuit configuration, with no external bias was applied, and the photocurrent generated was measured across the tube along the source and drain electrodes.

The nIR photocurrent spectrum of the few-chiral suspension on the SOI substrate is shown in Figure 6.6 (a). The responsivity was calculated as described in chapter 5. The photocurrent is plotted in comparison with the absorption spectrum and absorption coefficient of silicon. The spectrum shows a large positive photocurrent in the shorter wavelength region, which weakens non monotonically from 825nm to 1020nm. The photocurrent then switches sign, indicating the change in direction from 1020nm to 1200nm, and no photocurrent beyond 1200nm. The negative photocurrent between 1020nm and 1200nm corresponds very well with the S_{11} transitions of $(7, 5)$ CNT at 1045nm and $(7, 6)$ CNT at 1125nm. However, contributions from the larger diameter tubes are not observed, though (8, 7) (9, 7) and (9, 8) are present in the dispersion. On the contrary, a positive photocurrent is observed at shorter wavelengths, where there are no CNTs present to contribute to it. Evidently, it is the silicon that is photoactive in the shorter wavelength region, and on comparing the absorption coefficient of silicon, the wavelength dependence is very similar. The modulation in the positive photocurrent response is caused due to the interference effect in the $Si/SiO_2/Si$ stack, is understood from the reflectivity measurements (Figure 6.6 (b)). From the light field intensity simulations in such a stack, we can understand if the reflectance is at a minimum, then the light field intensity at the surface (location of the junction) has a maximum. Hence, the photocurrent maximum is expected where the reflectance has a minimum and vice versa. This explains the non-monotonic decrease of the positive photocurrent with increasing wavelength.

The positive, negative and the diameter dependent photocurrent are understood by considering the band structure of the p-doped silicon in contact with the CNT sidewall in presence of a natural oxide. The energy of the p-doped silicon conduction band edge is at $\mathrm{E_C} = -4.15\ \mathrm{eV}$ and of the valence band edge at $\mathrm{E_V} = -5.27\ \mathrm{eV}$ (bandgap E_G = 1.12 eV); the Fermi energy is at E_F = −4.98 eV. The values were derived from the

resistivity, $\rho = 18 \pm 4\,\Omega\,\mathrm{cm}$.[246] From X-ray photoelectron spectroscopy (XPS) measurements, it is known that close to the p-Si/SiO_2 surface, a significant downward bending of the bands of about -0.4 eV is present.[229,230] Such a bending is caused due to the charge build up on the oxide side of the interface causing electron injection to the silicon. Although the band bending would be compensated by the excessive electron hole pair generation due to illumination, such a condition is not possible with the intensities of incident light employed in this experiment. The energies of the molecular orbitals of the nanotubes can be calculated as given here. The energy of the highest occupied molecular orbital (HOMO) was calculated from the work function (WF) and the optical gap using $\mathrm{HOMO} = \mathrm{WF} - 1/2\,\mathrm{E_G}$, and for the lowest unoccupied molecular orbital (LUMO), it can be determined as $\mathrm{LUMO} = \mathrm{E_G} + \mathrm{E_B}$, where $\mathrm{E_G}$ and $\mathrm{E_B}$ are the optical gap and exciton binding energy, respectively. $\mathrm{E_G}$ was obtained from the optical spectrum, and the calculated $\mathrm{E_B}$ were obtained from Capaz et al. and scaled with the dielectric constant of the SiO2 ($\varepsilon = 3.9$).

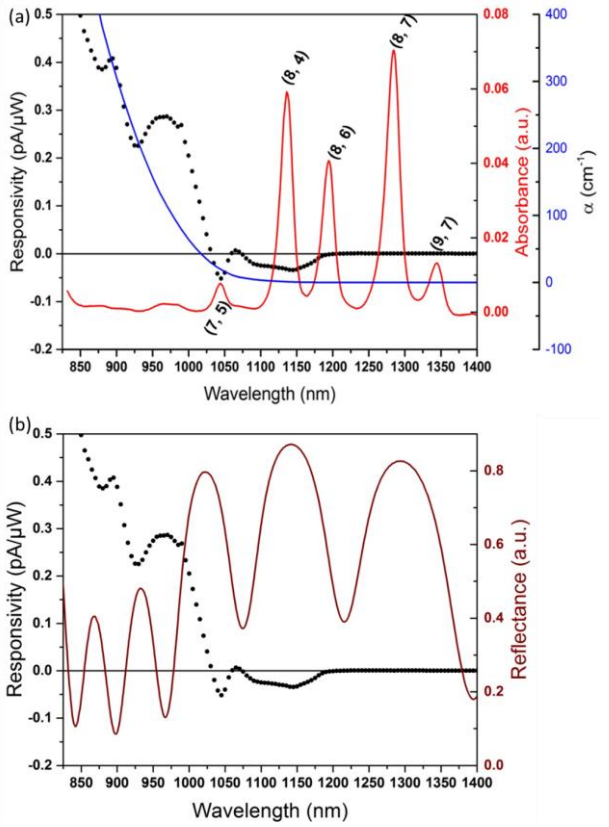

Figure 6.6: Photocurrent responsivity spectrum (a) in comparison with the absorption spectrum of a multi-chiral suspension, along with the absorption coefficient of doped silicon[247] and (b)reflectance spectra of the Si/SiO_2/Si stack . [Reproduced from [66]]

For a (7, 5) CNT the HOMO is at -5.07 eV and the LUMO is at -3.85 eV, with $\mathrm{E_G} = 1.188$ eV and $\mathrm{E_B} = 0.246$ eV. Indeed, in a previous study the (7, 5) HOMO was measured by photoelectron yield spectroscopy in air and is located at 5.09 eV on glass.[28] Although these energy levels shift by -0.4 eV due to the above discussed band bending at the p-Si/SiO_2 interface, the LUMO of the smaller diameter (7, 5) CNT is higher than the conduction band of the Silicon $\mathrm{E_C}$. Therefore, under excitation of a (7, 5) CNT, an injection of electrons to the silicon from the CNT takes place on the high terminal, while holes are injected at the low terminal. This becomes ineffective for a larger diameter tubes with lower LUMO position than the

Silicon E_C, and evidently on illumination, Si is excited causing the electrons to flow towards the low terminal. The data suggests that such configuration is not favorable for photodetection despite the presence of the photoactive CNTs in the wavelength range of interest. Figure 6.7 shows the energy scheme of (a) small diameter (7, 5) and (b) large diameter (10, 9) CNT junctions with p-Si. Note that, using an n-doped silicon would change the energy levels as the LUMO level will not be down shifted of the interface.[232].

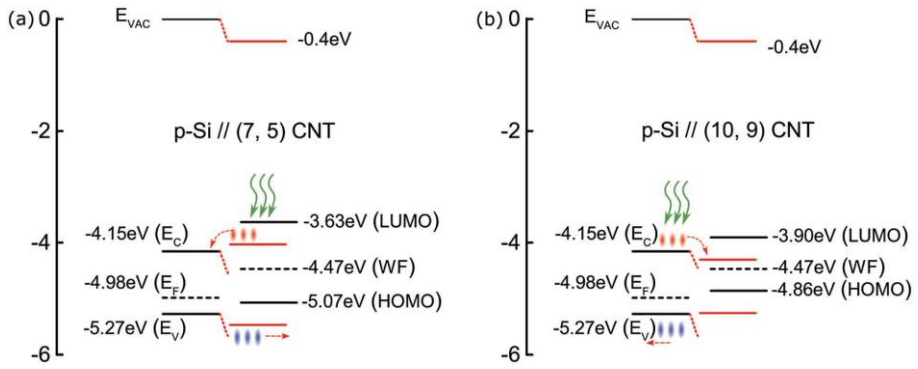

Figure 6.7: Energy levels schemes of (a) p-Si/(7, 5)–CNT and (b) p-Si/(10, 9)–CNT junction under photoexcitation of CNT and Si (green arrows), respectively. The Si conduction band and valence band edges, E_C and E_V, and the HOMO and LUMO levels of the CNTs are given. In contact with p-Si/SiO_2 (natural Si oxide layer not shown), the CNT LUMO and HOMO levels (red lines) are shifted by $-0.4\ eV$ due to band bending at the p-Si/SiO_2 interface (red dotted line). Propagation of electrons (red circles) and holes (blue circles) is indicated. [reproduced from [66]]

To gain further understanding on the photocurrent generation on CNT/p- Si junction, photocurrent studies were continued on devices fabricated with PFO sorted monochiral (6, 5) suspensions on SOI substrates. Figure 6.8 (a) shows the photocurrent response of the monochiral (6, 5) CNTs in comparison with the absorption spectrum in solution and the intensity spectrum from the source, and (b) shows the Figure 6.6 for a direct comparison.

Surprisingly the photocurrent spectrum measured from a monochiral (6, 5) suspensions does not show a negative photocurrent at the S11 transition of (6, 5) at 996 nm as one would expect from the model above. Instead, the photocurrent spectrum shows a negative photocurrent matching the S11 transition of (7, 5), resembling the photocurrent spectrum obtained from few chiral suspensions as shown in Figure 6.6. Hence, the energy band profile model proposed fails to fit the photocurrent generation mechanism for devices integrated with monochiral (6, 5) tubes and has to be reevaluated.

In order to rule out any substrate induced effect, the photocurrent spectroscopy measurements were initially carried out on SOI device structure without any nanotube bridging the 800nm channel width. The photocurrent measurements showed no photo-response in absence of a nanotube bridging across the channel as expected. To gain further understanding, photocurrent measurements were continued on devices integrated with monochiral (6, 5) tubes on silicon on sapphire (SOS) substrates. The photocurrent spectrum measured shows no negative photocurrent as observed in SOI substrates across 1025 nm - 1200 nm, shown in Figure 6.9.

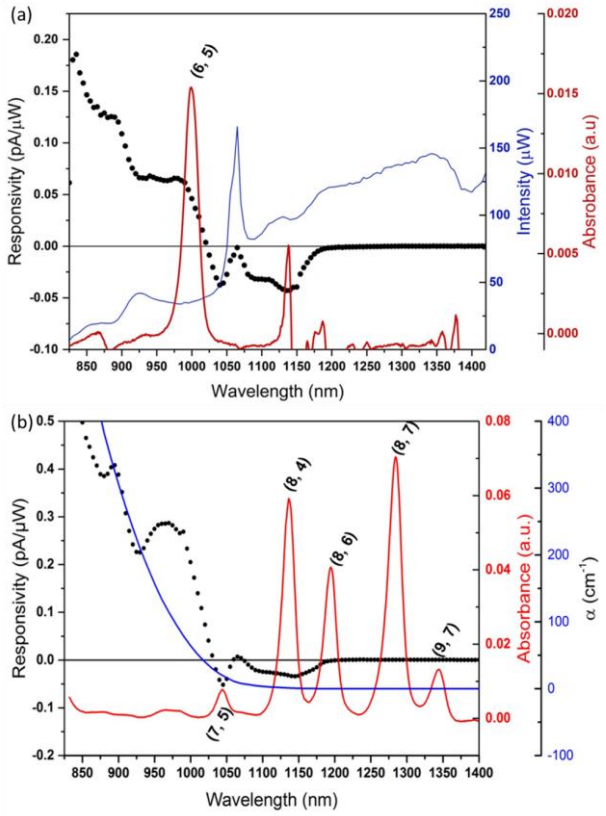

Figure 6.8: Photocurrent responsivity spectrum of a second device. (a) in comparison with absorption spectrum of monochiral (6, 5) suspension and the intensity spectrum of the incident light source. (b) Image 6.6 (a) repeated for comparison.

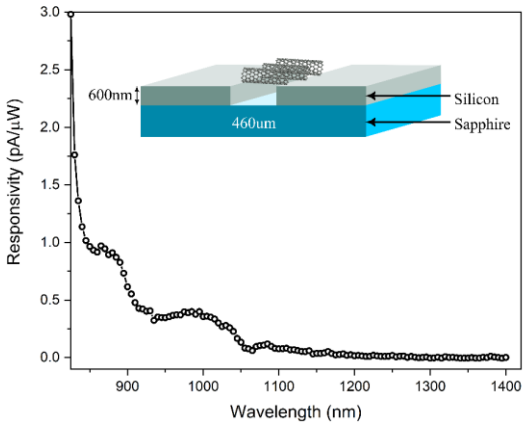

Figure 6.9: Photocurrent Spectrum of Monochiral (6, 5)nanotubes on silicon on sapphire substarte. Inset: The schematic of a device on SOS substrate

Considering the devices on both SOS and SOI substrates, we have two photoactive material present for the targeted wavelength range (825 nm- 1420 nm), namely nanotube and silicon. As monochiral (6, 5) nanotubes have been integrated on both of these devices, the photoresponse from the nanotubes should

be the same. On the other hand, for silicon we have two layers of silicon in the SOI substrate and one layer in the SOS substrate. The silicon layers in the SOI substrate are separated from one another by 3 µm SiO_2(Figure 6.1(a)), which acts as a dielectric spacer between the silicon layers and it resembles a parallel plate capacitor. But after e-beam patterning and etching, the created source (plate-1)-drain (plate-2) electrodes are separated from one another on the top silicon layer for the nanotubes to bridge across. Now, the two electrodes form two isolated capacitor plates on the same plane but with different surface areas (Figure 6.1 (b)). Both of these electrodes are separated from the bottom silicon (plate-3) by SiO_2 layer (See Figure 6.10)

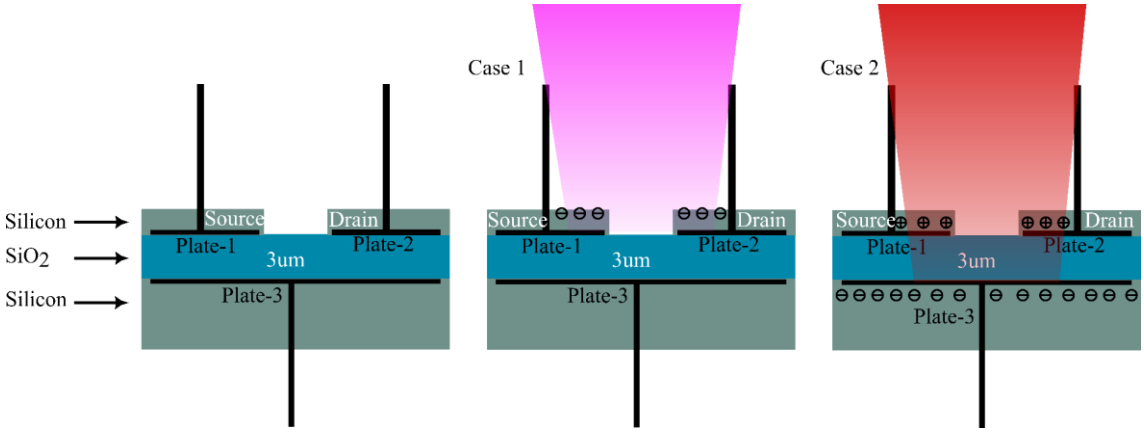

Figure 6.10:Schematic to explain, parallel plate capacitor model.

On illumination, the top p-Si (figure 6.10 - case1) (source and drain electrodes) absorbs shorter wavelengths from 825 nm to 1025 nm generating electron hole pairs. This results in charge accumulation on the oxide side for both source (plate-1) and drain (plate-2) contacts across the nanotube. The extent of charging is controlled by the dimensional area of the electrodes, and as the surface area of the common drain electrode is twice as that of the source electrode (see Figure 6.1(b)), a potential difference is created across them. This potential difference leads to a flow of charge in the positive direction (source to drain). Beyond 1025 nm till 1200 nm, the (figure 6.10 – case 2) bottom silicon (plate-3) becomes active as the top silicon is too thin to absorb longer wavelengths. A similar surface charging effect at the oxide interface occurs with the bottom silicon (plate-3), being a common parallel plate to the source (plate-1) and drain (plate-2) electrodes it charges them with a complement charge due to the capacitance effect. This causes a reverse flow of current or a negative photocurrent (drain to source). Such a model explains the photo-response from the monochiral (6, 5) tube on contact with the p-type silicon on SOI. This also agrees with the photo-response from the SOS substrates, showing no negative photocurrent due to absence of a bottom silicon in SOS substrates. However, this mechanism would not stand true for CNTs forming a large Schottky barrier with p- silicon. As splitting of excitons generated from nanotube would be possible. Also, as the bottom silicon on SOI substrate is at floating potential for all the photocurrent measurements reported in this chapter, the exact potential of the bottom silicon would be questionable at any given time.

6.4 Conclusion

The photocurrent measurements were carried out in similar fashion to that described in Chapter 5. The photocurrent signal was measured across the p-Si/CNT junctions, to explore CNTs as on chip photodetectors in silicon photonics in the near infrared region. On integrating a few chiral tubes on to the silicon

platform, the relative chirality specific contribution to the photocurrent generation were understood with an energy scheme model, where the smaller diameter (7, 5) and (7, 6) tubes could contribute due to a favorable energy difference between the LUMO of the CNTs and the conduction band of silicon. However, the larger diameter (8, 6) (8, 7) and (9, 7) CNTs do not contribute due to the unfavorable energy conditions. In order to gain further clarity, the experiments were continued with monochiral (6, 5) suspensions on two different substrates. The experimental data revealed that the initially proposed energy band profile model has to be reconsidered due to close resemblance of the photocurrent spectra from two different dispersions on SOI substrates. This suggests a possibility of substrate induced effect, which is supported by the photocurrent data obtained monochiral (6, 5) integrated devices on SOS substrate.

It is to be noted that the substrate induced effect is still speculative. Hence, further photocurrent studies with other bulk semiconductors like germanium and n-silicon could provide a better insight on nanotube/semiconductor junctions. Also, larger diameter SWCNTs like (9, 7) and (9, 8) on n-silicon are expected to show a similar negative photoresponse on their respective S11 transition, according to the energy band profile model.

7 Conclusion and Future Work

7.1 Conclusion

In this thesis, the length distribution of polymer wrapped monochiral s-SWCNTs in organic solvent was measured by analytical ultracentrifugation (AUC) technique. For the PFO wrapped (7, 5) SWCNTs in toluene, we have found empirically simple correlation between the sedimentation coefficient and the nanotube length ($s = 1.9 \times 10^4 Sv/m^{1/2} \cdot \sqrt{L}$), which enables us to calculate the length distribution from the sedimentation coefficient distribution, in contrary, to the rod model that worked for aqueous suspensions. The underlying square root length dependence of the friction coefficient suggests that there could be shape fluctuations due to polymer wrapping of the nanotubes. The results have been bench marked with the AFM measurements by converting the volume distribution to number distributions. The method has potential for hassle-free in situ length characterization of PFO wrapped SWCNTs.

Also, photocurrent spectroscopy was performed on a variety of solution processed carbon nanotubes integrated into devices in a transistor configuration. The unique (n, m) dependent inter-band optical transition was displayed distinctly under photocurrent spectroscopy, enabling them to be an ideal tool for on chip characterization of the nanotubes. Eventually, it was shown that nanotubes can be narrow band optical detectors. The photocurrent spectrum itself was refined from substrate influences by using sapphire as a substrate. Also, the device geometry was designed with the consideration for an appropriate electric field environment on the device surface. The electrostatic pn junction created by electrostatic gating from the split gates to enhance the photocurrent generation were dominated by the Schottky barriers formed at the nanotube –metal contact interfaces. However, the photocurrent spectra could be tailored with external gating by tuning the relative (n, m) specific contribution. Hence, making the few chiral tubes integrated with the split gate devices on a sapphire platform, a broad band tunable optical detector in the nIR region from $1200nm$ to $1600nm$.

Finally, photocurrent spectroscopy was also performed on toluene processed SWCNT integrated devices on silicon platform. The negative photocurrent observed correlated to S11 transition of (7, 5) nanotubes could be explained well with the energy band profile model. However, successive measurements with monochiral (6, 5) nanotube overruled the energy band profile model, due to compelling results towards the substrate induced effects.

7.2 Future Work

This thesis has highlighted the in-situ length analysis of polymer (7, 5) wrapped single walled carbon nanotubes using AUC with a simple square root expression relating the length of the nanotube to the sedimentation coefficient distribution. Further research is required in order to develop an index for the pre-factor for different combinations of polymer to nanotube. This would make AUC a viable replacement for the time consuming AFM technique. Also, a microscopic model taking account of the attached polymer with its density and change in viscosity due to the branched arms has to be developed.

In addition, this thesis has highlighted that sapphire is the right platform for photo detection along with the possibility of enhancing the photocurrent generation by creating an electrostatic pn-junction for nanotubes in the nIR spectral range. However, it was found that the Schottky barriers formed at the nanotube/metal contact interfaces dominated over the electrostatically formed pn-junctions suggesting that further research has to be done on finding the suitable contact for the nanotube of choice to realize the pn-junction. Typically, increasing the contact length between the nanotube and the metal contact interface would suffice the need for the few chirality suspensions studied in Chapter 5. Also, a better dielectric film quality between the gates and the electrodes would improve the generation of stronger pn-junctions along the nanotube channel.

Finally, the thesis highlights the peculiar photoresponse of solution processed few chiral and monochiral (6, 5) nanotube/p-silicon junction. The devices fabricated with the nanotubes initially showed a change in photocurrent direction which coincidentally matched with the S11 transition of the smaller diameter tubes and not for the larger diameter tubes, which was not been reported before. However, on continuing the work with a monochiral (6, 5) suspension it rather seemed a substrate effect instead of the photoresponse from the tubes. As this is still speculative, a scope to further continue this work with larger diameter tube and n silicon, along with other bulk semiconductors like germanium and switching between smaller and larger diameter tubes, would answer the argument

References

1. Svensson, J. & Campbell, E. E. B. Schottky barriers in carbon nanotube-metal contacts. *J. Appl. Phys.* **110**, (2011).
2. Moore, G. E. Cramming more components onto integrated circuits, Reprinted from Electronics, volume 38, number 8, April 19, 1965, pp.114 ff. *IEEE Solid-State Circuits Soc. Newsl.* (2009).
3. Iijima, S. © 19 9 1 Nature Publishing Group 그라첼꺼. *Nature* **354**, 56–58 (1991).
4. Heer, W. A. De, Chatelain, A. & Ugarte, D. Walt A. de Heer,* A. Chatelain, D. Ugarte. **270**, (1995).
5. McEuen, P. L. Single-wall carbon nanotubes. *Phys. World* **13**, 31–36 (2000).
6. Pyatkov, F. *et al.* Cavity-enhanced light emission from electrically driven carbon nanotubes. *Nat. Photonics* **10**, 420–427 (2016).
7. Grobert, N. Kleine Röhren: Carbon Nanotubes: Basic Concepts and Physical Properties. Von S. Reich, C. Thomson, J. Maultzsch. Wiley-VCH, Weinheim 2004. 215 Seiten, geb., 99,- Euro. ISBN 3-527-40386-8. *Nachrichten aus der Chemie* **52**, 945–945 (2004).
8. Ado Jorio, G. D. & Dresselhaus, M. S. Carbon nanotubes: Advanced topics in the synthesis, structure, properties and applications. *Mater. Today* **11**, 57 (2008).
9. De Volder, M. F. L., Tawfick, S. H., Baughman, R. H. & Hart, A. J. Carbon Nanotubes: Present and Future Commercial Applications. *Science (80-.).* **339**, 535–539 (2013).
10. Sinha, N. & Yeow, J. T.-W. Carbon Nanotubes for Biomedical Applications. *IEEE Trans. Nanobioscience* **4**, 180–195 (2005).
11. Khare, R. & Bose, S. Carbon Nanotube Based Composites- A Review. *J. Miner. Mater. Charact. Eng.* **04**, 31–46 (2005).
12. Pugno, N. M. On the strength of the carbon nanotube-based space elevator cable: from nanomechanics to megamechanics. *J. Phys. Condens. Matter* **18**, S1971–S1990 (2006).
13. Wilson, N. R. & Macpherson, J. V. Carbon nanotube tips for atomic force microscopy. *Nat. Nanotechnol.* **4**, 483–491 (2009).
14. Berber, S., Kwon, Y.-K. & Tománek, D. Unusually High Thermal Conductivity of Carbon Nanotubes. *Phys. Rev. Lett.* **84**, 4613–4616 (2000).
15. Han, Z. & Fina, A. Thermal conductivity of carbon nanotubes and their polymer nanocomposites: A review. *Prog. Polym. Sci.* **36**, 914–944 (2011).
16. Kreupl, F. Carbon nanotubes finally deliver Fossil raindrops and ancient air. *Nature* 8–9 (2012).
17. Steiner, M. *et al.* High-frequency performance of scaled carbon nanotube array field-effect transistors. *Appl. Phys. Lett.* **101**, 1–5 (2012).
18. Sun, D. M. *et al.* Flexible high-performance carbon nanotube integrated circuits. *Nat. Nanotechnol.* **6**, 156–161 (2011).
19. Shulaker, M. M. *et al.* Carbon nanotube computer. *Nature* **501**, 526–530 (2013).
20. Li, W. S. *et al.* High-quality, highly concentrated semiconducting single-wall carbon nanotubes for use in field effect transistors and biosensors. *ACS Nano* **7**, 6831–6839 (2013).
21. Tans, S. J., Verschueren, A. R. M. & Dekker, C. Room-temperature transistor based on a single carbon nanotube. *Nature* **393**, 49–52 (1998).
22. Saito, R., Fujita, M., Dresselhaus, G. & Dresselhaus, M. S. Electronic structure of chiral graphene tubules. *Appl. Phys. Lett.* **60**, 2204–2206 (1992).
23. Ando, T. Excitons in carbon nanotubes revisited: Dependence on diameter, Aharonov-Bohm flux, and strain.

J. Phys. Soc. Japan **73**, 3351–3363 (2004).

24. Rao, A. M. *et al.* Diameter-selective Raman scattering from vibrational modes in carbon nanotubes. *Science (80-.).* **275**, 187–190 (1997).

25. Shi, Z. *et al.* Observation of a Luttinger-liquid plasmon in metallic single-walled carbon nanotubes. *Nat. Photonics* **9**, 515–519 (2015).

26. Khasminskaya, S., Pyatkov, F., Flavel, B. S., Pernice, W. H. & Krupke, R. Waveguide-integrated light-emitting carbon nanotubes. *Adv. Mater.* **26**, 3465–3472 (2014).

27. Bahena-Garrido, S. *et al.* Plannar light source using a phosphor screen with single-walled carbon nanotubes as field emitters. *Rev. Sci. Instrum.* **85**, (2014).

28. Pfohl, M. *et al.* Probing the Diameter Limit of Single Walled Carbon Nanotubes in SWCNT: Fullerene Solar Cells. *Adv. Energy Mater.* **6**, (2016).

29. Kiang, C. H. *et al.* Cobalt-catalysed growth of carbon nanotubes with single-atomic-layer walls. *Nature* **363**, 605–607 (1993).

30. Journet, C. *et al.* Large-scale production of single-walled carbon nanotubes by the electric-arc technique. *Nature* **388**, 756–758 (1997).

31. Thess, A. *et al.* Crystalline ropes of metallic carbon nanotubes. *Science (80-.).* **273**, 483–487 (1996).

32. Cassell, A. M., Raymakers, J. A., Kong, J. & Dai, H. Large Scale CVD Synthesis of Single-Walled Carbon Nanotubes. *J. Phys. Chem. B* **103**, 6484–6492 (1999).

33. Hou, P. X. *et al.* Preparation of metallic single-wall carbon nanotubes by selective etching. *ACS Nano* **8**, 7156–7162 (2014).

34. Li, Y. *et al.* Preferential Growth of Semiconducting Single-Walled Carbon Nanotubes by a Plasma Enhanced CVD Method. *Nano Lett.* **4**, 317–321 (2004).

35. Komatsu, N. & Wang, F. A comprehensive review on separation methods and techniques for single-walled carbon nanotubes. *Materials (Basel).* **3**, 3818–3844 (2010).

36. Xie, X. *et al.* Microwave purification of large-area horizontally aligned arrays of single-walled carbon nanotubes. *Nat. Commun.* **5**, 1–11 (2014).

37. Li, J., Franklin, A. D. & Liu, J. Gate-Free Electrical Breakdown of Metallic Pathways in Single-Walled Carbon Nanotube Crossbar Networks. *Nano Lett.* **15**, 6058–6065 (2015).

38. Zheng, M. *et al.* Structure-Based Carbon Nanotube Sorting by Sequence-Dependent DNA Assembly. *Science (80-.).* **302**, 1545–1548 (2003).

39. Voggu, R., Rao, K. V., George, S. J. & Rao, C. N. R. A simple method of separating metallic and semiconducting single-walled carbon nanotubes based on molecular charge transfer. *J. Am. Chem. Soc.* **132**, 5560–5561 (2010).

40. Li, X. *et al.* Langmuir-Blodgett assembly of densely aligned single-walled carbon nanotubes from bulk materials. *J. Am. Chem. Soc.* **129**, 4890–4891 (2007).

41. Behnam, A. *et al.* High-field transport and thermal reliability of sorted carbon nanotube network devices. *ACS Nano* **7**, 482–490 (2013).

42. Arnold, M. S., Green, A. A., Hulvat, J. F., Stupp, S. I. & Hersam, M. C. Sorting carbon nanotubes by electronic structure using density differentiation. *Nat. Nanotechnol.* **1**, 60–65 (2006).

43. Tanaka, T. *et al.* Simple and scalable gel-based separation of metallic and semiconducting carbon nanotubes. *Nano Lett.* **9**, 1497–1500 (2009).

44. Tulevski, G. S., Franklin, A. D. & Afzali, A. High purity isolation and quantification of semiconducting carbon nanotubes via column chromatography. *ACS Nano* **7**, 2971–2976 (2013).

45. Zhu, S. N. *et al.* Separation of metallic single-walled carbon nanotubes and semiconducting single-walled carbon nanotubes by Agarose gel electrophoresis. *Fenxi Huaxue/ Chinese J. Anal. Chem.* **40**, 1839–1844 (2012).

46. Mistry, K. S., Larsen, B. A. & Blackburn, J. L. High-yield dispersions of large-diameter semiconducting single-

walled carbon nanotubes with tunable narrow chirality distributions. *ACS Nano* **7**, 2231–2239 (2013).

47. Gomulya, W., Gaoa, J. & Loib, M. A. Conjugated polymer-wrapped carbon nanotubes: Physical properties and device applications. *Eur. Phys. J. B* **86**, (2013).

48. Lemasson, F. *et al.* Polymer library comprising fluorene and carbazole homo- and copolymers for selective single-walled carbon nanotubes extraction. *Macromolecules* **45**, 713–722 (2012).

49. LeMieux, M. C. *et al.* Self-sorted, aligned nanotube networks for thin-film transistors. *Science (80-.).* **321**, 101–104 (2008).

50. Wang, Y., Pillai, S. K. R. & Chan-Park, M. B. High-performance partially aligned semiconductive single-walled carbon nanotube transistors achieved with a parallel technique. *Small* **9**, 2960–2969 (2013).

51. Cao, Q. *et al.* Arrays of single-walled carbon nanotubes with full surface coverage for high-performance electronics. *Nat. Nanotechnol.* **8**, 180–186 (2013).

52. Krupke, R., Hennrich, F., Löhneysen, H. v. & Kappes, M. M. Separation of metallic from semiconducting single-walled carbon nanotubes. *Science* **301**, 344–347 (2003).

53. Cao, Q., Han, S. J. & Tulevski, G. S. Fringing-field dielectrophoretic assembly of ultrahigh-density semiconducting nanotube arrays with a self-limited pitch. *Nat. Commun.* **5**, 1–7 (2014).

54. Krupke, R., Hennrich, F., Weber, H. B., Kappes, M. M. & Löhneysen, H. V. Simultaneous deposition of metallic bundles of single-walled carbon nanotubes using ac-dielectrophoresis. *Nano Lett.* **3**, 1019–1023 (2003).

55. Krupke, R. *et al.* Contacting single bundles of carbon nanotubes with alternating electric fields. *Appl. Phys. A Mater. Sci. Process.* **76**, 397–400 (2003).

56. Vijayaraghavan, A. *et al.* Ultra-large-scale directed assembly of single-walled carbon nanotube devices. *Nano Lett.* **7**, 1556–1560 (2007).

57. Li, W., Hennrich, F., Flavel, B. S., Kappes, M. M. & Krupke, R. Chiral-index resolved length mapping of carbon nanotubes in solution using electric-field induced differential absorption spectroscopy. *Nanotechnology* **27**, (2016).

58. Krupke, R., Hennrich, F., Kappes, M. M. & Löhneysen, H. V. Surface conductance induced dielectrophoresis of semiconducting single-walled carbon nanotubes. *Nano Lett.* **4**, 1395–1399 (2004).

59. Perebeinos, V. & Avouris, P. Exciton ionization, Franz-Keldysh, and stark effects in carbon nanotubes. *Nano Lett.* **7**, 609–613 (2007).

60. Tsen, A. W., Donev, L. A. K., Kurt, H., Herman, L. H. & Park, J. Imaging the electrical conductance of individual carbon nanotubes with photothermal current microscopy. *Nat. Nanotechnol.* **4**, 108–113 (2009).

61. Kumamoto, Y. *et al.* Spontaneous exciton dissociation in carbon nanotubes. *Phys. Rev. Lett.* **112**, 1–5 (2014).

62. Zhang, S. *et al.* Bolometric-Effect-Based Wavelength-Selective Photodetectors Using Sorted Single Chirality Carbon Nanotubes. *Sci. Rep.* **5**, 1–7 (2015).

63. Buchs, G., Bagiante, S. & Steele, G. A. Identifiying signatures of photothermal current in a double-gated semiconducting nanotube. *Nat. Commun.* **5**, 1–6 (2014).

64. St-Antoine, B. C., Ménard, D. & Martel, R. Single-walled carbon nanotube thermopile for broadband light detection. *Nano Lett.* **11**, 609–613 (2011).

65. St-Antoine, B. C., Ménard, D. & Martel, R. Photothermoelectric effects in single-walled carbon nanotube films: Reinterpreting scanning photocurrent experiments. *Nano Res.* **5**, 73–81 (2012).

66. Riaz, A. *et al.* Near-Infrared Photoresponse of Waveguide-Integrated Carbon Nanotube–Silicon Junctions. *Adv. Electron. Mater.* **5**, 1–6 (2019).

67. Zhang, H., Wu, B., Hu, W. & Liu, Y. Separation and/or selective enrichment of single-walled carbon nanotubes based on their electronic properties. *Chem. Soc. Rev.* **40**, 1324–1336 (2011).

68. Dresselhaus, M. S., Dresselhaus, G. & Saito, R. Physics of carbon nanotubes. *Carbon N. Y.* **33**, 883–891 (1995).

69. Proctor, J. E., Melendrez Armada, D. & Vijayaraghavan, A. *An Introduction to Graphene and Carbon Nanotubes.* (CRC Press, 2016).

70. Mintmire, J. W. & White, C. T. Universal Density of States for Carbon Nanotubes. *Phys. Rev. Lett.* **81**, 2506–2509 (1998).

71. Zhang, H., Wu, B., Hu, W. & Liu, Y. Separation and/or selective enrichment of single-walled carbon nanotubes based on their electronic properties. *Chem. Soc. Rev.* **40**, 1324–1336 (2011).

72. Reich, S., Maultzsch, J., Thomsen, C. & Ordejón, P. Tight-binding description of graphene. *Phys. Rev. B* **66**, 035412 (2002).

73. Castro Neto, A. H., Guinea, F., Peres, N. M. R., Novoselov, K. S. & Geim, A. K. The electronic properties of graphene. *Rev. Mod. Phys.* **81**, 109–162 (2009).

74. Alfonsi, J. Small crystal models for the electronic properties of carbon nanotubes. 182 (2008).

75. Charlier, J.-C., Blase, X. & Roche, S. Electronic and transport properties of nanotubes. *Rev. Mod. Phys.* **79**, 677–732 (2007).

76. Htoon, H., O'Connell, M. J., Doom, S. K. & Klimov, V. I. Single carbon nanotubes probed by photoluminescence excitation spectroscopy: The role of phonon-assisted transitions. *Phys. Rev. Lett.* **94**, 1–4 (2005).

77. Jorio, A. *et al.* Joint density of electronic states for one isolated single-wall carbon nanotube studied by resonant Raman scattering. *Phys. Rev. B* **63**, 245416 (2001).

78. Hansson, A., Paulsson, M. & Stafström, S. Effect of bending and vacancies on the conductance of carbon nanotubes. *Phys. Rev. B* **62**, 7639–7644 (2000).

79. Kim, P., Odom, T. W., Huang, J.-L. & Lieber, C. M. Electronic Density of States of Atomically Resolved Single-Walled Carbon Nanotubes: Van Hove Singularities and End States. *Phys. Rev. Lett.* **82**, 1225–1228 (1999).

80. Benedict, L. X., Louie, S. G. & Cohen, M. L. Static polarizabilities of single-wall carbon nanotubes. *Phys. Rev. B* **52**, 8541–8549 (1995).

81. Ajiki, H. & Ando, T. Aharonov-Bohm effect in carbon nanotubes. *Phys. B Condens. Matter* **201**, 349–352 (1994).

82. Ajiki, H. & Ando, T. Carbon Nanotubes: Optical Absorption in Aharonov-Bohm Flux. *Jpn. J. Appl. Phys.* **34**, 107 (1995).

83. Miyauchi, Y., Oba, M. & Maruyama, S. Cross-polarized optical absorption of single-walled nanotubes by polarized photoluminescence excitation spectroscopy. *Phys. Rev. B* **74**, 205440 (2006).

84. O'Connell, M. J. Band Gap Fluorescence from Individual Single-Walled Carbon Nanotubes. *Science (80-.).* **297**, 593–596 (2002).

85. Lefebvre, J., Fraser, J. M., Finnie, P. & Homma, Y. Photoluminescence from an individual single-walled carbon nanotube. *Phys. Rev. B* **69**, 075403 (2004).

86. Lebedkin, S. *et al.* FTIR-luminescence mapping of dispersed single-walled carbon nanotubes. *New J. Phys.* **5**, 140–140 (2003).

87. Kinder, J. M. & Mele, E. J. Nonradiative recombination of excitons in carbon nanotubes mediated by free charge carriers. *Phys. Rev. B* **78**, 155429 (2008).

88. Avouris, P., Chen, J., Freitag, M., Perebeinos, V. & Tsang, J. C. Carbon nanotube optoelectronics. *Phys. status solidi* **243**, 3197–3203 (2006).

89. Lauret, J.-S. *et al.* Ultrafast Carrier Dynamics in Single-Wall Carbon Nanotubes. *Phys. Rev. Lett.* **90**, 057404 (2003).

90. Manzoni, C. *et al.* Intersubband Exciton Relaxation Dynamics in Single-Walled Carbon Nanotubes. *Phys. Rev. Lett.* **94**, 207401 (2005).

91. Reich, S., Dworzak, M., Hoffmann, A., Thomsen, C. & Strano, M. S. Excited-state carrier lifetime in single-walled carbon nanotubes. *Phys. Rev. B* **71**, 033402 (2005).

92. Li, Z., Tang, Z., Liu, H., *et al.* Polarized Absorption Spectra of Single-Walled 4 Å Carbon Nanotubes Aligned in Channels of an $AlPO_4$ -5 Single Crystal. *Phys. Rev. Lett.* **87**, 127401 (2001).

93. Bachilo, S. M. Structure-Assigned Optical Spectra of Single-Walled Carbon Nanotubes. *Science (80-.)?.* **298**, 2361–2366 (2002).

94. Ichida, M. *et al.* Coulomb effects on the fundamental optical transition in semiconducting single-walled carbon nanotubes: Divergent behavior in the small-diameter limit. *Phys. Rev. B* **65**, 241407 (2002).

95. Kane, C. L. & Mele, E. J. Ratio Problem in Single Carbon Nanotube Fluorescence Spectroscopy. *Phys. Rev. Lett.* **90**, 207401 (2003).

96. Gokus, T. Photoluminescence and Elastic White Light Scattering Studies of Individual Carbon Nanotubes and Optical Characterization of Oxygen Plasma Treated Graphene. 253 (2011).

97. Maultzsch, J. *et al.* Exciton binding energies in carbon nanotubes from two-photon photoluminescence. *Phys. Rev. B - Condens. Matter Mater. Phys.* **72**, 1–4 (2005).

98. Spataru, C. D., Ismail-Beigi, S., Benedict, L. X. & Louie, S. G. Excitonic Effects and Optical Spectra of Single-Walled Carbon Nanotubes. *Phys. Rev. Lett.* **92**, 077402 (2004).

99. Haug, H. & Koch, S. W. SEMICONDUCTOR QUANTUM WIRES. in *Quantum Theory of the Optical and Electronic Properties of Semiconductors*, 324-331(1990).

100. Avouris, P., Freitag, M. & Perebeinos, V. Carbon-nanotube photonics and optoelectronics. *Nat. Photonics* **2**, 341–350 (2008).

101. Wang, F. The Optical Resonances in Carbon Nanotubes Arise from Excitons. *Science* **308**, 838–841 (2005).

102. Demming, A. Multitasking in nanotechnology. *Nanotechnology* **24**, 220201–220201 (2013).

103. Ohno, Y. *et al.* Excitonic transition energies in single-walled carbon nanotubes: Dependence on environmental dielectric constant. *Phys. status solidi* **244**, 4002–4005 (2007).

104. Wang, F. *et al.* Observation of Excitons in One-Dimensional Metallic Single-Walled Carbon Nanotubes. *Phys. Rev. Lett.* **99**, 227401 (2007).

105. Perebeinos, V., Tersoff, J. & Avouris, P. Scaling of excitons in carbon nanotubes. *Phys. Rev. Lett.* **92**, 8–11 (2004).

106. Tune, D. D. & Flavel, B. S. Advances in Carbon Nanotube-Silicon Heterojunction Solar Cells. *Adv. Energy Mater.* **8**, 1703241 (2018).

107. Ando, T. Effects of Valley Mixing and Exchange on Excitons in Carbon Nanotubes with Aharonov–Bohm Flux. *J. Phys. Soc. Japan* **75**, 024707 (2006).

108. Xiong, W. *et al.* Direct writing of graphene patterns on insulating substrates under ambient conditions. *Sci. Rep.* **4**, 4892 (2015).

109. Kishida, H., Nagasawa, Y., Imamura, S. & Nakamura, A. Direct Observation of Dark Excitons in Micelle-Wrapped Single-Wall Carbon Nanotubes. *Phys. Rev. Lett.* **100**, 097401 (2008).

110. Mortimer, I. B. & Nicholas, R. J. Role of Bright and Dark Excitons in the Temperature-Dependent Photoluminescence of Carbon Nanotubes. *Phys. Rev. Lett.* **98**, 027404 (2007).

111. Kiowski, O., Arnold, K., Lebedkin, S., Hennrich, F. & Kappes, M. M. Direct Observation of Deep Excitonic States in the Photoluminescence Spectra of Single-Walled Carbon Nanotubes. *Phys. Rev. Lett.* **99**, 237402 (2007).

112. Amori, A. R., Rossi, J. E., Landi, B. J. & Krauss, T. D. Defects Enable Dark Exciton Photoluminescence in Single-Walled Carbon Nanotubes. *J. Phys. Chem. C* **122**, 3599–3607 (2018).

113. Weisman, R. B. & Bachilo, S. M. Dependence of optical transition energies on structure for single-walled carbon nanotubes in aqueous suspension: An empirical Kataura plot. *Nano Lett.* **3**, 1235–1238 (2003).

114. Lefebvre, J., Fraser, J. M., Homma, Y. & Finnie, P. Photoluminescence from single-walled carbon nanotubes: a comparison between suspended and micelle-encapsulated nanotubes. *Appl. Phys. A* **78**, 1107–1110 (2004).

115. Pichler, T. *et al.* Localized and Delocalized Electronic States in Single-Wall Carbon Nanotubes. *Phys. Rev. Lett.* **80**, 4729–4732 (1998).

116. Datta, S. *Electronic Transport in Mesoscopic Systems*. *Electronic Transport in Mesoscopic Systems* (Cambridge University Press, 1995). ISBN:9780511805776 doi:10.1017/CBO9780511805776.

117. McEuen, P. L., Bockrath, M., Cobden, D. H., Yoon, Y.-G. & Louie, S. G. Disorder, Pseudospins, and Backscattering in Carbon Nanotubes. *Phys. Rev. Lett.* **83**, 5098–5101 (1999).

118. Yao, Z., Kane, C. L. & Dekker, C. High Field Electrical Transport in Single-Wall Carbon Nanotubes. *Phys. Rev. Lett.* **84**, 2941–2944 (2000).

119. Park, J.-Y. *et al.* Electron−Phonon Scattering in Metallic Single-Walled Carbon Nanotubes. *Nano Lett.* **4**, 517–520 (2004).

120. Javey, A. *et al.* High-Field Quasiballistic Transport in Short Carbon Nanotubes. *Phys. Rev. Lett.* **92**, 106804 (2004).

121. Li, W. Advanced Dielectrophoresis for Carbon Nanotube Electronics. 168 (2017).

122. Ganzhorn, M. *et al.* A Scalable, CMOS-Compatible Assembly of Ambipolar Semiconducting Single-Walled Carbon Nanotube Devices. *Adv. Mater.* **23**, 1734–1738 (2011).

123. Jensen, L., Schmidt, O. H., Mikkelsen, K. V. & Åstrand, P.-O. Static and Frequency-Dependent Polarizability Tensors for Carbon Nanotubes. *J. Phys. Chem. B* **104**, 10462–10466 (2000).

124. Jensen, L., Åstrand, P. O. & Mikkelsen, K. V. The static polarizability and second hyperpolarizability of fullerenes and carbon nanotubes. *J. Phys. Chem. A* **108**, 8795–8800 (2004).

125. Kozinsky, B. & Marzari, N. Static Dielectric Properties of Carbon Nanotubes from First Principles. *Phys. Rev. Lett.* **96**, 166801 (2006).

126. Seo, H.-W., Han, C.-S., Choi, D.-G., Kim, K.-S. & Lee, Y.-H. Controlled assembly of single SWNTs bundle using dielectrophoresis. *Microelectron. Eng.* **81**, 83–89 (2005).

127. Heinze, S. *et al.* Carbon Nanotubes as Schottky Barrier Transistors. *Phys. Rev. Lett.* **89**, 106801 (2002).

128. Martel, R., Schmidt, T., Shea, H. R., Hertel, T. & Avouris, P. Single- and multi-wall carbon nanotube field-effect transistors. *Appl. Phys. Lett.* **73**, 2447–2449 (1998).

129. Léonard, F. & Talin, A. A. Electrical contacts to one- and two-dimensional nanomaterials. *Nat. Nanotechnol.* **6**, 773–783 (2011).

130. Franklin, A. D. & Chen, Z. Length scaling of carbon nanotube transistors. *Nat. Nanotechnol.* **5**, 858–862 (2010).

131. Léonard, F. & Tersoff, J. Role of Fermi-Level Pinning in Nanotube Schottky Diodes. *Phys. Rev. Lett.* **84**, 4693–4696 (2000).

132. Chen, Z., Appenzeller, J., Knoch, J., Lin, Y. & Avouris, P. The Role of Metal–Nanotube Contact in the Performance of Carbon Nanotube Field-Effect Transistors. *Nano Lett.* **5**, 1497–1502 (2005).

133. Javey, A., Guo, J., Wang, Q., Lundstrom, M. & Dai, H. Ballistic carbon nanotube field-effect transistors. *Nature* **424**, 654–657 (2003).

134. Barkelid, M. & Zwiller, V. Photocurrent generation in semiconducting and metallic carbon nanotubes. *Nat. Photonics* **8**, 47–51 (2014).

135. St-Antoine, B. C., Ménard, D. & Martel, R. Position Sensitive Photothermoelectric Effect in Suspended Single-Walled Carbon Nanotube Films. *Nano Lett.* **9**, 3503–3508 (2009).

136. Wang, F. *et al.* High Conversion Efficiency Carbon Nanotube-Based Barrier-Free Bipolar-Diode Photodetector. *ACS Nano* **10**, 9595–9601 (2016).

137. Amer, M. R., Chang, S.-W., Dhall, R., Qiu, J. & Cronin, S. B. Zener Tunneling and Photocurrent Generation in Quasi-Metallic Carbon Nanotube pn-Devices. *Nano Lett.* **13**, 5129–5134 (2013).

138. DeBorde, T., Aspitarte, L., Sharf, T., Kevek, J. W. & Minot, E. D. Photothermoelectric Effect in Suspended Semiconducting Carbon Nanotubes. *ACS Nano* **8**, 216–221 (2014).

139. Braidy, N., El Khakani, M. . & Botton, G. . Single-wall carbon nanotubes synthesis by means of UV laser vaporization. *Chem. Phys. Lett.* **354**, 88–92 (2002).

140. Zheng, B. *et al.* Efficient CVD Growth of Single-Walled Carbon Nanotubes on Surfaces Using Carbon Monoxide Precursor. *Nano Lett.* **2**, 895–898 (2002).

141. Kong, J., Cassell, A. M. & Dai, H. Chemical vapor deposition of methane for single-walled carbon nanotubes. *Chem. Phys. Lett.* **292**, 567–574 (1998).

142. Lyu, S. C. *et al.* Large-Scale Synthesis of High-Quality Double-Walled Carbon Nanotubes by Catalytic

Decomposition of n -Hexane. *J. Phys. Chem. B* **108**, 2192–2194 (2004).

143. Tian, Y. *et al.* In Situ TA-MS Study of the Six-Membered-Ring-Based Growth of Carbon Nanotubes with Benzene Precursor. *J. Am. Chem. Soc.* **126**, 1180–1183 (2004).

144. Resasco, D. E. *et al.* A scalable process for production of single-walled carbon nanotubes (SWNTs) by catalytic disproportionation of CO on a solid catalyst. *J. Nanoparticle Res.* **4,** 131-136 (2002)

145. Nikolaev, P. *et al.* Gas-phase catalytic growth of single-walled carbon nanotubes from carbon monoxide. *Chem. Phys. Lett.* **313**, 91-97 (1999)

146. Bronikowski, M. J., Willis, P. A., Colbert, D. T., Smith, K. A. & Smalley, R. E. Gas-phase production of carbon single-walled nanotubes from carbon monoxide via the HiPco process: A parametric study. *J. Vac. Sci. Technol. A Vacuum, Surfaces, Film.* **19**, 1800 (2001).

147. Liu, B., Wu, F., Gui, H., Zheng, M. & Zhou, C. Chirality-Controlled Synthesis and Applications of Single-Wall Carbon Nanotubes. *ACS Nano* **11**, 31–53 (2017).

148. Arepalli, S. Laser ablation process for single-walled carbon nanotube production. in *Journal of Nanoscience and Nanotechnology* **4**, 317-325 (2004).

149. Kingston, C. T. & Simard, B. Recent Advances in Laser Synthesis of Single-Walled Carbon Nanotubes. *J. Nanosci. Nanotechnol.* **6**, 1225–1232 (2006).

150. Eklund, P. C. *et al.* Large-Scale Production of Single-Walled Carbon Nanotubes Using Ultrafast Pulses from a Free Electron Laser. *Nano Lett.* **2**, 561-566 (2002).

151. Liu, H., Nishide, D., Tanaka, T. & Kataura, H. Large-scale single-chirality separation of single-wall carbon nanotubes by simple gel chromatography. *Nat. Commun.* **2**, (2011).

152. Xu, Z., Yang, X. & Yang, Z. A Molecular Simulation Probing of Structure and Interaction for Supramolecular Sodium Dodecyl Sulfate/Single-Wall Carbon Nanotube Assemblies. *Nano Lett.* **10**, 985–991 (2010).

153. Tvrdy, K. *et al.* A kinetic model for the deterministic prediction of gel-based single-chirality single-walled carbon nanotube separation. *ACS Nano* **7**, 1779-1789 (2013).

154. Fleurier, R., Lauret, J. S., Lopez, U. & Loiseau, A. Transmission electron microscopy and UV-vis-IR spectroscopy analysis of the diameter sorting of carbon nanotubes by gradient density ultracentrifugation. *Adv. Funct. Mater.* **19**, 2219-2223 (2009).

155. Seo, J. W. T. *et al.* Diameter refinement of semiconducting arc discharge single-walled carbon nanotubes via density gradient ultracentrifugation. *J. Phys. Chem. Lett.* **4**, 2805-2810 (2013).

156. Simien, D. *et al.* Influence of Nanotube Length on the Optical and Conductivity Properties of Thin Single-Wall Carbon Nanotube Networks. *ACS Nano* **2**, 1879–1884 (2008).

157. Bonaccorso, F. *et al.* Density gradient ultracentrifugation of nanotubes: Interplay of bundling and surfactants encapsulation. *J. Phys. Chem. C* **4**, 2805-2810(2010).

158. Shea, M. J., Mehlenbacher, R. D., Zanni, M. T. & Arnold, M. S. Experimental Measurement of the Binding Configuration and Coverage of Chirality-Sorting Polyfluorenes on Carbon Nanotubes. *J. Phys. Chem. Lett.* **5**, 3742–3749 (2014).

159. Wang, H. & Bao, Z. Conjugated polymer sorting of semiconducting carbon nanotubes and their electronic applications. *Nano Today* **10**, 737-758 (2015).

160. Hennrich, F. *et al.* Length-Sorted, Large-Diameter, Polyfluorene-Wrapped Semiconducting Single-Walled Carbon Nanotubes for High-Density, Short-Channel Transistors. *ACS Nano* **10**, 1888–1895 (2016).

161. Gao, J., Loi, M. A., De Carvalho, E. J. F. & Dos Santos, M. C. Selective wrapping and supramolecular structures of polyfluorene-carbon nanotube hybrids. *ACS Nano* **5**, 3993–3999 (2011).

162. Duesberg, G. S., Burghard, M., Muster, J. & Philipp, G. Separation of carbon nanotubes by size exclusion chromatography. *Chem. Commun.*435–436 (1998).

163. Duesberg, G. S., Muster, J., Krstic, V., Burghard, M. & Roth, S. Chromatographic size separation of single-wall carbon nanotubes. *Appl. Phys. A Mater. Sci. Process.* **67**, 117-120 (1998).

164. Tanaka, T., Urabe, Y., Nishide, D. & Kataura, H. Continuous separation of metallic and semiconducting carbon

nanotubes using agarose gel. *Appl. Phys. Express* **2**, 125002 (2009).

165. Piner, R. & Ruoff, R. S. Length distribution of single walled carbon nanotubes determined by ac atomic force microscopy. (2002).

166. Ziegler, K. J. *et al.* Statistically Accurate Length Measurements of Single-Walled Carbon Nanotubes. *J. Nanosci. Nanotechnol.* **7**, 2917–2921 (2007).

167. Wang, S., Liang, Z., Wang, B. & Zhang, C. Statistical characterization of single-wall carbon nanotube length distribution. *Nanotechnology* **17**, 634–639 (2006).

168. Lee, J. Y. *et al.* Electrophoretic and Dynamic Light Scattering in Evaluating Dispersion and Size Distribution of Single-Walled Carbon Nanotubes. *J. Nanosci. Nanotechnol.* **5**, 1045–1049 (2005).

169. Shetty, A. M., Wilkins, G. M. H., Nanda, J. & Solomon, M. J. Multiangle Depolarized Dynamic Light Scattering of Short Functionalized Single-Walled Carbon Nanotubes. *J. Phys. Chem. C* **113**, 7129–7133 (2009).

170. Badaire, S., Poulin, P., Maugey, M. & Zakri, C. In situ measurements of nanotube dimensions in suspensions by depolarized dynamic light scattering. *Langmuir* **20**, 10367–10370 (2004).

171. Bauer, B. J., Fagan, J. A., Hobbie, E. K., Chun, J. & Bajpai, V. Chromatographic fractionation of SWNT/DNA dispersions with on-line multi-angle light scattering. *J. Phys. Chem. C* **112**, 1842–1850 (2008).

172. Pease, L. F. *et al.* Length Distribution of Single-Walled Carbon Nanotubes in Aqueous Suspension Measured by Electrospray Differential Mobility Analysis. *Small* **5**, 2894–2901 (2009).

173. Casey, J. P., Bachilo, S. M., Moran, C. H. & Weisman, R. B. Chirality-Resolved Length Analysis of Single Walled Carbon nanotube samples through Shear Alignment Photoluminesence Anisotropy. *ACS Nano.* **2**, 1738-1746 (2008).

174. Streit, J. K. *et al.* Measuring single-walled carbon nanotube length distributions from diffusional trajectories. *ACS Nano* **6**, 8424–31 (2012).

175. Silvera Batista, C. A., Zheng, M., Khripin, C. Y., Tu, X. & Fagan, J. A. Rod Hydrodynamics and Length Distributions of Single-Wall Carbon Nanotubes Using Analytical Ultracentrifugation. *Langmuir* **30**, 4895–4904 (2014).

176. Li, W., Hennrich, F., Flavel, B. S., Kappes, M. M. & Krupke, R. Chiral-index resolved length mapping of carbon nanotubes in solution using electric-field induced differential absorption spectroscopy. *Nanotechnology* **27**, 375706 (2016).

177. Brady, G. J. *et al.* Polyfluorene-sorted, carbon nanotube array field-effect transistors with increased current density and high on/off ratio. *ACS Nano* **8**, 11614–11621 (2014).

178. Flavel, B. S., Moore, K. E., Pfohl, M., Kappes, M. M. & Hennrich, F. Separation of single-walled carbon nanotubes with a gel permeation chromatography system. *ACS Nano* **8**, 1817-1816 (2014).

179. Selvasundaram, P. B. *et al.* Measuring in Situ Length Distributions of Polymer-Wrapped Monochiral Single-Walled Carbon Nanotubes Dispersed in Toluene with Analytical Ultracentrifugation. *Langmuir* **35**, 3790–3796 (2019).

180. Lamm, O. Zur Theorie und Methodik der Ultrazentrifugierung. *Zeitschrift für Phys. Chemie* **143A**, 177 (1929).

181. Falabella, J. B., Cho, T. J., Ripple, D. C., Hackley, V. A. & Tarlov, M. J. Characterization of gold nanoparticles modified with single-stranded DNA using analytical ultracentrifugation and dynamic light scattering. *Langmuir* **26**, 12740–12747 (2010).

182. Sousa, A. A. *et al.* Synthesis, characterization, and direct intracellular imaging of ultrasmall and uniform glutathione-coated gold nanoparticles. *Small* **8**, 2277–2286 (2012).

183. Lees, E. E. *et al.* Experimental determination of quantum dot size distributions, ligand packing densities, and bioconjugation using analytical ultracentrifugation. *Nano Lett.* **8**, 2883–2890 (2008).

184. Carney, R. P. *et al.* Determination of nanoparticle size distribution together with density or molecular weight by 2D analytical ultracentrifugation. *Nat. Commun.* **2**, 335 (2011).

185. Jamison, J. A. *et al.* Applying analytical ultracentrifugation to nanocrystal suspensions. *Nanotechnology* **20**, 355702 (2009).

186. Zook, J. M., Rastogi, V., MacCuspie, R. I., Keene, A. M. & Fagan, J. Measuring agglomerate size distribution and

dependence of localized surface plasmon resonance absorbance on gold nanoparticle agglomerate size using analytical ultracentrifugation. *ACS Nano* **5**, 8070–8079 (2011).

187. Arnold, M. S., Suntivich, J., Stupp, S. I. & Hersam, M. C. Hydrodynamic characterization of surfactant encapsulated carbon nanotubes using an analytical ultracentrifuge. *ACS Nano* **2**, 2291–2300 (2008).

188. Schuck, P. & Rossmanith, P. Determination of the sedimentation coefficient distribution by least-squares boundary modeling. *Biopolymers* **54**, 328–341 (2000).

189. Fagan, J. A. *et al.* Analyzing Surfactant Structures on Single-Wall Carbon Nanotubes by Analytical Ultracentrifugation. *ACS Nano* **7**, 3373–3387 (2013).

190. Lam, S., Zheng, M. & Fagan, J. A. Characterizing the Effect of Salt and Surfactant Concentration on the Counterion Atmosphere around Surfactant Stabilized SWCNTs Using Analytical Ultracentrifugation. *Langmuir* **32**, 3926–3936 (2016).

191. Harris, K. R. Temperature and Density Dependence of the Viscosity of Toluene. *J. Chem. Eng. Data* **45**, 893–897 (2000).

192. Broersma, S. Rotational Diffusion Constant of a Cylindrical Particle. *J. Chem. Phys.* **32**, 1626–1631 (1960).

193. Batchelor, G. K. Slender-body theory for particles of arbitrary cross-section in Stokes flow. *J. Fluid Mech.* **44**, 419 (1970).

194. Aragon, S. R. & Flamik, D. High precision transport properties of cylinders by the boundary element method. *Macromolecules* **42**, 6290–6299 (2009).

195. Mansfield, M. L. & Douglas, J. F. Transport properties of rodlike particles. *Macromolecules* **41**, 5422–5432 (2008).

196. González, J. M. *et al.* Cooperative behavior of Escherichia coli cell-division protein FtsZ assembly involves the preferential cyclization of long single-stranded fibrils. *Proc. Natl. Acad. Sci. U. S. A.* **102**, 1895–1900 (2005).

197. Fakhri, N., Tsyboulski, D. A., Cognet, L., Weisman, R. B. & Pasquali, M. Diameter-dependent bending dynamics of single-walled carbon nanotubes in liquids. *Proc. Natl. Acad. Sci.* **106**, 14219–14223 (2009).

198. Engel, M. *et al.* Photocurrent Spectroscopy of (n, m) Sorted Solution-Processed Single-Walled Carbon Nanotubes. *ACS Nano* **8**, 9324–9331 (2014).

199. Balasubramanian, K. & Burghard, M. Charge transport through carbon nanotubes interacting with light. *Semicond. Sci. Technol.* **21**, 21–32 (2006).

200. Balasubramanian, K., Burghard, M., Kern, K., Scolari, M. & Mews, A. Photocurrent imaging of charge transport barriers in carbon nanotube devices. *Nano Lett.* **5**, 507-510 (2005).

201. Moore, J. A., Choi, J. O. Degradation of poly(methylmethacrylate) by deep ultraviolet, x-ray, electron beam, and proton beam irradiations. *Radiation effects on polymers.* Chapter **11**, 156-192 (1988).

202. Kelly, P. J. & Arnell, R. D. Magnetron sputtering: A review of recent developments and applications. *Vacuum* **56**, 159-172 (2000).

203. Tarakeshwar, P., Palacios, J. J. & Kim, D. M. Interface study of metal electrode and semiconducting carbon nanotubes: Effects of electrode atomic species. *IEEE Transc. on Nanotechnology, NMDC* **7**, 124-127 (2006).

204. Qian, Q. *et al.* Trap-State-Dominated Suppression of Electron Conduction in Carbon Nanotube Thin-Film Transistors. *ACS Nano* **8**, 9597–9605 (2014).

205. Collins, P. G. Extreme Oxygen Sensitivity of Electronic Properties of Carbon Nanotubes. *Science (80-.).* **287**, 1801–1804 (2000).

206. Klein, N. The Mechanism of Self-Healing Electrical Breakdown in MOS Structures. *IEEE Trans. Electron Devices* **13**, 788-805 (1966).

207. Wadsworth, W. J. *et al.* Supercontinuum generation in photonic crystal fibers and optical fiber tapers: a novel light source. *J. Opt. Soc. Am. B* **19**, 2148-2155 (2002).

208. Dudley, J. M., Genty, G. & Coen, S. Supercontinuum generation in photonic crystal fiber. *Rev. Mod. Phys.* **78**, 1135–1184 (2006).

209. Alfano, R. R. & Shapiro, S. L. Observation of self-phase modulation and small-scale filaments in crystals and

glasses. *Phys. Rev. Lett.* **24**, 592–594 (1970).

210. Alfano, R. R. & Shapiro, S. L. Emission in the region 4000 to 7000 via four-photon coupling in glass. *Phys. Rev. Lett.* **14**, 584-587(1970).

211. Granzow, N. Supercontinuum white light lasers: a review on technology and applications. **1114408**, 49 (2019).

212. Harris, S. E. & Wallace, R. W. Acousto-Optic Tunable Filter*. *J. Opt. Soc. Am.* **59**, 744 (1969).

213. Chang, I. C. Acousto-Optic Tunable Filters. *Opt. Eng.* **20**, (1981).

214. Bass, M. & others. *Handbook of Optics Volume II Devices, Measurements, and Properties*. (McGraw-Hill, Inc., 1995).

215. Avouris, P., Freitag, M. & Perebeinos, V. Carbon-nanotube photonics and optoelectronics. *Nat. Photonics* **2**, 341–350 (2008).

216. Kinoshita, M. *et al.* The polarized carbon nanotube thin film LED. *Opt. Express* **18**, 25738 (2010).

217. Khasminskaya, S. *et al.* Fully integrated quantum photonic circuit with an electrically driven light source. *Nat. Photonics* **10**, 727–732 (2016).

218. Jariwala, D., Sangwan, V. K., Lauhon, L. J., Marks, T. J. & Hersam, M. C. Carbon nanomaterials for electronics, optoelectronics, photovoltaics, and sensing. *Chem. Soc. Rev.* **42**, 2824–2860 (2013).

219. Bindl, D. J., Wu, M. Y., Prehn, F. C. & Arnold, M. S. Efficiently harvesting excitons from electronic type-controlled semiconducting carbon nanotube films. *Nano Lett.* **11**, 455–460 (2011).

220. He, X., Léonard, F. & Kono, J. Uncooled Carbon Nanotube Photodetectors. *Adv. Opt. Mater.* **3**, 989–1011 (2015).

221. Liu, Y. *et al.* Room Temperature Broadband Infrared Carbon Nanotube Photodetector with High Detectivity and Stability. *Adv. Opt. Mater.* **4**, 238–245 (2016).

222. Balestrieri, M. *et al.* Polarization-Sensitive Single-Wall Carbon Nanotubes All-in-One Photodetecting and Emitting Device Working at 1.55 µm. *Adv. Funct. Mater.* **27**, 1702341 (2017).

223. Liang, S. *et al.* Microcavity-Integrated Carbon Nanotube Photodetectors. *ACS Nano* **10**, 6963–6971 (2016).

224. Rogalski, A., Antoszewski, J. & Faraone, L. Third-generation infrared photodetector arrays. *J. Appl. Phys.* **105**, 091101 (2009).

225. Berciaud, S., Cognet, L. & Lounis, B. Luminescence Decay and the Absorption Cross Section of Individual Single-Walled Carbon Nanotubes. *Phys. Rev. Lett.* **101**, 077402 (2008).

226. Liu, K. *et al.* Systematic determination of absolute absorption cross-section of individual carbon nanotubes. *Proc. Natl. Acad. Sci.* **111**, 7564–7569 (2014).

227. Liu, Y., Wang, S., Liu, H. & Peng, L. M. Carbon nanotube-based three-dimensional monolithic optoelectronic integrated system. *Nat. Commun.* **8**, 15649 (2017).

228. Wang, H. *et al.* CoSO4/SiO2 catalyst for selective synthesis of (9,8) single-walled carbon nanotubes: Effect of catalyst calcination. *J. Catal.* **300**, 91–101 (2013).

229. Sezen, H. & Suzer, S. Communication: Enhancement of dopant dependent x-ray photoelectron spectroscopy peak shifts of Si by surface photovoltage. *J. Chem. Phys.* **135**, 141102 (2011).

230. Çopuroğlu, M., Sezen, H., Opila, R. L. & Suzer, S. Band-Bending at Buried SiO 2 /Si Interface as Probed by XPS. *ACS Appl. Mater. Interfaces* **5**, 5875–5881 (2013).

231. Marcus, M. S., Simmons, J. M., Castellini, O. M., Hamers, R. J. & Eriksson, M. A. Photogating carbon nanotube transistors. *J. Appl. Phys.* **100**, 084306 (2006).

232. Sczygelski, E. *et al.* Extrinsic and intrinsic photoresponse in monodisperse carbon nanotube thin film transistors. *Appl. Phys. Lett.* **102**, 083104 (2013).

233. Alam, A. *et al.* Photocurrent spectroscopy of dye-sensitized carbon nanotubes. *Nanoscale* **9**, 11205-11213 (2017).

234. Ando, T. Theory of Electronic States and Transport in Carbon Nanotubes. *J. Phys. Soc. Japan* **74**, 777–817 (2005).

235. Freitag, M., Martin, Y., Misewich, J. A., Martel, R. & Avouris, P. Photoconductivity of Single Carbon Nanotubes. *Nano Lett.* **3**, 1067–1071 (2003).

236. Lee, J. U., Gipp, P. P. & Heller, C. M. Carbon nanotube p-n junction diodes. *Appl. Phys. Lett.* **85**, 145–147 (2004).

237. Freitag, M. *et al.* Imaging of the Schottky Barriers and Charge Depletion in Carbon Nanotube Transistors. *Nano Lett.* **7**, 2037–2042 (2007).

238. Chang, S.-W., Hazra, J., Amer, M., Kapadia, R. & Cronin, S. B. A Comparison of Photocurrent Mechanisms in Quasi-Metallic and Semiconducting Carbon Nanotube pn-Junctions. *ACS Nano* **9**, 11551–11556 (2015).

239. Mohite, A. D., Gopinath, P., Shah, H. M. & Alphenaar, B. W. Exciton Dissociation and Stark Effect in the Carbon Nanotube Photocurrent Spectrum. *Nano Lett.* **8**, 142–146 (2008).

240. McCulley, D. R., Senger, M. J., Bertoni, A., Perebeinos, V. & Minot, E. D. Extremely Efficient Photocurrent Generation in Carbon Nanotube Photodiodes Enabled by a Strong Axial Electric Field. *Nano Lett.* **20**, 433–440 (2020).

241. Bogaerts, W. *et al.* Nanophotonic waveguides in silicon-on-insulator fabricated with CMOS technology. *J. Light. Technol.* **23**, 401–412 (2005).

242. Tune, D. D., Flavel, B. S., Krupke, R. & Shapter, J. G. Carbon Nanotube-Silicon Solar Cells. *Adv. Energy Mater.* **2**, 1043–1055 (2012).

243. Li, X., Lv, Z. & Zhu, H. Carbon/Silicon Heterojunction Solar Cells: State of the Art and Prospects. *Adv. Mater.* **27**, 6549–6574 (2015).

244. An, Y., Rao, H., Bosman, G. & Ural, A. Characterization of carbon nanotube film-silicon Schottky barrier photodetectors. *J. Vac. Sci. Technol. B, Nanotechnol. Microelectron. Mater. Process. Meas. Phenom.* **30**, 021805 (2012).

245. Salvato, M. *et al.* Single walled carbon nanotube/Si heterojunctions for high responsivity photodetectors. *Nanotechnology* **28**, 435201 (2017).

246. Novikov, A. Experimental measurement of work function in doped silicon surfaces. *Solid. State. Electron.* **54**, 8–13 (2010).

247. Green, M. A. Self-consistent optical parameters of intrinsic silicon at 300K including temperature coefficients. *Sol. Energy Mater. Sol. Cells* **92**, 1305–1310 (2008).

248. Engel, M. *et al.* Photocurrent Spectroscopy of (n, m) Sorted Solution-Processed Single-Walled Carbon Nanotubes. *ACS Nano* **8**, 9324-9331 (2014).

Appendix

A 1 Density of PFO-wrapped (7, 5) SWCNTs in toluene

The density of PFO-wrapped SWCNTs was determined by measuring the sedimentation coefficient of nanotubes in toluene/deuterated-toluene mixtures of different density. The density was varied by mixing toluene with toluene-d8 (Sigma Aldrich) in volume ratios of 0 %, 20 %, 40 %, 60 % and 80 % and the effective density ρ and viscosity η of the mixtures were determined from their volumetric ratios. For the density and viscosity of toluene and toluene-d8 we have used the pressure dependent values reported by Harris (J. Chem. Eng. Data, 45, 893 (2000); 10.1021/je000024l) and Wilbur et al. (The Journal of Chemical Physics 62, 2800 (1975); 10.1063/1.430815). We have interpolated the values to T=20°C and the pressure in the measurement cell. The pressure in the cell has been calculated based on the expression cited by Schuck (Biophysical Chemistry 108, 201 (2004); 10.1016/j.bpc.2003.10.017)

$$p(r) = \rho_0 \omega^2 (r^2 - m^2)/2$$

with ρ_0, the ambient pressure density of the solvent at the meniscus, the position of the meniscus m, the position of interest r, and the angular frequency ω.

With ρ_0 (toluene, 20°C, 0.1MPa) = 867 kg/m^3, m = 5.9$\pm$0.1cm and ω = 40krpm·2π/60s we obtain p = 6.3MPa at the cell center m = 6.5cm. Figure S2 has then been composed using

Interpolated from DOI:10.1021/je000024l

ρ (toluene, 20°C, 0.1 MPa) = 867 kg/m^3

ρ (toluene, 20°C, 6.3 MPa) = 872 kg/m^3

η (toluene, 20°C, 0.1 MPa) = 0.592 mPa.s

η (toluene, 20°C, 6.3 MPa) = 0.622 mPa.s

Interpolated from DOI: 10.1063/1.430815

ρ (toluene-d8, 20°C, 0.1 MPa) = 939 kg/m^3

ρ (toluene-d8, 20°C, 6.3 MPa) = 944 kg/m^3

η (toluene-d8, 20°C, 0.1 MPa) = 0.666 mPa.s

η (toluene-d8, 20°C, 6.3 MPa) = 0.695 mPa.s

By extrapolating the product of sedimentation coefficient s and the viscosity η to s = 0 we obtain ρ_t = 1308 $\pm$ 74 kg/m^3 for the density of PFO-wrapped SWCNTs. The s values are the mean of right-skew Gaussian fits to the s distributions of the respective dispersion mixtures.

A 2 Rigid-rod models

A 2.1 Mansfield – Douglas (Cylinders)

$$A = \frac{L}{2R_{eff}} \tag{1}$$

$$t = ln(A)^{-1} \tag{2}$$

$$f = 6\pi\eta R_{eff} A \left[ln\left(\frac{4A}{e}\right)\right]^{-1} \left[\frac{1 - 0.782t + 0.691t^{1.67} + 0.622t^{1.77} + 0.418t^{2.16}}{1 - 0.677t + 1.601t^{2.07} + 0.178t^{2.26}}\right] \tag{3}$$

A 2.2 Batchelor

$$Y = \left[ln\left(\frac{L}{R_R}\right)\right] \tag{4}$$

$$f_{\parallel} = \frac{2\pi\eta L}{Y}\left(\frac{1 + 0.307Y^{-1}}{1 + 0.5Y^{-1}} + 0.426Y^{-2}\right) \tag{5}$$

$$f_{\perp} = \frac{4\pi\eta L}{Y}\left(\frac{1 + 0.307Y^{-1}}{1 + 0.5Y^{-1}} + 0.119Y^{-2}\right) \tag{6}$$

$$f = 6\pi\eta L\left(\frac{Y^3 + 0.614^2 + 0.638Y + 0.0135}{2Y^4 + 0.614Y^3 + 0.544Y^2 - 0.136}\right) \tag{7}$$

A 2.3 Aragon -Flamik (Cylinder)

$$A = \frac{L}{2R_{eff}} \tag{8}$$

$$f = \frac{3\pi\eta L}{lnA + \chi_\tau} \tag{9}$$

$$\chi_\tau = 0.374304 - \frac{1.11097}{A^{0.5}} + \frac{1.71453}{A} - \frac{0.149474}{A^2} + \frac{0.491453\ ln(A)}{A} - \frac{0{,}091666\ ln(A)}{A^2} \tag{10}$$

A 2.4 Broersma

$$\frac{R}{R_{eff}} = A[ln(2A) - 0.5(\Gamma_{\parallel} + \Gamma_{\perp})]^{-1} \quad (11)$$

$$\Gamma_{\parallel} = 1.27 - 7.4(z - 0.34)^2 \quad (12)$$

$$\Gamma_{\perp} = 0.19 - 4.2(z - 0.39)^2 \quad (13)$$

$$z = [\ln(A)]^{-1} \quad (14)$$

$$A = \frac{L}{2R_{eff}} \quad (15)$$

$$f = 6\pi\eta R \quad (16)$$

A 3 Best fits obtained for rod and flexible chain model

Fraction	Mansfield Douglas Rod model, best fit of Reff	Flexible chain model, best fit of Prefactor b
Frac 1	0.795 nm	1.93·E4
Frac 2	0.78 nm	2.12·E4
Frac 3	0.79 nm	1.74·E4
Frac 4	0.825 nm	1.80·E4

Table A 1: Fitting values of the fits in Figure 3.11.

A 4 Dielectrophoresis Deposition parameters

DEP Type	Substrate	Bias Electrodes	DEP Voltage	Time
DC	300nm oxide – SiO_2/Si	Gate / Drain	2V - 3V	5 min
DC	800nm oxide – SiO_2/Si	Gate / Drain	3V - 5V	5 min
DC	Sapphire	Source / Drain	0.1V - 0.6V	5 min
DC	Silicon on Insulator (SOI)	Source / Drain	2V – 6V	5 min

A 5 Fitting code Examples for Hydrodynamic Theory and Square Root Function

A 5.1 Matlab Fitting

A 5.1.1 Mansfield & Douglas Model

```
eta=0.5753e-3; rhop=1129.67; rhol=867;
L= 10^-9:10^-9:1.2*10^-6;
r=1*10^-9;
%r=1*10^-9:0.3*10^-9:1.6*10^-9;

A=zeros(length(L), length(r));
t=zeros(length(L), length(r));
s=zeros(length(L), length(r));
f=zeros(length(L), length(r));
R=zeros(length(L), length(r));
absS=zeros(length(L), length(r));
%le=zeros(length(S), length(r));
%for k=1:length(S)
for i=1: length(L)
   for j=1: length(r)
A(i,j)=L(i)/(2*r(j));
t(i,j)=(log(A(i,j))^-1);
R(i,j)=(r(j)*A(i,j)*((log((4*A(i,j))/exp(1)))^-1)*...
   ((1-(0.782*t(i,j))+(0.691*t(i,j)^1.67)+(0.622*t(i,j)^1.77)+(0.418*t(i,j)^2.16))/...
   (1-(0.677*t(i,j))+(1.601*t(i,j)^2.07)+(0.178*t(i,j)^2.26))));
f(i,j)=(6*pi*eta*R(i,j));
s(i,j)=(pi*(r(j)^2)*L(i)*(rhop-rhol))/f(i,j);
absS(i,j)=abs(s(i,j))*10^13;

%if abs(absS(i,j)-S(k))<=0.43
  %le(k,j)=L(i);
 % le(k,j)=le(k,j)*10^9;
%end
   end
end
%end

plot(L,absS);

%s=s_r(30:40);

%A=L/2*r;
%t=log(A)^-1;
%R=r*(log((4*A)/exp(1))*(1-0.782*t+0.691*t^1.67+0.622*t^1.77+0.418*t^2.16)/(1 - 0.677*t + 
1.601*t^2.07 + 0.178*t^2.26));
%f=6*pi*eta*R;
%le=zeros(1,length(s));
%for i=1: length(s)
%z=(solve(s(i)==(pi*r^2*L)*(rhop-rhol)/f,L));
```

```
%le(i)=abs(subs(z));
%end
%end
```

A 5.1.2 Flexible chain Model (Square root Model)

```
L=10^-9:1*10^-9:1.8*10^-6; b=1.9*10^4;%:0.5*10^4:2*10^4;
s=zeros(length(L), length(b));
for i=1: length(L)
    for j=1: length(b)
   s(i,j)=b(j)*sqrt(L(i));
    end
end
```

A 5.2 Python Fitting

A 5.2.1 Mansfield & Douglas Model and Square root Model

```
def convert_auc_data(df, b, interpolation=False):
   lower_lim, upper_lim = auc_data_range(df)
   df = df.query('@lower_lim < s_exp < @upper_lim').copy()
   if interpolation:
      df = interp(df, stepsize=0.1)
   df['L'] = np.power(df.s_exp, 2)/b**2
   df['cl'] = df.cs/(df.s_exp*2/b**2)
   df['cl_div_l'] = df.cl/df.L

   return df

from matplotlib.ticker import AutoMinorLocator

df_auc_sqrt = convert_auc_data(df_auc_interp, b=...)
df_auc_mansdoug = best_fit['mans_doug']['data']

x_afm, y_afm = df_afm.L*1e9, df_afm.counts_norm
x_auc, y_auc = df_auc_sqrt.L*1e9, df_auc_sqrt.cl_div_l/df_auc_sqrt.cl_div_l.max()
x_auc_mansdoug, y_auc_mansdoug = df_auc_mansdoug.L*1e9, df_auc_mansdoug.cL_div_L_norm

fig, ax = plt.subplots(figsize=(8.5/2.54, 8.5/2.54))

delta_xafm = abs(x_afm[0]-x_afm[1])*0.9
ax.bar(x_afm, y_afm, width=delta_xafm, color='r', label='AFM')
ax.plot(x_auc, y_auc, color='b', label='AUC: $\sqrt$')
ax.plot(x_auc_mansdoug, y_auc_mansdoug, color='g', label='AUC: M-D')

ax.set_title(sample)
ax.set_xlabel(r'Length (nm)')
```

```
ax.set_ylabel(r'norm. counts $N_N$')
ax.legend(loc='upper right')
#ax.text(0.95, 0.65, r'$b={:.2f}e4\,$Sv$/\sqrt{}$'.format(b/1e4, '{m}'),
#       verticalalignment='top', horizontalalignment='right',
#       transform=ax.transAxes, fontsize=8)

xmin, xmax, xstep = 0, 1200, 200
ax.set_xlim(xmin, xmax)
ax.xaxis.set_ticks(np.arange(xmin, xmax+xstep/2., xstep))
ax.xaxis.set_minor_locator(AutoMinorLocator(2))

ymin, ymax, ystep = 0, 1.08, 0.2
ax.set_ylim(ymin, ymax)
ax.yaxis.set_ticks(np.arange(ymin, ymax+ystep/2., ystep))
ax.yaxis.set_minor_locator(AutoMinorLocator(2))

fig.savefig('plots/'+sample+'_final.png', bbox_inches='tight', dpi=1000)
plt.show()
plt.close()
```

A 6 Number of Excitons Generated per Incident Pulse for a Specific Nanotube

S_{11} Wavelength (λ) = 1045 nm,

Average power (P_{AVG}) = 5.19×10^{-4} W,

Repetition Rate = 80 MHz,

Pulse Width = 6 ps

Area of the laser spot size (A_{SPOT}) = $\frac{\pi(1.22\lambda)^2}{4} = \frac{\pi\{1.22\times(1045\times10^{-9}\ \mathrm{m})\}^2}{4} = 1.28 \times 10^{-12}\mathrm{m}^2$,

Absorption cross-section per carbon of (7,5) at S_{11} (σ_{11}) = 1.8×10^{-21} m^2/Carbon,

Diameter of (7,5) = 0.83nm, Length of a CNT = 800 nm,

Peak power $P_{peak} = \frac{P_{AVG}}{\text{Repition Rate}\times\text{pulse width}} = \frac{5.19\times10^{-4}\ \mathrm{W}}{(80\times10^{6}\ \mathrm{Hz})\times(6\times10^{-12}\mathrm{s})} = 1.08\mathrm{W}.$

Number of photon per second $N_p = \frac{P_{PEAK}}{hc/\lambda} = \frac{1.08\ \mathrm{W}}{(6.63\times10^{-34}\ \mathrm{Js})\times(3\times10^{8}\ \mathrm{ms^{-1}})/(1045\times10^{-9}\ \mathrm{m})}$

$= 5.68 \times 10^{18}\ \mathrm{s^{-1}}.$

Number of carbon atoms per unit length $N_c/L = \frac{4\pi d_t}{a_{c-c}^2\sqrt{3}} = \frac{4\pi\times0.83\ \mathrm{nm}}{(0.249\ \mathrm{nm})^2\times\sqrt{3}} = 97.12\ \mathrm{nm^{-1}}.$

Total number of carbon atoms in 800 nm $N_c = 97.12\ \mathrm{nm^{-1}} \times 800\ \mathrm{nm} = 77696$

Total absorption cross-section $\sigma = 1.8 \times 10^{-21}\ \mathrm{m^2/atom} \times 77696\ \mathrm{atom}$

$= 1.4 \times 10^{-16}\ \mathrm{m^2}.$

Generated number of excitons per pulse (N_G) $= \left(\frac{N_p\times\sigma}{A_{SPOT}}\right) \times$ pulse width

$$= \left(\frac{(5.68 \times 10^{18}\ \mathrm{s^{-1}}) \times (1.4 \times 10^{-16}\ \mathrm{m^2})}{(1.28 \times 10^{-12}\mathrm{m^2})}\right) \times 6 \times 10^{-12}\ \mathrm{s} = 3728\ \text{excitons.}$$